Spurious interface and boundary behaviour beyond physical solutions in lattice Boltzmann schemes

Irina Ginzburg

Version of Record: https://www.sciencedirect.com/science/article/pii/S0021999120307609
Manuscript_4e9ba0f762b3ade6043bc619cf7cf2b5

Spurious interface and boundary behaviour beyond physical solutions in lattice Boltzmann schemes

Irina Ginzburg[a,*]

[a] *Université Paris-Saclay, INRAE, UR HYCAR, 92160, Antony, France*

Abstract

The scalar field and the non-equilibrium solutions of the linear advection-diffusion d2Q9 Lattice Boltzmann (LBM) two-relaxation-times (TRT) scheme are constructed analytically. The scheme copes with an infinite number of suitable, second-order accurate, equilibrium weights. Here, the simplest, translation-invariant geometry with an implicitly located, straight or diagonal, grid-aligned interface (boundary) is addressed. We show that these two interface (boundary) orientations are accommodated with the help of two distinctive, anisotropic, discrete-exponential algebraic solution components, referred to as the A-layer and the B-layer. Being unpredicted by the perturbative analysis, such as the Chapman-Enskog, asymptotic or truncation, their solution is derived symbolically from the TRT recurrence equations, subject to the local mass conservation solvability and effective closure conditions. When the interface (boundary) is "diagonal", the A-layer perturbs the simplest physical solutions, like the piece-wise linear, polynomial or exponential scalar field, rendering the macroscopic solution weight-dependent and delaying its convergence to the first order; the A-layer base depends upon the weights, free relaxation parameter Λ and physical numbers. In contrast, the B-layer, invisible to the scalar field, typically accommodates the non-equilibrium discrepancy between the normal and diagonal directions on the "straight" interface (boundary); the B-layer base is fixed by Λ alone. The A-layer and B-layer may coexist and degrade the physical solution gradient and its convergence. Only the D2Q5 model is free from all these effects in the straight and diagonal orientations, while the diagonally-rotated D2Q5 model is unsuitable because of the "checkerboard" effect. These spurious corrections are not the Knudsen layers, but they present the LBM response for any-order bulk mismatch with the implicit or explicit interface (boundary) treatment; the A-layer and B-layer bring them in evidence and provide excellent benchmarks for their attenuation through interface-conjugate or adaptive refinement techniques. Our approach extends to any lattice, linear collision, source term, heterogeneity and LBM problem class.

Keywords: analytical LBM solution; exponential accommodation; equilibrium weights; implicit interface; bounce-back; local gradient estimate.

1. Introduction

Exact solutions of numerical schemes are interesting for numerous reasons, - they enhance our understanding of them, delineate their degrees of freedom and provide us the best benchmarks for implementation and improvement. In this work, we construct the exact steady-state equilibrium and non-equilibrium solutions of the Lattice Boltzmann method (LBM) for the linear advection-diffusion equation (ADE), in the presence of an implicit interface between heterogeneous domains, characterized by piece-wise continuous diffusion coefficients and mass-sources. Brought into the world about 30 years ago in the pioneering works [52, 39, 40], the LBM has proven its reliability and efficiency in a very disparate panel of physical systems and industrial applications with respect to the heterogeneous physical parameters, boundaries

*Corresponding author
Email address: irina.ginzburg@inrae.fr (Irina Ginzburg)

and interfaces (see [46] and reference herein). Yet, the fundamental principle of the LBM analysis is the Chapman-Enskog expansion [7, 19], ingeniously adapted by the Lattice-gas automata [20] and further generalized [41] for the multiple-relaxation-time (MRT) linear collision. Since the Chapman-Enskog analysis unfolds the non-equilibrium in the form of a perturbative series around the local equilibrium, a smooth behaviour of the macroscopic variables (population moments) and the relaxation rates must be postulated. It follows that neither the Chapman-Enskog analysis nor the Fourier analysis [47, 3], truncation analysis [58, 29, 60] or other alternative perturbative approaches, - asymptotic [43], Hilbert [13] or Taylor [17], to mention a few examples, are valid across an interface. Furthermore, they are not able to provide exact closed-form LBM solutions, except for some particular cases when the non-equilibrium fits into a finite series.

In this context, a very early seminal work [11] solved the Kramers problem [5], examined the exact steady-state modes of the linearized Boltzmann approximation and demonstrated that the solvability conditions of the scheme support the development of anisotropic exponential modes, referred to as the *Knudsen layers*. It was found [11, 12] that the mass-conserving hydrodynamic wall condition, - a linear combination of the bounce-back and the specular reflection, is "suitable", in the sense that it suppresses those "spurious" modes, either for a parallel or a perpendicular wall orientation with respect to the FHP lattice. Moreover, it was suggested that (i) the solid body location is impacted by the kinetic degrees of freedom and (ii), the effective location is *anisotropic* with respect to the lattice. These two suggestions were confirmed [22] for the Maxwell reflections in the straight and diagonal Poiseuille Stokes flow via the exact Taylor boundary analysis combined with the exact, third-order-accurate, Chapman-Enskog non-equilibrium expansion. This combination becomes a key point in the construction of high-order accurate, wall-shaped boundary rules for both flow and ADE problems, either with in-node based (LSOB) or directional (multi-reflection) techniques (see [23, 24, 27, 48, 18, 61, 62, 63]).

Another analysis approach consists in the exact solution of the whole steady-state population update in the discrete-velocity, single-relaxation-rate (BGK) basis [55], where the polynomial population distribution is *a priori* prescribed [73, 66]. More generally, the solvability condition is reorganized [38] in the form of the central finite-difference momentum equation, where its discrete solutions, either in polynomial or exponential form, are recognized, and their free parameters are tuned to fit the boundary rule. Notably, the bounce-back "slip" is observed [73, 38], but it is not linked with the kinetic effect. Nevertheless, the solution procedure [38], although limited to the grid-aligned channel flow, gains popularity in establishing the effective wall location [see [9] and reference herein]. However, a similar inconsistency is also observed for effective bulk transport coefficients, e.g., the anisotropic modification of the Brinkman viscosity, either due to linear velocity dependency of the resistance [54] or because of the "partial-bounce-back" BGK update [8, 70, 72] is recognized, but not connected with the Chapman-Enskog expansion. This happens because the methodology [38] does not build any non-equilibrium solution *explicitly*.

The exact solvability condition and the exact non-equilibrium construct are handled together by the recurrence equations [42]. Either transient or steady-state, the recurrence equations linearly inter-relate the central-difference, equilibrium and non-equilibrium, operators to non-equilibrium solution. The recurrence equations are especially attractive for being intuitive, dimension- and lattice-transparent with the directional collisions, like the anisotropic-ADE L-basis [25] or its particular sub-class, the two-relaxation-time TRT collision [24, 71, 53, 36]; the TRT is suitable for both hydrodynamic and advection-diffusion problems, [26]. The form of the recurrence solutions proves [42] that any steady-state TRT bulk solution is controlled by the free-tunable product of its two relaxation eigenfunctions, $\Lambda = \Lambda^{-}\Lambda^{+}$. If the boundary scheme maintains this parametrization, the error-estimate becomes transport-coefficient independent; the MRT shares this feature provided that a specific scaling [14, 45] of its additional collision rates is accounted for. It is demonstrated [28] that a perturbative expansion of the recurrence steady-state non-equilibrium solution into an infinite series around an equilibrium coincides with the Chapman-Enskog expansion; the discrete solvability conditions (mass-conservation equations) are then expressed through the moments of the recurrence relations exactly; their Taylor expansion delivers the truncation corrections [29, 30].

However, the recurrence non-equilibrium solution can be perturbed [42] for zero-equilibrium by an *additive, directional* correction of the type $a_q K^n + b_q K^{-n}$, which we are refer to as the B-layer. The B-layer develops along the boundary-cut segment $n\vec{c}_q$, its base K is determined by Λ and the constants are fixed through the boundary rules. A very particular choice $\Lambda = \frac{1}{4}$ expresses the non-equilibrium through the

equilibrium variables exactly, and it constrains the B-layer correction to the boundary nodes. The simplest example [27] has been given for the bounce-back straight Poiseuille flow profile, which is identical with the parabolic (Stokes) and the quartic (Navier-Stokes) equilibrium thanks to the B-layer assistance. The B-layer is typically overlooked when it accommodates the high-order mismatch with the boundary rule, where it remains "invisible" to the macroscopic solution, e.g. [73, 38]. Yet, the boundary or interface closure relations are not necessarily illegitimate for their *tangential component*, even at the first order, [26, 25, 2, 50]. The bounce-back weight-dependent restriction of the tangential advection-diffusion flux gives an outstanding example [24, 21, 48, 51]. Recall, there is an infinite number of suitable, advection and diffusion, equilibrium weight families, ranging from the coordinate (d2Q5, d3Q7) to the diagonally-rotated (d2Q5$^{(r)}$, d3Q7$^{(r)}$) stencil. Typically, the Λ impact on the accuracy largely exceeds the discretization [45] or weight-stencil effects [15]. However, only the d2Q5 and d3Q7 moments do not suffer from the bounce-back tangential spurious effect in *the transient* ADE solutions, as shown for the straight channel and the cylindrical capillary, respectively, [32]. Otherwise, the B-layer accommodation explains (i) the retardation of the average advection velocity (first moment), - evident in plug flow [24], and (ii), the decrease of the diffusion coefficient (second moment), - revealed by the early work [16]. These two *macroscopic corrections* are proportional, respectively, to the *diagonal* advection and diffusion weight, and they decay only when Λ reduces to zero; a low-cost remedy [32] attenuates them by adapting distinctive Λ values in bulk and boundary nodes.

Curiously, the very similar but *steady-state scalar solution* of the bounce-back and implicit-interface ADE reveals to be weight-independent in the straight geometry for a large variety of the mass sources and velocity fields, [34]. This work extends the B-layer construct [32] to the implicit interface between two heterogeneous domains, explains this apparent contradiction and reveals the B-layer importance for local macroscopic gradient in steady-state straight solutions. On top of that, it is discovered that the scalar-field itself becomes perturbed by the discrete-exponential accommodation on the *diagonal interface/boundary*. This quite unexpected solution element is referred to as the A-layer; on top of Λ, the A-layer base depends upon the equilibrium weights and physical governing parameters. For comparison, the bounce-back Stokes pipe flow [23, 57] excites the spurious velocity modifications only in the lattice-rotated geometry, because the parallel flow does not evolve along the boundary-normal link in the diagonal channel [22, 26], to be contrasted with the d2Q9 equilibrium diffusion weight-stencil.

The two distinctive, weight-dependent accommodation mechanisms, the A-layer and B-layer, are not predicted by the Chapman-Enskog analysis. In the previous symbolic "straight" constructs, the symmetric non-equilibrium component in the ADE schemes [34], or the anti-symmetric non-equilibrium component in the flow models [28, 31, 61], is uniquely identified through the symmetry conditions. Now we confront this principal limitation and solve the complete set of the recurrence non-equilibrium equations. The obtained solutions describe exactly how the A-layer and B-layer interplay with the canonical scalar profiles: (i) the piece-wise linear in the pure diffusion; (ii) the discrete-exponential in the interface-perpendicular constant velocity and (iii), the polynomial in the interface-parallel flow.

The modelled ADE with velocity-dependent sources allow us to predict the effective diffusivity and the longitudinal Taylor-Aris dispersion [65, 1]; they are respectively, produced by the averaged scalar-field solution gradient and the averaged scalar-field product with the longitudinal-velocity following [4, 56, 68, 67]. In that respect, we also examine the truncation corrections of the commonly used, local, non-equilibrium gradient estimate, e.g. [6]. Perhaps surprisingly, it is shown that the truncation produces (i) a non-zero solution gradient along the invariant direction, and (ii), a gradient dependency upon an additive solution constant, e.g., in the parabolic and the higher-order polynomial velocity profiles. Finally, the individual role of the rotation, truncation, the A-layer and B-layer accommodations in the scalar field and its gradient is examined with respect to the reference solutions [33].

The paper is organized as follows. Sec. 2 recalls the TRT scheme and its recurrence equations, formulates the effective ADE and its interface/boundary closure, introduces the A-layer and B-layer. Sec. 3 develops solution procedure in the straight and diagonal heterogeneous layers. Secs. 4 applies it within the interface-perpendicular, fully periodic evolution process. Sec. 5 addresses the interface-parallel, stratified, bounded and unbounded systems. Sec. 6 concludes the paper, where the principal accommodation scenarios are summarized in Table 1. Appendix A and Appendix B construct the A-layer and B-layer, respectively.

2. Background

2.1. The two-relaxation-time TRT

The LBM is operated on the cuboid computational grid within the penetrable d-dimensional domain $\vec{r} \in V$; an equidistant mesh-size is set equal to one lattice unit. The neighboring nodes are interconnected by the $d-$dimensional discrete velocity set $dDqQ$; it consists of a zero-amplitude vector $\vec{c}_0$ and $Q_m = Q-1$ vectors $\vec{c}_q$. The local variable of the scheme is the set of Q real numbers called "populations": $\{f_q(\vec{r},t)\ ,\ q = 0,..,Q_m\}$. The populations $\{f_q(\vec{r},t)\}$ enter into the local collision, sums with their post-collision values $\{\hat{n}_q(\vec{r},t)\}$, and then propagate to the neighboring sites along their discrete velocities. Any two populations with the opposite velocities $\vec{c}_{\bar{q}} = -\vec{c}_q$ are decomposed into their symmetric and anti-symmetric components: $\{f_q^{\pm} = \frac{1}{2}(f_q \pm f_{\bar{q}})\}$ and $\{\hat{n}_q^{\pm} = \frac{1}{2}(\hat{n}_q \pm \hat{n}_{\bar{q}})\}$. In the presence of the time-independent mass-source $M(\vec{r})$, the TRT collision-stream algorithm reads:

$$
\begin{aligned}
f_q(\vec{r}+\vec{c}_q,t+1) &= f_q(\vec{r},t) + \hat{n}_q^+(\vec{r},t) + \hat{n}_q^-(\vec{r},t)\ ,\ q = 1,\ldots,\frac{Q_m}{2}\ ,\\
f_{\bar{q}}(\vec{r}+\vec{c}_{\bar{q}},t+1) &= f_{\bar{q}}(\vec{r},t) + \hat{n}_q^+(\vec{r},t) - \hat{n}_q^-(\vec{r},t)\ ,\ q = 1,\ldots,\frac{Q_m}{2}\ ,\\
f_0(\vec{r},t+1) &= f_0(\vec{r},t) + M(\vec{r}) - 2\sum_{q=1}^{Q_m/2}\hat{n}_q^+(\vec{r},t)\ ,\\
\text{with}\quad \hat{n}_q^{\pm}(\vec{r},t) &= -\frac{f_q^{\pm}(\vec{r},t) - e_q^{\pm}(\vec{r},t)}{\tau^{\pm}(\vec{r})}\ ,\ q = 1,\ldots,\frac{Q_m}{2}\ ,\ \vec{r}\in V\ .
\end{aligned}
\tag{1}
$$

The equilibrium distribution $e_q(\vec{r},t)$ is prescribed as the sum of its two counterparts, $\{e_q = e_q^+ + e_q^-\}$:

$$
\begin{aligned}
e_q^+(\vec{r},t) &= c_e(t_q^{(m)}C^{(eq)}(\vec{r}) + t_q^{(M)}\tau^+(\vec{r})M(\vec{r}))\\
&= t_q^{(m)}c_e(C(\vec{r}) + \Lambda^+(\vec{r})M(\vec{r})) + c_e(t_q^{(M)} - t_q^{(m)})\tau^+(\vec{r})M(\vec{r})\ ,
\end{aligned}
\tag{2a}
$$

$$
e_q^-(\vec{r},t) = t_q^{(a)}C(\vec{r},t)\vec{u}(\vec{r})\cdot\vec{c}_q - t_q^{(m)}\vec{J}_k(\vec{r})\cdot\vec{c}_q\ ,\ q = 1,\ldots,\frac{Q_m}{2}\ ,
\tag{2b}
$$

$$
C(\vec{r},t) = C^{(eq)}(\vec{r},t) + \frac{1}{2}M(\vec{r})\ ,\ C^{(eq)} = \beta_e\frac{\rho(\vec{r},t)}{\phi(\vec{r})}\ ,\ \beta_e \geq 1\ ,\ \rho(\vec{r},t) = \sum_{q=0}^{Q_m} f_q(\vec{r},t)\ ,
\tag{2c}
$$

$$
\sum_{q=1}^{Q_m} t_q c_{q\alpha}c_{q\beta} = \delta_{\alpha\beta}\ ,\ \forall\alpha\ ,\forall\beta\ ,\ t_q = \{t_q^{(m)},t_q^{(M)},t_q^{(a)}\}\ ,\ t_q = \{t_c,t_d\} \geq 0\ .
\tag{2d}
$$

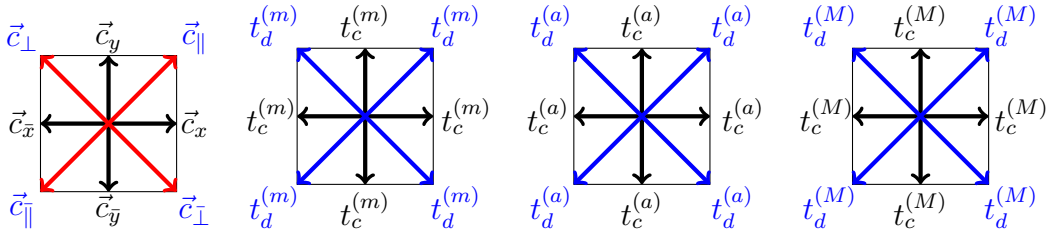

Figure 1: The d2Q9 discrete-velocity set, the diffusion-weight $t_q^{(m)} = \{t_c^{(m)},t_d^{(m)}\}$, the velocity-weight $t_q^{(a)} = \{t_c^{(a)},t_d^{(a)}\}$ and the mass-source weight $t_q^{(M)} = \{t_c^{(M)},t_d^{(M)}\}$, Eq. (2). The d2Q5 $[\vec{c}_q = \{\vec{c}_x,\vec{c}_y\}]$ is $\{t_c = \frac{1}{2}\ ,\ t_d = 0\}$. The "rotated" d2Q5$^{(r)}$ $[\vec{c}_q = \{\vec{c}_\parallel,\vec{c}_\perp\}]$ is $\{t_c = 0\ ,\ t_d = \frac{1}{4}\}$.

We prescribe: (i) continuous steady-state velocity field $\vec{u}(\vec{r})$; (ii) molecular diffusion coefficient $\mathcal{D}_0$; (iii) diffusion-scale $c_e \in]0, c_e^{max}(t_c^{(m)})]$; and (iv), block-wise heterogeneous porosity distribution $\phi(\vec{r}) = \{\phi_k\}$,

together with the associated diffusive-flux jump-term $\vec{J}_k(\vec{r})$; hereafter, k specifies a sub-domain $V_k \in V$. The two relaxation parameters $\tau^{\pm} = \{\tau_k^{\pm}\}$ are computed from the positive distribution $\Lambda^{\pm}(\vec{r}) = \{\Lambda_k^{\pm}\}$ giving their free-tamable product $\Lambda = \{\Lambda_k\}$:

$$\tau_k^{\pm}(\vec{r}) := \Lambda_k^{\pm}(\vec{r}) + \frac{1}{2} \ , \ \tau_k^{\pm} > \frac{1}{2} \ , \ \Lambda_k^{-} \ := \phi_k \Lambda^{-} \ , \ \Lambda_k^{+} := \tfrac{\Lambda_k}{\Lambda_k^{-}} \ , \ \Lambda^{-} := \tfrac{\mathcal{D}_0}{c_e} \ . \tag{3}$$

Based either on the Chapman-Enskog expansion or the TRT recurrence-equations, the steady-state second-order approximate of Eqs. (1)-(3) matches the linear advection-diffusion equation in the form:

$$\nabla \cdot (\vec{u}(\vec{r})C(\vec{r}) \ \ -\vec{J}_k(\vec{r})) - M_k(\vec{r}) = \mathcal{D}_k \Delta^2 C(\vec{r}) \ , \ C(\vec{r}) = \{C_k(\vec{r})\} \ , \ \mathcal{D}_k = \{\phi_k \mathcal{D}_0\} \ , \ \vec{r} \in V_k \ , \ V = \{V_k\} \ . \tag{4}$$

It is assumed that $\phi(\vec{r})$ and $\vec{u}(\vec{r})$ are periodic along mean seepage-velocity direction $\vec{U}_{z'} = U_{z'}\vec{1}_{z'}$, and the mass source $M_k(\vec{r})$ is set velocity-dependent:

$$M_k(\vec{r}) = \phi_k U_{z'} - u_{z'}(\vec{r}) \ , \ U_{z'} = \frac{< u_{z'} >}{< \phi >} \ , \ M(\vec{r}) = \{M_k(\vec{r})\} \ , \ < M >= 0 \ . \tag{5}$$

Hereafter, $< \cdot >$ denotes an averaging over the penetrable part of a single periodic cell V; $< M >= 0$ assures the solvability condition of Eq. (4) in fully periodic or impermeable domain. Eq. (4) is subject to periodic, interface and boundary conditions, respectively:

$$C(\vec{r} + L_{z'}\vec{1}_{z'}) = C(\vec{r}) \ , \tag{6a}$$

$$||C||_{A_\phi} = 0 \ , \ || - \mathcal{D}_k \vec{n} \cdot \nabla C||_{A_\phi} = ||\vec{n} \cdot \vec{J}_k||_{A_\phi} \ , \tag{6b}$$

$$-\mathcal{D}_k \vec{n} \cdot \nabla C|_{A_s} = \vec{n} \cdot \vec{J}_k|_{A_s} \ , \ \vec{J}_k = \mathcal{D}_k \vec{1}_{z'} \ , \tag{6c}$$

$\vec{n}$ is an inward or outward, normal vector on the boundary A_s or interface A_ϕ, and $|| \cdot ||$ denote the jump of a scalar variable along $\vec{n}$. The boundary value problem (4)- (6) allows to predict [68, 33] the effective diffusivity $\mathcal{D}_{eff}$ of the porous structure and its Taylor dispersion coefficient $\mathcal{D}_T$ in given velocity field. Without loss of generality, we employ these two a posteriori functionals in the error-estimates of the local gradient $\partial_{z'} C(\vec{r})$ and the scalar-field $C(\vec{r})$, respectively. The EMM extends the model equation over the higher-order moments (skewness, kurtosis, ...) produced with the recursively re-constructed polynomial and exponential mass source, [68, 33]. In this work we construct the effective steady-state solutions of the TRT scheme when it runs without any modification across the interface. The interface is set aligned with one of the discrete d2Q9 velocities, either the coordinate ("straight") or the "diagonal". In this context, the full-stencil d2Q9 scheme prescribes freely the three non-negative weight families $t_q = \{t_q^{(m)}, t_q^{(a)}, t_q^{(M)}\}$, where we denote t_c for the coordinate links and t_d for the diagonal links; the two values are only constrained to Eq. (2d). We will operate the d2Q9 scheme assigned on the half velocity set $\vec{c}_q = \{\vec{c}_x, \vec{c}_y, \vec{c}_\parallel, \vec{c}_\perp\}$ (see Fig. 1):

$$\vec{c}_x = \{1, 0\} \ , \ \vec{c}_y = \{0, 1\} \ , \ \vec{c}_\parallel = \{1, 1\} \ , \ \vec{c}_\perp = \{-1, 1\} \ . \tag{7}$$

The d2Q9 reduces to "grid-aligned" models: (i) d2Q5 $[\vec{c}_q = \{\vec{c}_x, \vec{c}_y\}]$ with $\{t_c = \frac{1}{2} \ , \ t_d = 0\}$, and (ii), "rotated" d2Q5$^{(r)}$ $[\vec{c}_q = \{\vec{c}_\parallel, \vec{c}_\perp\}]$ with $\{t_c = 0 \ , \ t_d = \frac{1}{4}\}$. Identical weight $t_q^{(a)} = t_q^{(m)} = t_q^{(M)} = t_q$ is a suitable choice, including $t_q^{(a)} = t_q^{(m)} = \frac{1}{4}$ in combination with $\Lambda = \frac{1}{4}$ for advanced stability (see [29, 30] and reference herein). The necessary stability conditions relate c_e with the velocity amplitude $||\vec{u}||^{max}$ in homogeneous domain; on top of stability, the numerical [10] and truncation [29, 30] role of c_e has been investigated. The commonly used "hydrodynamic" weights obey one additional constraint: $2\sum_{q=1}^{Q_m/2} t_q c_{q\alpha}^2 c_{q\beta}^2 = \frac{1}{3}$, $\alpha \neq \beta$ [then $\{t_c, t_d\} = \{\frac{1}{3}, \frac{1}{12}\}$ in d2Q9]; the hydrodynamic weights assure the rotational invariance of the truncation corrections [29]. Further details can be found on the TRT truncation and non-negativity [58, 59], anisotropy [25, 29], weights- and $\Lambda-$ joined effects [71, 15, 32], heterogeneity and acceleration parameter β_e to steady-state [68, 34]. It is noted that the steady-state solutions are independent of β_e.

2.2. Boundary/interface equations

Any interface-cut link $\vec{c}_q$ connecting the node $\vec{r}_N^{(1)}$ in phase $k=1$ to node $r_0^{(2)} = \vec{r}_N^{(1)} + \vec{c}_q$ in phase $k=2$ implicitly introduces two interface closure conditions [26]:

$$[e_q^+ + \frac{1}{2}\hat{n}_q^- - \Lambda^+ \hat{n}_q^+]|_{\vec{r}_N^{(1)}} = [e_q^+ - \frac{1}{2}\hat{n}_q^- - \Lambda^+ \hat{n}_q^+]|_{r_0^{(2)} = \vec{r}_N^{(1)} + \vec{c}_q} \ , \tag{8a}$$

$$[e_q^- + \frac{1}{2}\hat{n}_q^+ - \Lambda^- \hat{n}_q^-]|_{\vec{r}_N^{(1)}} = [e_q^- - \frac{1}{2}\hat{n}_q^+ - \Lambda^- \hat{n}_q^-]|_{r_0^{(2)} = \vec{r}_N^{(1)} + \vec{c}_q} \ . \tag{8b}$$

These conditions present the linear combinations (the half-sum and half-difference, respectively) of the steady-state TRT update from Eq. (1) using Eq. (3) to express the non-equilibrium component $f_q^\pm - e_q^\pm = -\tau^\pm \hat{n}_q^\pm$. When the anti-bounce-back (ABB) rule [24, 9, 32] applies as the Dirichlet boundary condition at $\vec{r}_s = \vec{r}_N + \frac{1}{2}\vec{c}_q$, or the bounce-back (BB) applies as the flux boundary condition, their steady-state closure relations read:

$$\begin{aligned} \text{ABB} \ : \ f_{\bar{q}}(\vec{r}_N) &:= -[f_q + \hat{n}_q^+ + \hat{n}_q^-](\vec{r}_N) + 2e_q^+(\vec{r}_s) \ , \ \text{ then} \\ & e_q^+ + \frac{1}{2}\hat{n}_q^- - \Lambda^+ \hat{n}_q^+|_{\vec{r}_N} = e_q^+(\vec{r}_s) \ , \end{aligned} \tag{9a}$$

$$\begin{aligned} \text{BB} \ : \ f_{\bar{q}}(\vec{r}_N) &:= \ [f_q + \hat{n}_q^+ + \hat{n}_q^-](\vec{r}_N) - 2e_q^-(\vec{r}_s) \ , \ \text{ then} \\ & e_q^- + \frac{1}{2}\hat{n}_q^+ - \Lambda^- \hat{n}_q^-|_{\vec{r}_N} = e_q^-(\vec{r}_s) \ , \ \vec{r}_s = \vec{r}_N + \frac{1}{2}\vec{c}_q \ . \end{aligned} \tag{9b}$$

The linear combinations (9a) and (9b) of the collision and post-collision components are the same as the implicit interface relations in Eqs. (8a) and (8b), respectively. It follows that the present analysis of the implicit interface comprises both the ABB and BB closure conditions.

2.3. Recurrence equations, solvability condition and the A-layer

On top of Eq. (8), the steady-state evolution update from Eq. (1) is reformulated [42, 28] through the equivalent central-difference *recurrence equations*, which present the *three-point* linear directional combinations of Eq. (1). In the present context, they are valid inside the homogeneous domain $\vec{r} \in V_k$. The two pairs of the *steady state* recurrence equations read as follows [phase index k is dropped]:

$$\begin{cases} \hat{n}_q^\pm(\vec{r}) = [\bar{\Delta}_q e_q^\mp - \Lambda^\mp \bar{\Delta}_q^2 e_q^\pm + (\Lambda - \frac{1}{4})\bar{\Delta}_q^2 \hat{n}_q^\pm](\vec{r}) \ , \ q = 1, \dots, Q_m \ , \ \hat{n}_0^\pm \equiv 0 \ , & \text{(10a)} \\ [\bar{\Delta}_q^2 e_q^\pm - \Lambda^\pm \bar{\Delta}_q^2 \hat{n}_q^\pm - \bar{\Delta}_q \hat{n}_q^\mp](\vec{r}) = 0 \ , \ q = 1, \dots, Q_m \ . & \text{(10b)} \end{cases}$$

The central-difference operators apply link-wisely: $\bar{\Delta}_q \psi(\vec{r}) = \frac{1}{2}(\psi(\vec{r} + \vec{c}_q) - \psi(\vec{r} - \vec{c}_q))$ and $\bar{\Delta}_q^2 \psi(\vec{r}) = \psi(\vec{r} + \vec{c}_q) - 2\psi(\vec{r}) + \psi(\vec{r} - \vec{c}_q)$, $\forall \psi = \{e_q^\pm, \hat{n}_q^\pm\}$. The steady-state solvability condition of Eq. (1) reads:

$$M(\vec{r}) = 2 \sum_{q=1}^{Q_m/2} \hat{n}_q^+(\vec{r}) \ . \tag{11}$$

Plugging Eq. (10a) for $\hat{n}_q^+$ into Eq. (11), the steady-state mass conservation equation reads with Eq. (2):

$$\bar{\nabla} \cdot (\vec{u}C - \vec{J}) - M - \mathcal{E} = c_e \Lambda^- \bar{\Delta}^2 C \ . \tag{12}$$

The error-term $\mathcal{E}(\vec{r})$ denotes the discrepancy with *the central-difference approximation* of Eq. (4):

$$\mathcal{E}(\vec{r}) \ = \Lambda c_e \bar{\Delta}^2 M(\vec{r}) - 2(\Lambda - \tfrac{1}{4}) \textstyle\sum_{q=1}^{Q_m/2} \bar{\Delta}_q^2 \hat{n}_q^+(\vec{r}) + 2c_e \Lambda^-(\vec{r}) \tau^+(\vec{r}) \sum_{q=1}^{Q_m/2} (t_q^{(M)} - t_q^{(m)}) \bar{\Delta}_q^2 M \ . \tag{13}$$

Eqs. (12)-(13) are expressed through the weighted central-difference operators $\bar{\nabla} \cdot \vec{\psi} := \sum_{q=1}^{Q_m} t_q \bar{\Delta}_q \vec{\psi} \cdot \vec{c}_q$ and $\bar{\Delta}^2 \psi := \sum_{q=1}^{Q_m} t_q \bar{\Delta}_q^2 \psi$. These discrete operators are weight-independent and rotational-invariant at the

second-order due to Eq. (2d); however, at the higher orders, they are both weight-stencil and angle-dependent in the rotated coordinate system (x', y'):

$$x' = \cos[\theta]x + \sin[\theta]y \ , \ y' = -\sin[\theta]x + \cos[\theta]y \ , \ \theta \in [0, \frac{\pi}{2}] \ . \tag{14}$$

The heterogeneous layers $\phi = \{\phi_k\}$ are set parallel with the translation-invariant axis $\vec{1}_{x'}$; Eqs. (4) and (5) are prescribed with $\vec{u}(y')$, and then $M(y')$. Exact solutions [68, 33] to Eqs. (4)- (6) combine the polynomial and exponential functions in the two basic cases: (i), in "series", when the constant velocity is perpendicular with the interface, $\vec{u} = u_\perp \vec{1}_{y'}$; and (b), in "stratified layers", when the interface-parallel velocity $\vec{u} = u_\parallel(y')\vec{1}_{x'}$ is polynomial or exponential. We assume that there exists the translation-invariant *discrete* solution $C(y')$ to Eqs. (1)- (2) with the implicit interface conditions in Eq. (8). The scalar field is then decomposed on the polynomial "(p)-"component $P(y')$ and the discrete-exponential "(a)-"component $A(y')$:

$$C(y') = P(y') + A(y') \ , \ P(y') = \sum_{m=0} p_m {y'}^m \ , \ A(y') = \sum_{j=1} a_j(y') {r_j}^{y'} \ . \tag{15}$$

The unknowns are coefficients $\{p_m\}$ and polynomials $\{a_j(y')\}$; the base $\{r_j\}$ is to be derived from the solvability condition given by Eq. (12). The "a-"component sums the physical and accommodation branches.

Definition: The *accommodation* component of $A(y')$ is referred to as the A-layer. The A-layer modifies directly the macroscopic scalar solution and hence, an equilibrium; its directional evolution modifies the physical nonequilibrium solution.

In general, $\mathcal{E}(\vec{r})$ from Eq. (13) vanishes if only $M(\vec{r})$ is piece-wise linear and $\Lambda = \frac{1}{4}$; hence, the symbolic solving of Eqs. (12)-(13) needs us to derive the set $\{\hat{n}_q^+(\vec{r})\}$ exactly. Its solution is known a-priori only in a "straight" translation-invariant d2Q5 configuration $y' = y$, e.g. [34]:

$$\text{d2Q5} \ , \ \theta = 0 \ , \ t_q = \frac{1}{2} \quad : \quad \hat{n}_q^+(y') = t_q M(y') c_{qy'}^2 \ . \tag{16}$$

In this work, we exactly construct the effective solutions $P(y')$, $A(y')$ and $\{\hat{n}_q^\pm(y')\}$ in the straight and the diagonal d2Q9 systems. We operate them with the three distinctive weight-stencils but $t_q^{(m)} = t_q^{(M)}$ vanishes the last terms in Eqs. (2a), (13) and allows for their physical parametrization.

2.4. Non-equilibrium accommodation: the B-layer

Due to linearity, the recurrence equations in Eq. (10) all remain satisfied when $\hat{n}_q^\pm(\vec{r})$ is summed with the directional additive correction $\hat{B}_q^\pm(\vec{r})$, which solves Eq. (10) with $e_q^\pm \equiv 0$:

$$\begin{cases} \hat{B}_q^\pm(\vec{r}) = (\Lambda - \frac{1}{4})\bar{\Delta}_q^2 \hat{B}_q^\pm(\vec{r}) \ , \ q = 1, \dots, Q_m \ , \ \hat{B}_0^\pm \equiv 0 \ , & \text{(17a)} \\ [\Lambda^\pm \bar{\Delta}_q^2 \hat{B}_q^\pm + \bar{\Delta}_q \hat{B}_q^\mp](\vec{r}) = 0 \ , \ q = 1, \dots, Q_m \ . & \text{(17b)} \end{cases}$$

The B-layer concept is introduced [42] as a way to adjust the closure relations of the directional boundary schemes. In this work, the B-layer is constructed along the interface-cut directional segment $\vec{r}_n$ between two interface nodes $\vec{r}_0 \in V_k$ and $\vec{r}_N \in V_k$ inside the same phase "k" [$\Lambda = \Lambda_k$, phase index k is dropped]:

$$\Lambda \neq \frac{1}{4} \ : \ \hat{B}_q^\pm(\vec{r}_n) = b_q^\pm K_{(\sigma)}^n + d_q^\pm K_{(\sigma)}^{-n} \ , \ \vec{r}_n = \vec{r}_0 + n\vec{c}_q \ , \ n = 0, \dots, N \ , \tag{18a}$$

$$K_{(\sigma)} = \frac{2\sqrt{\Lambda} - \sigma}{2\sqrt{\Lambda} + \sigma} \ , \ b_q^- = \sigma \frac{\sqrt{\Lambda}}{\Lambda^-} b_q^+ \ , \ d_q^- = -\sigma \frac{\sqrt{\Lambda}}{\Lambda^-} d_q^+ \ , \ \sigma = \pm 1 \ . \tag{18b}$$

$$\Lambda = \frac{1}{4} \ : \ \hat{B}_q^\mp(\vec{r}_0) = \frac{\hat{B}_q^\pm(\vec{r}_0)}{2\Lambda^\mp} \ , \ \hat{B}_q^\mp(\vec{r}_N) = -\frac{\hat{B}_q^\pm(\vec{r}_N)}{2\Lambda^\mp} \ , \ 2\Lambda^\mp = \frac{1}{2\Lambda^\pm} \ . \tag{18c}$$

The B-layer obeys the symmetry argument: $\hat{B}^+_{\bar{q}} = \hat{B}^+_q$ and $\hat{B}^-_{\bar{q}} = -\hat{B}^-_q$. When $\Lambda \neq \frac{1}{4}$, the system has two (equivalent) roots: $K_{(+1)} = K^{-1}_{(-1)}$; the unknown coefficients $b^\pm_q$ and $d^\pm_q$ are inter-related in Eq. (18b) [these relations are obtained with the help of Eq. (17b)]. When $\Lambda = \frac{1}{4}$, the B-layer is set exclusively with the interface (boundary) node values $\{\hat{B}^+_q(\vec{r}_0), \hat{B}^+_q(\vec{r}_N)\}$; their counterparts $\{\hat{B}^-_q(\vec{r}_0), \hat{B}^-_q(\vec{r}_N)\}$ are expressed from them through Eq. (18c). The unknown directional coefficients $\{b^+_q, d^+_q\}$, or the accommodation node-values $\{\hat{B}^+_q(\vec{r}_0), \hat{B}^+_q(\vec{r}_N)\}$, are derived from the interface (boundary) closure relations.

Definition: Solution $\{\hat{B}^\pm_q\}$ to Eq. (17) in the form of Eq. (18) is referred to as *the B-layer*. The B-layer does not modify the scalar field *directly*; its base $K_{(\pm1)}$ is determined by Λ alone.

Appendix B specifies the B-layer construct in straight and diagonal interface geometry.

3. The straight and the diagonal heterogeneous layers

We solve the recurrence equations, subject to the local mass conservation solvability and the effective closure conditions, in straight and diagonal heterogeneous layers described with an implicit interface. Sec. 3.1 specifies our geometrical set-up and the interface conditions. Sec. 3.2 formulates the symbolic solution algorithm. Sec. 3.3 presents the numerical validation and the error-estimates.

3.1. Geometry, interface and boundary conditions

Our numerical and symbolic solutions in the straight and the diagonal layers are computed in a single vertical column as sketched in Fig. 2; phase $k = 1$ is bellow the interface $n = 0$: $\phi = \phi_1$, $y \in]-H_1, 0[$, and phase $k = 2$ is above it: $\phi = \phi_2$, $y \in]0, H_2[$, using convention:

$$\theta = 0 \ : \ y'(n) = n^{(k)} + \frac{1}{2} \ ; \tag{19a}$$

$$\theta = \frac{\pi}{4} \ : y'(n) = \frac{\sqrt{2}}{2}(n^{(k)} + \frac{1}{2}) \ , \ n^{(1)} = -H_1, \ldots, -1 \ ; \ \ n^{(2)} = 0, \ldots, H_2 - 1 \ . \tag{19b}$$

The "internal" numbering n_k is convenient with the B-layer description in Eq. (18), and it is adopted hereafter:

$$\text{phase } k = 1 : \ n_1 = n^{(1)} + H_1 = 0, 1, \ldots, H_1 - 1 \ ; \tag{20a}$$

$$\text{phase } k = 2 : \ n_2 = n^{(2)} = 0, 1, \ldots, H_2 - 1 \ . \tag{20b}$$

The interface-perpendicular velocity ("series") is vertical in the straight system, $\vec{u} = u_\perp \vec{1}_y$, and complanar with the $\vec{c}_\perp$ in the diagonal system: $\vec{u} = u_\perp \vec{1}_{y'} = u_\perp \vec{1}_\perp$. The interface-parallel velocity ("stratified layers") is horizontal in the straight system, $\vec{u} = u_\parallel \vec{1}_x$, and complanar with the $\vec{c}_\parallel$ in the diagonal system, $\vec{u} = u_\parallel \vec{1}_{x'} = u_\parallel \vec{1}_\parallel$ according to Eq. (7). The two exact closure relations per interface-cut link are set by Eq. (8); they apply on the "internal" and "periodic" (bounding) interfaces sketched in Fig. 2. Eq. (9b) with $e^-_q(\vec{r}_s) = 0$ replaces the bounding interface in impermeable system. The closure relations are all expressed through the three evolution velocity vectors: $\vec{c}_q[\theta = 0] = \{\vec{c}_y, \vec{c}_\parallel, \vec{c}_\perp\}$ and $\vec{c}_q[\theta = \frac{\pi}{4}] = \{\vec{c}_x, \vec{c}_y, \vec{c}_\perp\}$, with the help of the symmetry argument: $\psi^+_{\bar{q}} = \psi^+_q$ and $\psi^-_{\bar{q}} = -\psi^-_q$ applied to all solution components, with $\psi^+ = \{e^+_q, \hat{n}^+_q\}$ and $\psi^- = \{e^-_q, \hat{n}^-_q\}$.

3.1.1. The straight layers

Consider the interface nodes $\{n^{(1)}, n^{(2)}\} := \{\vec{r}^{(1)}_N, r^{(2)}_0 = \vec{r}^{(1)}_N + \vec{c}_q\}$ when $\theta = 0$. The "internal" interface imposes the six relations:

$$3 \ \times \ \text{Eqs. (8a)- (8b)} \ \ \text{with} \ \ \{n^{(1)}, n^{(2)}\} = \{-1, 0\} \ , \ \vec{c}_q = \{\vec{c}_y, \vec{c}_\parallel, \vec{c}_\perp\} \ . \tag{21}$$

The "periodic" interface relates the bounding nodes similarly:

$$3 \ \times \ \text{Eqs. (8a)- (8b)} \ \ \text{with} \ \ \{n^{(1)}, n^{(2)}\} = \{-H_1, H_2 - 1\} \ , \ \vec{c}_{\bar{q}} = \{\vec{c}_y, \vec{c}_\parallel, \vec{c}_\perp\} \ . \tag{22}$$

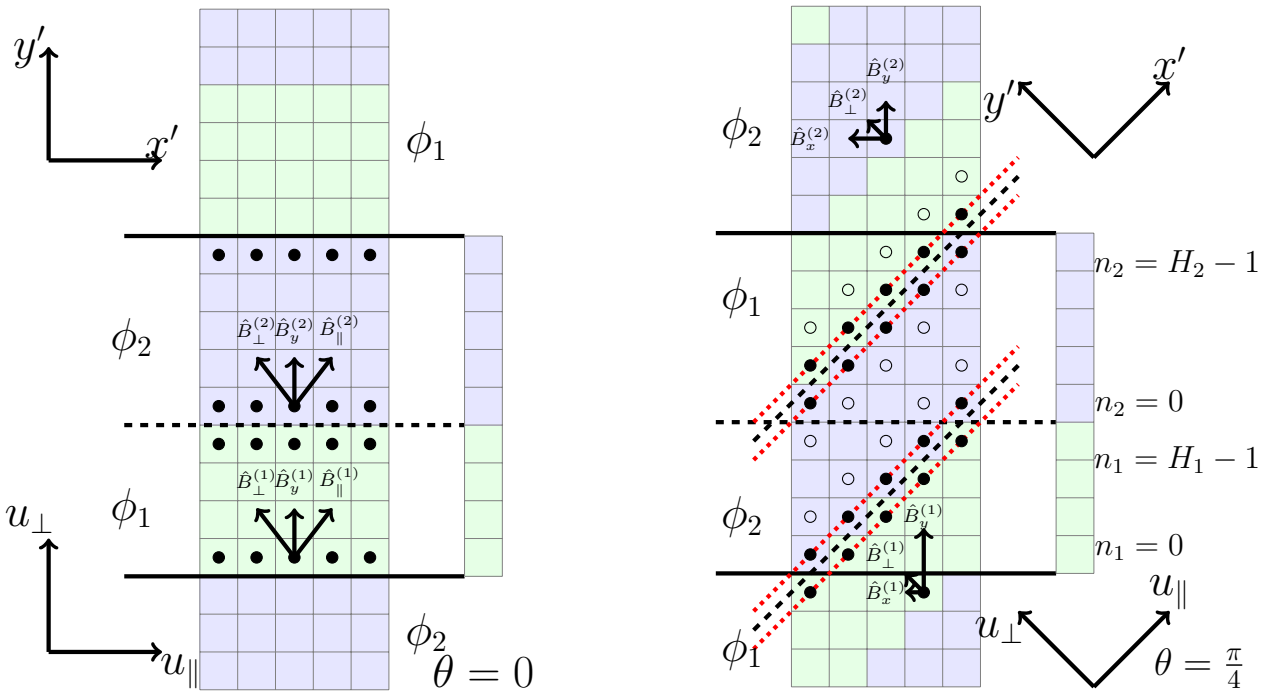

Figure 2: The straight (left) and the diagonal (right) two-layered heterogeneous system is modeled as a single vertical column with the help of the straight or diagonal, respectively, periodic conditions. The velocity field is $\vec{u} = \{u_\parallel, u_\perp\}$; the implicit midway interface between the blocks ϕ_1 and ϕ_2 is parallel with the $\vec{1}_{x'}$ [black dashed]. Two blocks in "series": Eq. (4) applies with $\vec{1}_{z'} = \vec{1}_{y'} = \vec{1}_\perp$ in the pure-diffusion process and the interface-perpendicular Darcy flow $\vec{u} = u_\perp \vec{1}_{y'}$. Two stratified layers: Eq. (4) applies with $\vec{1}_{z'} = \vec{1}_{x'} = \vec{1}_\parallel$ in the parallel flow $\vec{u} = u_\parallel(y')\vec{1}_{x'}$. When $\Lambda = \frac{1}{4}$, the B-layer $\{\hat{B}_q^{\pm(k)}\}$ is constrained to the interface nodes ("filled circles"), and it vanishes in the nodes with the single interface-cutted link ("empty circles").

The impermeable boundary replaces Eq. (22) by Eq. (9b) for 3×2 wall-cut links. In total, there are 6×2 interface/boundary closure relations in the two-layered straight system. They reduce to the 2×2 conditions along $\vec{c}_y$ in d2Q5, and the 4×2 conditions along $\{\vec{c}_\parallel, \vec{c}_\perp\}$ in d2Q5$^{(r)}$. The periodic conditions are imposed for all outgoing horizontal links.

3.1.2. The diagonal layers

Consider the interface nodes $\{\vec{r}_N^{(1)}, r_0^{(2)} = \vec{r}_N^{(1)} + \vec{c}_q\} = \{n^{(1)}, n^{(2)}\}$ when $\theta = \frac{\pi}{4}$. The "internal" interface imposes

$$4 \times \text{ Eqs. (8a)- (8b)} \quad \text{with} \tag{23a}$$

$$\{n^{(1)}, n^{(2)}\} = \{-1, 0\}\ ,\ \vec{c}_q = -\vec{c}_x\ ,\ \text{and}\ \ \{n^{(1)}, n^{(2)}\} = \{-1, 0\}\ ,\ \vec{c}_q = \vec{c}_y\ , \tag{23b}$$

$$\{n^{(1)}, n^{(2)}\} = \{-1, 1\}\ ,\ \vec{c}_q = \vec{c}_\perp\ ,\ \text{and}\ \ \{n^{(1)}, n^{(2)}\} = \{-2, 0\}\ ,\ \vec{c}_q = \vec{c}_\perp\ . \tag{23c}$$

The periodic interface prescribes

$$4 \times \text{ Eqs. (8a)- (8b)} \quad \text{with} \tag{24a}$$

$$\{n^{(1)}, n^{(2)}\} = \{-H_1, H_2 - 1\}\ ,\ \vec{c}_q = \vec{c}_x\ ,\quad \text{and}\ \{n^{(1)}, n^{(2)}\} = \{-H_1, H_2 - 1\}\ ,\ \vec{c}_q = -\vec{c}_y\ , \tag{24b}$$

$$\{n^{(1)}, n^{(2)}\} = \{-H_1, H_2 - 2\}\ ,\ \vec{c}_q = -\vec{c}_\perp\ ,\ \text{and}\ \{n^{(1)}, n^{(2)}\} = \{-H_1 + 1, H_2 - 1\}\ ,\ \vec{c}_q = -\vec{c}_\perp\ . \tag{24c}$$

The 4 bounce-back closure relations (9b) replace Eq. (24) on the impermeable ends. Altogether, there are 8×2 interface/boundary closure relations. They reduce to the 4×2 conditions, along $\{\vec{c}_x, \vec{c}_y\}$ and $\{\vec{c}_\parallel, \vec{c}_\perp\}$, respectively, in d2Q5 and d2Q5$^{(r)}$. The *diagonal* periodic conditions are imposed for all outgoing links $\vec{c}_\parallel$.

3.2. Solution procedure

The scalar field $C_k(n)$ is decomposed on polynomial "(p)" and accommodation "(a)" components with Eq. (15); the post-collision $\hat{n}_q^{\pm(k)}(n)$ is additionally amended by the B-layer component $\hat{B}_q^{\pm(k)}(n)$ from Eq. (18):

$$C_k(n) = P_k(n) + A_k(n)\ ,\ P_k(n) = \sum_{m=0} p_m^{(k)} n^m\ ,\ A_k(n) = \sum_{j=1} a_j^{(k)}(n)[r_j^{(k)}]^{n_k}\ , \tag{25a}$$

$$\hat{n}_q^{\pm(k)}(n) = \hat{P}_q^{\pm(k)}(n) + \hat{A}_q^{\pm(k)}(n) + \hat{B}_q^{\pm(k)}(n)\ ,\quad q = 1, \ldots, \frac{Q_m}{2}\ ,\ n = -H_1, \ldots, H_2 - 1\ , \tag{25b}$$

$$\hat{P}_q^{+(k)}(n) = \sum_{m=0} \hat{p}_{q,m}^{(k)} n^m\ ,\ \hat{A}_q^{+(k)}(n) = \sum_{j=1} \hat{a}_{q,j}^{(k)}(n)[r_j^{(k)}]^{n_k}\ ,\ n_k = 0, 1, \ldots, H_k - 1\ ,\ k = 1, 2\ . \tag{25c}$$

The unknowns are: the base $\{r_j^{(k)}\}$; the coefficients $\{p_m^{(k)}, a_j^{(k)}\}$ and the directional coefficients $\{\hat{p}_{q,m}^{(k)}, \hat{a}_{q,j}^{(k)}\}$. On top of them, the B-layer directional coefficients $\{b_q^{+(k)}, d_q^{+(k)}\}$ from Eq. (18b) or, when $\Lambda = \frac{1}{4}$, the interface-node values $\{\hat{B}_q^+(\vec{r}_0), \hat{B}_q^+(\vec{r}_N)\}$ from Eq. (18c), are unknowns. In our examples, $\{r_j\}$, $\{p_m^{(k)}\}$ and $\{b_q^{+(k)}, d_q^{+(k)}\}$ are piece-wise constant; $\{a_j^{(k)}(n), \hat{a}_{q,j}^{(k)}(n)\}$ are either piece-wise constant or polynomial. The symmetric post-collision components $\hat{n}_q^{+(p,k)} = \hat{P}_q^{+(k)}(n)$ and $\hat{n}_q^{+(a,k)} = \hat{A}_q^{+(k)}(n)$ solve Eq. (10a):

$$\hat{n}_q^{+(l,k)}(n) \quad = \quad [\bar{\Delta}_q e_q^{-(l,k)} - \Lambda^- \bar{\Delta}_q^2 e_q^{+(l,k)} + (\Lambda - \frac{1}{4})\bar{\Delta}_q^2 \hat{n}_q^{+(l,k)}](n)\ ,\ l = \{p, a\}\ ,\ k = 1, 2\ . \tag{26}$$

Their counterpart $\hat{n}_q^{-(l,k)} = \{\hat{P}_q^{-(k)}, \hat{A}_q^{-(k)}\}$ is expressed from them by combining Eqs. (10a) and (10b):

$$\Lambda_k^- \hat{n}_q^{-(l,k)} \quad = \quad [\Lambda_k^- \bar{\Delta}_q e_q^{+(l,k)} - \frac{1}{4}\bar{\Delta}_q^2 e_q^{-(l,k)} - (\Lambda_k - \frac{1}{4})\bar{\Delta}_q \hat{n}_q^{+(l,k)}]\ ,\ l = \{p, a\}\ . \tag{27}$$

Eq. (11) implies the solvability conditions in the form:

$$\sum_{q=1}^{Q_m/2} \hat{n}_q^{+(l,k)}(n) = \frac{1}{2} M^{(l,k)}(n)\ ,\ l = \{p, a\}\ , \tag{28a}$$

$$\sum_{q=1}^{Q_m/2} \hat{B}_q^{+(k)}(n) = 0\ ,\ k = 1, 2\ . \tag{28b}$$

The solution procedure consists of the following steps.

1. Eq. (25a) is plugged into $e_q^{+(l,k)}$; Eq. (25c) expresses $\hat{n}_q^{+(l,k)}$, $l = \{p, a\}$; Eq. (26) is discretized with Eqs. (A.1)-(A.2) by substituting all these relations;
2. The directional relations $\{\hat{p}_{q,m}^{(k)}(p_m^{(k)})\}$ and $\{\hat{a}_{q,j}^{(k)}(a_j^{(k)})\}$ are derived from Eq. (26) by vanishing its polynomial coefficients;
3. The obtained relations are substituted into Eq. (25c); the $\{\hat{P}_q^{+(k)}(n)\}$ and $\{\hat{A}_q^{+(k)}(n)\}$ are then plugged into solvability condition given in Eq. (28a);
4. Eq. (28a) is solved for $\{r_j^{(k)}\}$, the second- and the higher-order coefficients $\{p_m^{(k)}\ ,\ m \geq 2\}$;
5. Eq. (27) expresses $\hat{P}_q^{-(k)}$ and $\hat{A}_q^{-(k)}$;
6. The B-layer $\hat{B}_q^{\pm(k)}(n)$ is expressed through its unknown coefficients $\{b_q^{+(k)}, d_q^{+(k)}\}$, Appendix B;
7. Eqs. (8)-(9) substitute $e_q^{\pm}$ and $\hat{n}_q^{\pm(k)}(n)$ from Eq. (25b) with all derived relations, and close the system;
8. The closure equations are solved for the remaining coefficients; they determine solution in Eq. (25).

Typically, the closure relations fix the lower-order polynomial coefficients $\{p_0^{(k)}, p_1^{(k)}\}$ to an additive constant; they also determine the A-layer coefficients $\{a_j^{(k)}\}$ and the B-layer coefficients $\{b_q^{+(k)}, d_q^{+(k)}\}$ [or, when $\Lambda = \frac{1}{4}$, the B-layer in-node values, see Eq. (B.6)]; the $A_k(n)$ can be based on the physical and accommodation roots to solvability condition. Beyond the parabolic profile, $P_k(n)$ deviates from the exact solution due to the truncation corrections. The A-layer and/or B-layer accommodation is excited by the set of the directional closure relations when the discrete, physical solution cannot satisfy them; the accommodation may then modify the physical solution, its gradient and the next-order terms.

3.3. Numerical validation

The symbolic, straight and diagonal, configurations are exemplified in the two next sections. The resulting linear system includes up to 8×2 closure equations, e.g. Eqs. (23)- (24); the whole system is solved either symbolically or by substituting the numerical data. The symbolical procedure basically simplifies when $\Lambda = \frac{1}{4}$. All constructed solutions are first verified on the numerical profile $C(n)$ and the steady-state post-collision output $\hat{n}_q^{\pm}(n)$ from Eq. (1). For that, we compare the normalized (constant-independent) distributions $\mathcal{C}(n)$:

$$\mathcal{C}(\vec{r}) = C(\vec{r}) - \overline{C} \ , \ \overline{C} = \frac{< C\phi >}{< \phi >} \ , \text{ then } \quad \frac{< \mathcal{C}\phi >}{< \phi >} = 0 \ . \tag{29}$$

One can also determine a particular constant value by fitting the predicted solution $C(n)$ to the numerical profile when the post-collision depends on an additive constant. The same value $\Lambda_k = \Lambda$ is applied in both phases but the solution procedure remains valid when Λ_k is piece-wise constant. Typically, we performed the first verification using $H_1 = 8$, $H_2 = 11$, $\phi_1 = \frac{1}{4}$, $\phi_2 = 1$, $||\vec{u}|| = 10^{-2}$, $c_e = 0.1$, $\Lambda^- = 1$, and the arbitrary prescribed weight families, e.g., $t_c^{(a)} = \frac{3}{10}$, $t_c^{(m)} = \frac{1}{4}$, $t_c^{(M)} = \frac{1}{8}$, with $\Lambda = \{\frac{1}{12}, \frac{1}{4}, 2\}$. The numerical convergence study is performed with $t_c = \frac{1}{3}$ and $t_c = \frac{1}{4}$, when $\Lambda = \frac{1}{4}$ and $\Lambda = \frac{1}{6}$ [these two values enhance the stability and the fourth-order spatial accuracy, respectively, see [29, 30]]. Numerical computations confirm the superior stability of the combination $\{\Lambda = \frac{1}{4}, t_c = \frac{1}{4}\}$, e.g., when approaching the diffusion stability limit on the fine grid [$c_e \to c_e^{max} = \frac{r_\phi}{4t_c^{(m)}\beta_e}$ using $c_e = 1/16$, $\phi_2 = 1$, $r_\phi = \phi_1/\phi_2 = \{\frac{1}{8}, \frac{1}{4}\}$, and $\beta_e \in [1, 4]$]. A nearly linear acceleration to steady state is achieved using $\beta_e > 1$. Once solution is validated, the symbolic error estimate is examined in the full parameter range.

The boundary-value problem in Eqs. (4)-(6) allows to predict [68, 33] the effective diffusivity $\mathcal{D}_{eff}$ and the longitudinal Taylor dispersion coefficient k_T:

$$\mathcal{D} = \mathcal{D}_{eff} + \mathcal{D}_T \ , \quad \text{where} \tag{30a}$$

$$\mathcal{D}_{eff} = \mathcal{D}_0(1 + < \partial_{z'}\mathcal{C}(n) >) \ , \ < \partial_{z'}\mathcal{C}(n) > = \frac{\sum_n \phi(n)\partial_{z'}\mathcal{C}(n)}{< \phi >} \ , \ < \phi > = \sum_k \phi_k H_k \ , \tag{30b}$$

$$\mathcal{D}_T = k_T \mathcal{D}_{eff} \ , \ k_T = -\frac{\sum_n u_{z'}(n)\mathcal{C}(n)}{< \phi > \mathcal{D}_{eff}} \ , \ u_{z'} = \vec{u}(n) \cdot \vec{1}_{z'} \ , \tag{30c}$$

$$\text{with } \ \vec{1}_{z'} = \vec{1}_{y'} \ \text{ if } \ \vec{u} = u_\perp \vec{1}_{y'} \ , \text{ and } \ \vec{1}_{z'} = \vec{1}_{x'} \ \text{ if } \ \vec{u} = u_\parallel \vec{1}_{x'} \ . \tag{30d}$$

The solution gradient $\partial_{z'}C(n) = \sum_l \partial_{z'}C^{(l)}(n)$ is approximated locally:

$$\partial_{z'}C^{(l)}(n) := \frac{2}{c_e} \sum_{q=1}^{Q_m/2} \hat{n}_q^{-(l)}(n) c_{q,z'} \ , \ \hat{n}_q^{-(l)} = \{\hat{P}_q^{-(k)}, \hat{A}_q^{-(k)}, \hat{B}_q^{-(k)}\} \ , \ l = \{p, a, b\} \ , \ k = 1, 2 \ . \tag{31}$$

The respective truncation "(p)", A-layer "(a)" and B-layer "(b)" contributions are quantified as:

$$\mathrm{E}(\mathcal{D}_{eff}) \quad = \mathrm{E}^{(p)} + \mathrm{E}^{(a)} + \mathrm{E}^{(b)} \ , \ \mathrm{E}^{(p)} = \frac{\mathcal{D}_0(1 + < \partial_{z'}C^{(p)} >)}{\mathcal{D}_{eff}} - 1 \ , \ \{\mathrm{E}^{(a)}, \mathrm{E}^{(b)}\} = \frac{\mathcal{D}_0 < \partial_{z'}C^{(l)} >}{\mathcal{D}_{eff}} \ . \tag{32}$$

In the presence of advection, the physical "(p)" and the A-layer "(a)" contributions to $\mathrm{E}(k_T)$ are quantified:

$$\mathrm{E}(k_T) = \mathrm{E}(k_T^{(p)}) + \mathrm{E}(k_T^{(a)}) \ , \ \mathrm{E}(k_T^{(p)}) = \frac{k_T^{(p)}}{k_T} - 1 \ , \ \mathrm{E}(k_T^{(a)}) = \frac{k_T^{(a)}}{k_T} \ , \ k_T^{(l)} = -\frac{\sum_n u_{z'}(n)\mathcal{C}^{(l)}(n)}{< \phi > \mathcal{D}_{eff}} \ , \ l = \{p, a\} \ . \tag{33}$$

4. Heterogeneous layers in "series"

We consider (i) the pure diffusion in Sec. 4.1 and (ii) the interface-perpendicular Darcy flow $\vec{u} = u_\perp \vec{1}_{y'}$ in Sec. 4.2. The one-dimensional advection-diffusion process is conducted through the periodic series of two

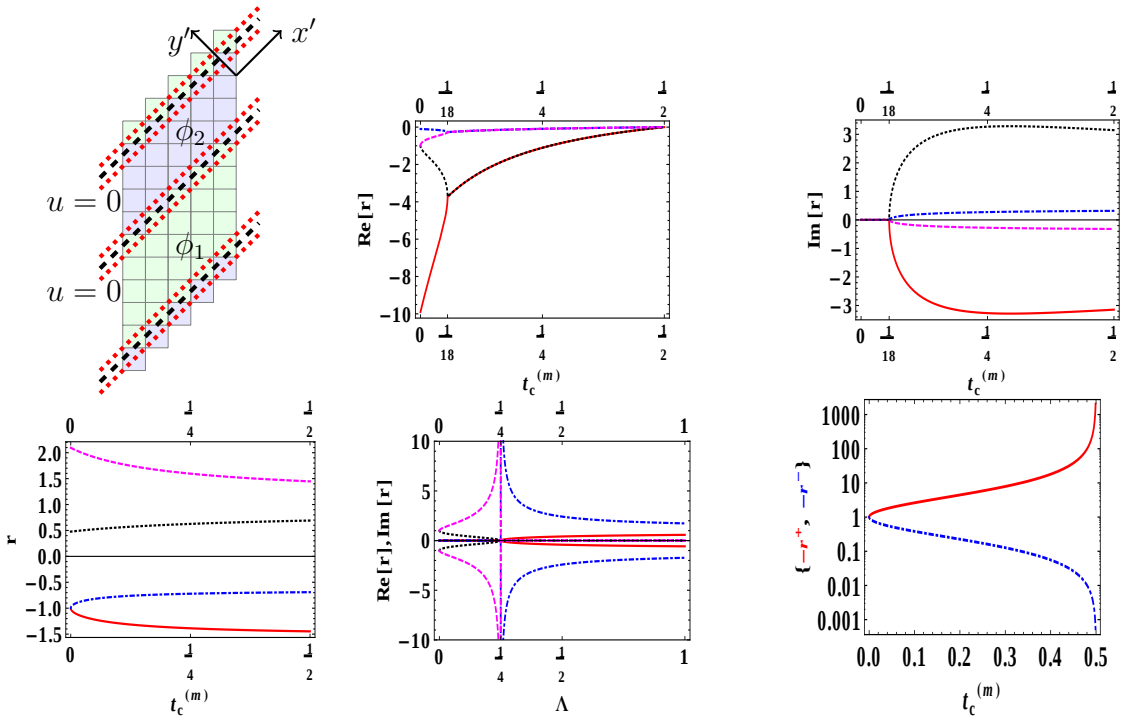

Figure 3: The pure-diffusion process through the diagonal layers (a); (b) and (c), the A-layer with $\Lambda = \frac{1}{6}$, the four roots to Eq. (42) are real when $t_c^{(m)} < \frac{1}{18}$, Eq. (A.7); (d): the A-layer with $\Lambda = 2$, the four roots to Eq. (42) are real $\forall t_c^{(m)}$ when $\Lambda > \frac{1}{4}$; (e): the A-layer with $t_c^{(m)} = \frac{1}{2}$, the four roots obey Eq. (A.8b); (f) the A-layer with $\Lambda = \frac{1}{4}$, the two roots from Eq. (43) are negative.

heterogeneous layers parallel with the axis $\vec{1}_{x'}$: $\phi = \phi_1$ when $y' \in [-h_1', 0]$ and $\phi = \phi_2$ when $y' \in [0, h_2']$ (see Fig. 3). Eqs. (4)-(6) read:

$$u_\perp \partial_{y'} C_k(y') - M_k = \partial_{y'} \mathcal{D}_k \partial_{y'} C_k(y') \ , \ M_k := \phi_k U_{y'} - u_\perp \ , \ k = 1, 2 \ , \tag{34a}$$

$$U_{y'} := \frac{< u_\perp >}{< \phi >} = \frac{u_\perp h'}{\phi_1 h_1' + \phi_2 h_2'} \ , \ Pe_\perp^{(k)} := \frac{u_\perp}{\mathcal{D}_k} \ , \ \mathrm{Pe} := \frac{U_{y'} h'}{\mathcal{D}_0} \ , \ h' = h_1' + h_2' \ , \tag{34b}$$

$$C_1|_{y'=\{0,-h_1'\}} = C_2|_{y'=\{0,h_2'\}} \ , \tag{34c}$$

$$-J_1 - \mathcal{D}_1 \partial_{y'} C_1|_{y'=\{0,-h_1'\}} = -J_2 - \mathcal{D}_2 \partial_{y'} C_2|_{y'=\{0,h_2'\}} \ , \ \vec{J}_k = J_k \vec{1}_{y'} \ , \ J_k = \mathcal{D}_k \ . \tag{34d}$$

The mass-source M_k is piece-wise constant; the diffusion-flux jump is prescribed with Eq. (34d). We construct the effective solutions $C(y')$ and $\hat{n}_q^{\pm}(y')$; they extend the d2Q5 results [34] to d2Q9 in the two grid-aligned considered orientations.

4.1. Pure diffusion

The pure diffusion process $\vec{u} = 0$ develops in the interface-perpendicular direction $\vec{1}_{y'}$. The coefficients of the effective diffusivity, skewness and kurtosis are derived [33] (Eq. (52) there) and applied [34] to validate the d2Q5 TRT scheme. In this work we limit ourselves to $\mathcal{D}_{eff}$ [$M = 0$ in Eq. (34)], because the focus is put on the accommodation effect in this characteristic measurement.

4.1.1. Exact solution

The piece-wise linear solution $C_k(y') = P_k(y')$ to Eq. (34) is defined to an additive constant p_0:

$$\begin{aligned} P_1(y') &= p_0 + p_1^{(1,ex)} y' \ , \ p_1^{(1,ex)} = \frac{h_2'(\phi_2 - \phi_1)}{\phi_1 h_2' + \phi_2 h_1'} \ , \ y' \in [-h_1', 0] \ , \\ P_2(y') &= p_0 + p_1^{(2,ex)} y' \ , \ p_1^{(2,ex)} = \frac{h_1'(\phi_1 - \phi_2)}{\phi_1 h_2' + \phi_2 h_1'} \ , \ y' \in [0, h_2'] \ . \end{aligned} \tag{35}$$

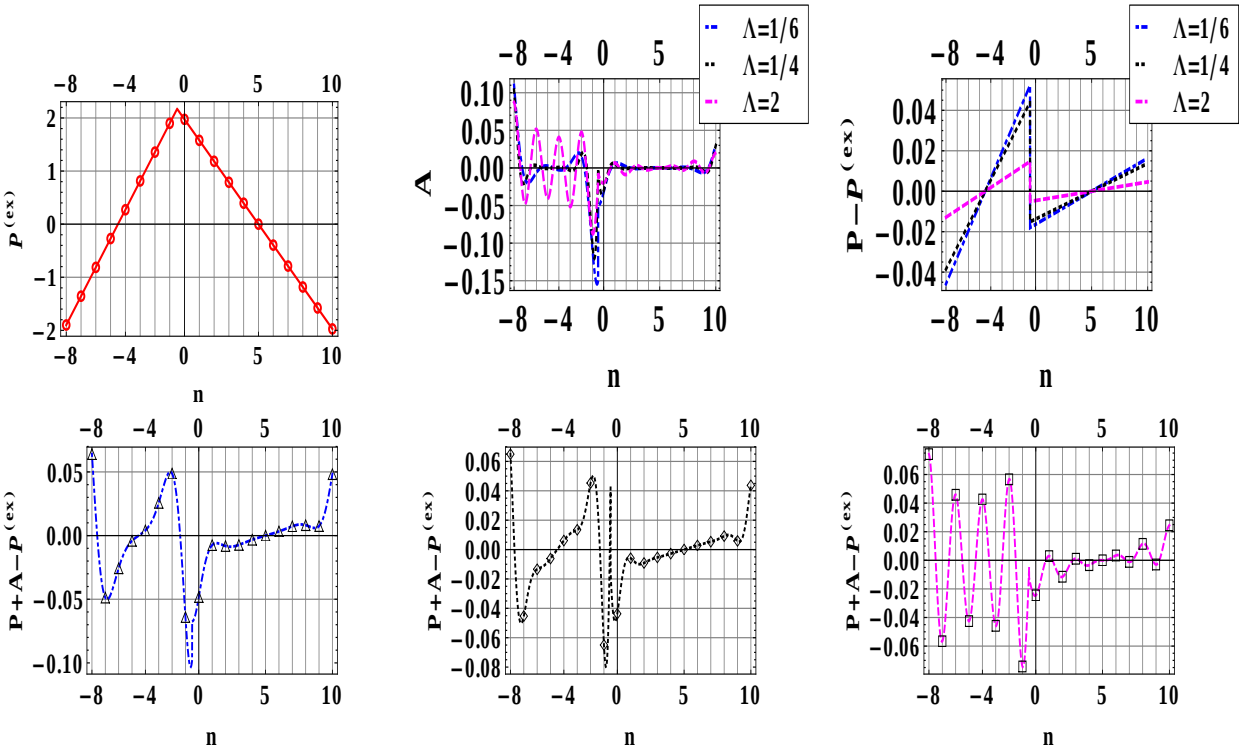

Figure 4: The pure-diffusion process through the diagonal layers. The normalized, theory (lines) and numerical (symbols) solution $\mathcal{C}(n)$. (a) d2Q5: $C(n) = P(n) = P^{(ex)}(n)$, Eq. (35) with Eq. (19). The d2Q9: (b) the A-layer $A(n)$ is built on the roots (42); (c) $P(n) - P^{(ex)}(n)$; (d), (e), (f): the whole deviation $P + A - P^{(ex)}$ when $\Lambda = \{\frac{1}{6}, \frac{1}{4}, 2\}$ [dashed, dotted, dash-dotted]. Data: the d2Q9 with $\{t_c^{(m)} = \frac{1}{4}, t_d^{(m)} = \frac{1}{8}\}$], $\phi_1 = \frac{1}{4}$, $\phi_2 = 1$, $H_1 = 8$, $H_2 = 11$, $c_e = 10^{-1}$, $\Lambda^- = 1$. $\mathrm{E}(\mathcal{D}_{eff}) \approx \{1.05 \times 10^{-2}, 8.8 \times 10^{-3}, 2.9 \times 10^{-3}\}$, (d)-(f).

The normalized solution $\mathcal{C}(y')$ obeys Eq. (29) and it is illustrated in Fig. 4. Eq. (30b) gives $\mathcal{D}_{eff}$:

$$\mathcal{D}_{eff} = \mathcal{D}_0(1 + < \phi >^{-1} (\phi_1 \int_{-h_1'}^{0} \partial_{y'} C_1 dy' + \phi_2 \int_{0}^{h_2'} \partial_{y'} C_2 dy')) \ , \ < \phi >= \phi_1 h_1' + \phi_2 h_2' \ , \tag{36a}$$

$$\mathcal{D}_{eff} = \mathcal{D}_r \mathcal{D}_0 \ , \ \mathcal{D}_r = \frac{(1 + r_h)^2 r_\phi}{(r_h + r_\phi)(1 + r_h r_\phi)} \ , \ r_\phi = \frac{\phi_1}{\phi_2} \ , \ r_h = \frac{h_1'}{h_2'} \ . \tag{36b}$$

Thus, $\mathcal{D}_{eff}$ is equal to the length-weighted harmonic mean of the two phase values, $\phi_1 \mathcal{D}_0$ and $\phi_2 \mathcal{D}_0$, divided by mean porosity value $\bar{\phi} =< \phi > /h'$; $\mathcal{D}_{eff}$ is rotational-invariant and it is fixed by the porosity contrast r_ϕ and the aspect ratio r_h.

4.1.2. The polynomial component

Assume the piece-wise linear solution $P_k = p_0^{(k)} + p_1^{(k)} y'$ and $M_k = 0$, then

$$e_q^{+(p,k)}(y') = t_q^{(m)} c_e P_k(y') \ , \ e_q^{-(k)}(y') = -t_q^{(m)} J_k c_{q,y'} \ , \tag{37a}$$

$$\hat{P}_q^{-(k)}(y') = t_q^{(m)} c_e p_1^{(k)} c_{q,y'} \ , \ p_1^{(k)} = \partial_{y'} P_k(y') \ , \tag{37b}$$

$$\hat{P}_q^{+(k)}(y') = -\mathcal{D}_k t_q^{(m)} p_2^{(k)} c_{q,y'} \ , \ \mathcal{D}_k = \Lambda_k^- c_e \ , \ p_2^{(k)} = \partial_{y'}^2 P_k = 0 \ . \tag{37c}$$

When $\partial_{y'} P_k$ is derived with Eq. (31) [$\vec{1}_{z'} = \vec{1}_{y'}$], Eq. (30b) gives:

$$\mathcal{D}_{eff}(P_k) \quad = \mathcal{D}_0 (1 + < \phi >^{-1} \sum_k \phi_k p_1^{(k)} H_k) \ , \ < \phi > = \sum_k \phi_k H_k \ . \tag{38}$$

Eq. (38) is equivalent to Eq. (36a) provided that the discrete aspect ratio is equal to r_h and $p_1^{(k)} = p_1^{(k,ex)}$. We examine whether this exact solution may satisfy the implicit interface.

4.1.3. The straight system with the d2Q9: no A-layer, no B-layer

Eqs. (21)-(22) factorize $t_q^{(m)} \neq 0$:

$$t_q^{(m)} (C_1 + \frac{1}{2} \partial_{y'} C_1 c_{q,y'})|_{\vec{r}_N^{(1)}} = t_q^{(m)} (C_2 - \frac{1}{2} \partial_{y'} C_2 c_{q,y'})|_{r_0^{(2)} = \vec{r}_N^{(1)} + \vec{c}_q} \ , \tag{39a}$$

$$t_q^{(m)} (-\mathcal{D}_1 + \mathcal{D}_1 \partial_{y'} C_1)|_{\vec{r}_N^{(1)}} = t_q^{(m)} (-\mathcal{D}_2 + \mathcal{D}_2 \partial_{y'} C_2)|_{r_0^{(2)} = \vec{r}_N^{(1)} + \vec{c}_q} \ . \tag{39b}$$

Eqs. (39) with Eq. (37) satisfy the system with the *mid-grid* interface for all straight-interface cut links; then $\partial_{y'} P_k = p_1^{(k)} = p_1^{(k,ex)}$ and Eq. (38) is exact for any diffusion-weight $t_q^{(m)}$ in Eq. (2) and any $\{\Lambda_k\}$ in Eq. (3).

4.1.4. The diagonal system with the d2Q5: no A-layer, no B-layer

The d2Q5 keeps the piece-wise linear solution (37) because it satisfies Eq. (39) on the vertical and horizontal diagonal-interface cut links [see Fig. 2]. Their four interface equations are equivalent for $-x$ and y axes; the solution reads: $p_0^{(1)} = p_0^{(2)}$, $p_1^{(1)} = \frac{H_2(\phi_2 - \phi_1)}{H_2 \phi_1 + H_1 \phi_2}$, $p_1^{(2)} = \frac{-H_1(\phi_2 - \phi_1)}{H_2 \phi_1 + H_1 \phi_2}$. Since $h_2'/H_2 = h_1'/H_1$, the d2Q5 solution coincides with Eq. (35) and Eq. (38) is kept exact.

Further, although one might suggest that the (diagonally-rotated) d2Q5$^{(r)}$ model replaces the d2Q5 in the diagonal orientation, this is only partially true. Indeed, thanks to symmetry, there is no either A-layer or B-layer in d2Q5$^{(r)}$ because only one diagonal link is cut and its "mass" should be equal to zero [Eqs. (11), (A.5b)]. However, the d2Q5$^{(r)}$ handles Eq. (1) through the two separate sub-diagonals: $n_k = 2m$ and $n_k = 2m+1$, $m = 0, 1, 2, \ldots$; the two sub-diagonals are inter-connected only providing that H_1 and H_2 are of the different parity. This known d2Q5$^{(r)}$ "checkerboard" effect persists in all heterogeneous periodic configurations considered below, and it makes the d2Q5$^{(r)}$ unsuitable for practical purpose. Although the d2Q5$^{(r)}$ effective solutions have been constructed for validation purpose, they will not be considered hereafter.

4.1.5. The diagonal system with the d2Q9: the A-layer + the B-layer

If we assume that the d2Q9 maintains the linear profile $C_k = p_0^{(k)} + p_1^{(k)} y'$, Eq. (39) locates the interface midway the cut links; its location is hence shifted by $\frac{\sqrt{2}}{4}$ for $\{\vec{c}_y, \vec{c}_x\}$, on the one side, and $\vec{c}_\perp$, on the other side [see Fig. 2, dashed (black) and dotted (red), respectively]. The accommodation is introduced to cure of this mismatch. Solution to Eq. (26) is then looked for in the form of Eq. (25) and it reads with the help of Eqs. (19) and (20):

$$C_k(n) = P_k(n) + A_k(n) \ , \ P_k(n) = p_0^{(k)} + p_1^{(k)} y' \ , \ y'(n) = \frac{\sqrt{2}}{2}(n + \frac{1}{2}) \ , \tag{40a}$$

$$A_k(n) = \sum_{j=1} a_j^{(k)} [r_j^{(k)}]^{n_k} \ , \ \hat{A}_q^{+(k)}(n) = \sum_{j=1} \hat{a}_{q,j}^{(k)} [r_j^{(k)}]^{n_k} \ , \ k = 1, 2 \ . \tag{40b}$$

Thanks to the symmetry between the y and $-x$ axes, the system obeys (see also Eq. (B.4)):

$$\hat{n}_x^{\pm(l,k)} = \pm\hat{n}_y^{\pm(l,k)} \ , \ l = \{p, a\} \ , \ \text{ and } \ \hat{B}_x^{\pm(k)} = \pm\hat{B}_y^{\pm(k)} \ , \ \hat{B}_\perp^{\pm(k)} = -2\hat{B}_y^{\pm(k)} \ . \tag{41}$$

The solvability equation is quartic and $r = \cup_{j=1}^{4}\{r_j^{(k)}(t_q^{(m)}, \Lambda)\}$ obeys (Appendix A.1):

$$\begin{aligned} ar^4 \ &+ \ br^3 + cr^2 + dr + e = 0 \ , \ \text{ with } \ a = e = (-1 + 4\Lambda)(1 + 6t_c^{(m)}) \ , \\ b \ &= \ d = -4(1 - 2t_c^{(m)}) \ , \ c = -2(3 + 2t_c^{(m)} + 4\Lambda(1 + 6t_c^{(m)})) \ . \end{aligned} \tag{42}$$

The four roots of Eq. (42) are fixed by Λ and $t_c^{(m)}$; they are real for any weight-value $t_c^{(m)}$ only when $\Lambda > \frac{1}{4}$ [see Eq. (A.7) and Fig. 3]. Eqs. (23) and (24) reduce to the 6×2 closure conditions thanks to symmetry. Solution is fixed with six unknowns per phase k: $\{p_0^{(k)}, p_1^{(k)}\}$ and the four coefficients $\{a_j^{(k)}\}$. The system is hence satisfied without any help of B-layer. Fig. 4 displays the constructed solution: the A-layer component $A(n)$, the difference of the effective piece-wise linear profile with its exact solution, $P(n) - P^{(ex)}(n)$, and the difference of the whole solution with the exact profile, $C(n) - P^{(ex)}(n)$. This total difference is exactly validated on the normalized numerical solution, together with the predicted solution for $\mathcal{D}_{eff}$ and the post-collision distribution. Thereby, we stress that the A-layer modifies the gradient of the piece-wise linear profile: $p_1^{(k)} \neq p_1^{(k,ex)}$.

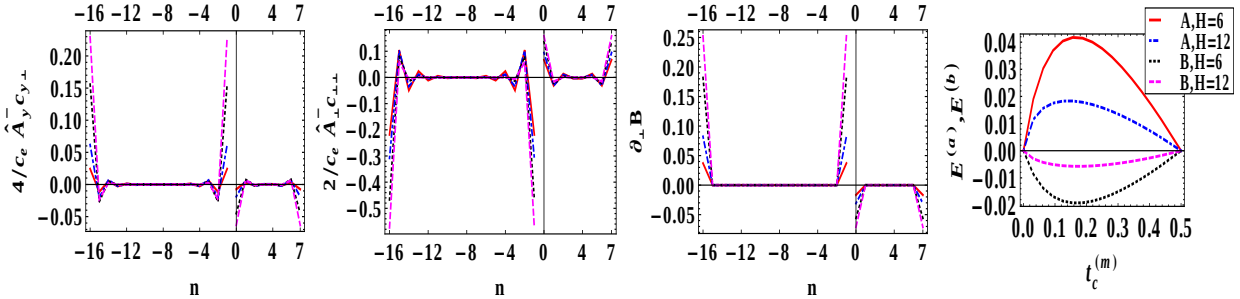

Figure 5: The pure diffusion process through the diagonal layers [$r_\phi = \frac{1}{4}$, $r_h = 2$, $c_e = r_\phi/4$, $H = 24$, $\Lambda = \frac{1}{4}$]. The non-equilibrium contribution to the local gradient $\partial_\perp C(n)$ [$\vec{1}_{z'} = \vec{1}_{y'} = \vec{1}_\perp$] in Eq. (31) from the A-layer (a) on the coordinate links x and y, $\frac{2\times 2}{c_e}\hat{A}_y^{-(k)} c_{\perp,\perp}$, with $\hat{A}_x^{-(k)} = \hat{A}_y^{-(k)}$ and (b), on the diagonal link: $\frac{2}{c_e}\hat{A}_\perp^{-(k)} c_{\perp,\perp}$; (c) the whole contribution from the B-layer. legend (a)-(c): $t_c^{(m)} = \{\frac{1}{16}, \frac{1}{8}, \frac{1}{4}, \frac{1}{3}\}$ [solid(red), dot-dashed(blue), dotted (black), dashed (magenta)]. (d) the contribution to $\mathcal{D}_{eff}$ from the A-layer ($\mathrm{E}^{(a)}$) and the B-layer ($\mathrm{E}^{(b)}$) versus $t_c^{(m)}$ when $H = 6$ and $H = 12$.

When $\Lambda = \frac{1}{4}$, Eq. (42) reduces to the quadratic equation with $a = e = 0$:

$$-(1+r)^2 + 2(-1+r)^2 t_c^{(m)} = 0 \ , \ r^\pm = \frac{2t_c^{(m)} + 1 \pm 2\sqrt{2t_c^{(m)}}}{2t_c^{(m)} - 1} \ , \ r^+ r^- = 1 \ , \ r^\pm < 0 \ , \ t_c^{(m)} \in]0, \frac{1}{2}[\ . \tag{43}$$

Eq. (43) degenerates when $t_c^{(m)} = \frac{1}{2}$ [d2Q5] or $t_c^{(m)} = 0$ [d2Q5$^{(r)}$]. The two roots to Eq. (43) are displayed in Fig. 3. The number of unknowns $\{p_0^{(k)}, p_1^{(k)}, a_1^{(k)}, a_2^{(k)}\}$ reduces to the 4×2. The 6×2 closure equations are then satisfied thanks to the 2×2 B-layer interface values $\hat{B}_x^{+(k)} = \hat{B}_y^{+(k)}$ [Eq. (41)]. Further inspection confirms that the A-layer and B-layer maintain the diffusion scaling: $\{\hat{P}_q^-, \hat{A}_q^-, \hat{B}_q^-\} \propto c_e$, and they are independent of Λ_k^-. It follows that when $\mathcal{D}_{eff}$ is derived with Eqs. (30b), (31), the relative coefficient D_r in Eq. (36b) and $\mathrm{E}(\mathcal{D}_{eff})$ from Eq. (32) remain independent of $\mathcal{D}_0$. Fig. 5 displays the accommodation contributions to $\partial_{y'} C_k(n)$ [Eq. (31) with $\vec{1}_{z'} = \vec{1}_{y'}$] and to $\mathrm{E}(\mathcal{D}_{eff})$ [$\mathrm{E}^{(a)}$, $\mathrm{E}^{(b)}$ from Eq. (32)]. The two corrections $\mathrm{E}^{(a)}$ and $\mathrm{E}^{(b)}$ non-linearly depend on the diffusion-weight $t_c^{(m)}$, and they vanish in the d2Q5 and d2Q5$^{(r)}$. In our example, $|\mathrm{E}^{(a)}|$ exceeds $\mathrm{E}^{(b)}$ by a factor of two and the two contributions have opposite signs. This tells us that the two contributions are quite comparable. Fig. 6 demonstrates that $\mathrm{E}^{(a)}$ and

$\mathrm{E}^{(b)}$ decay linearly with the space resolution. The first-order convergence is also observed in the piece-wise linear gradient: $\mathrm{E}(\partial_{y'}P) = |p_1^{(k)}/p_1^{(k,ex)} - 1|$. The $\mathrm{E}(\mathcal{D}_{eff})$ sums the three contributions in Eq. (32) and also converges only with first-order rate.

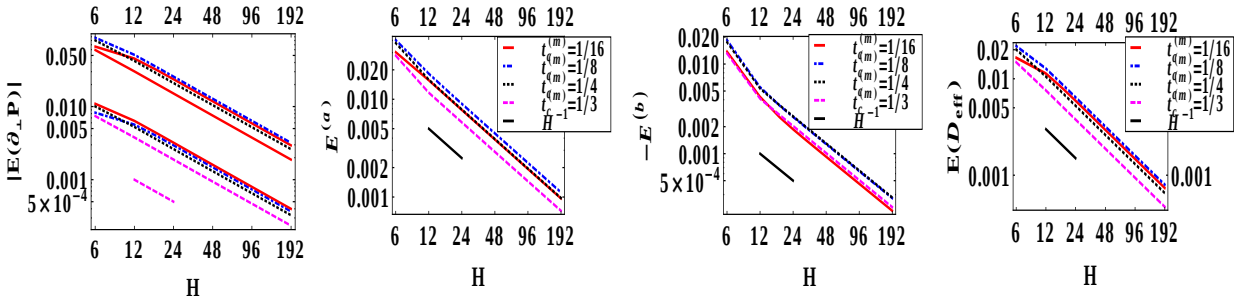

Figure 6: The pure diffusion process through the diagonal layers [$r_\phi = \frac{1}{4}$, $r_h = 2$, $c_e = r_\phi/4$, $\Lambda = \frac{1}{4}$]. The contributions to error-estimate $err(\mathcal{D}_{eff})$ in Eq. (32) versus $H = 6 \times 2^n$, $n \in [0, 7]$. (a) from the linear profile: $|\mathrm{E}(\partial_{y'}P)| = |p_1^{(k)}/p_1^{(k,ex)} - 1|$ with Eq. (35) in two phases $k = 1, 2$; (b) from the A-layer: $\mathrm{E}^{(a)}$; (c) from the B-layer: $\mathrm{E}^{(b)}$; (d) the total error $\mathrm{E}(\mathcal{D}_{eff})$; (a)-(d): $t_c^{(m)} = \{\frac{1}{16}, \frac{1}{8}, \frac{1}{4}, \frac{1}{3}\}$ [solid(red), dot-dashed(blue), dotted (black), dashed (magenta)]. The d2Q5 is exact.

4.1.6. Resume

The piece-wise linear scalar-profile and the effective-diffusivity $\mathcal{D}_{eff}$ are exact with any diffusion-weight $\{t_q^{(m)}\}$ in the straight heterogeneous layers. However, only the d2Q5 is exact in the diagonal system. The d2Q5$^{(r)}$ piece-wise linear profile is sub-divided on the two sub-diagonals, depending on the system parity. With the exception of these two models, the A-layer [Eq. (40b)] is excited in the diagonal pure-diffusion system without B-layer, unless when $\Lambda = \frac{1}{4}$. The A-layer is built on the four roots $\{r_j(t_q^{(m)}, \Lambda\}$ to Eq. (42). When $\Lambda = \frac{1}{4}$, the A-layer is built with the two roots (43) and complemented by the B-layer from Eq. (18c) in the interface nodes. A key point is that the A-layer and B-layer modify the gradient of the piece-wise linear profile $\partial_{y'}P_k$. On top of that, the A-layer and the B-layer impact the local gradient $\partial_{y'}C(y')$ directly in Eq. (31). The $\mathcal{D}_{eff}^{(num)}$ then converges to its exact (harmonic mean) value only with first-order rate; its dependency upon $\{t_q^{(m)}\}$ and Λ is non-trivial. The mass-source weight $\{t_q^{(M)}\}$ is irrelevant in the constructed solution because $M_k \equiv 0$.

4.2. The Darcy flow through the heterogeneous layers

We consider Eq. (34) with the interface-perpendicular Darcy flow $\vec{u} = u_\perp \vec{1}_{y'}$, M_k is then piece-wise constant. The $\mathcal{D}_{eff}$ is complemented with the Péclet dependent Taylor dispersion coefficient $\mathcal{D}_T = k_T \mathcal{D}_{eff}$ in Eq. (30c). The solution for $\mathcal{D}_T$, skewness and kurtosis is derived [33] with exact solution $C_k(y') = P_n^{(k)}(y') + P_{n-1}^{(k)}(y') e^{\frac{u_\perp y'}{\mathcal{D}_0 \phi_k}}$, where $P_n^{(k)}$ are the $n-$order polynomials, $n = \{1, 2, 3\}$ respectively. The d2Q5 "straight" solution [34] then becomes expressed through the discrete-exponential branches, as $C_k(y') = P_n^{(k)}(y') + P_{n-1}^{(k)}(y') r^{Pe_\perp^{(k)} y'}$, where r solves Eqs. (12)-(13) and the polynomials are fixed by the solvability and interface conditions. We construct the d2Q9 solution in the form of Eqs. (40)-(41) in the full weight-parameter space $\{t_q^{(m)}, t_q^{(m)}, t_q^{(M)}\}$ for two configurations depicted in Fig. 2. The piece-wise linear isotropic term $P_k(n) = p_0^{(k)} + p_1^{(k)} y'$ satisfies the scheme with $p_1^{(k)} = \frac{M_k}{u_\perp}$; the *anisotropic* discrete-exponential component is built in Appendix A.2 with the straight and diagonal configurations.

4.2.1. The straight system with the d2Q9: the B-layer

The "(a)" component of Eq. (28a) is weight-independent and it reduces to the quadratic equation:

$$\theta = 0 \quad : \; 2(-1+r)^2 - (-1+r^2) Pe_\perp^{(k)} = 0 \; , \; r = \{1, r_k\} \; . \tag{44}$$

Hence, Eq. (40) reads with the non-trivial root r_k to Eq. (44):

$$C_k(n) \quad = p_0^{(k)} + p_1^{(k)} n + a_1^{(k)} r_k^{n_k} \ , \ p_1^{(k)} = \tfrac{M_k}{u_\perp} \ , \ r_k = \tfrac{1+Pe_\perp^{(k)}/2}{1-Pe_\perp^{(k)}/2} \ . \tag{45}$$

Eq. (45) solves Eq. (34a) in the discrete form [with $y' = y$]:

$$u_\perp \bar{\Delta}_{y'} C_k(y') - M_k \quad = \quad \phi_k \mathcal{D}_0 \bar{\Delta}_{y'}^2 C_k(y') \ . \tag{46}$$

Eq. (46) reads with: $\bar{\Delta}_{y'}\psi = 2\sum_{q=1}^{Q_m/2} t_q \bar{\Delta}_q \psi(y') \cdot c_{q,y'}$ and $\bar{\Delta}_{y'}^2\psi = 2\sum_{q=1}^{Q_m/2} t_q \bar{\Delta}_q^2 \psi(y') c_{q,y'}^2$, and it fits Eq. (12) with $\mathcal{E} = 0$. Eqs. (45)-(46) are valid for any weights. Hence, in the straight geometry, $A_k = a_1^{(k)} r_k^n$ expresses the physical solution. Further, when the weights are all the same, $t_q^{(m)} = t_q^{(a)} = t_q^{(M)}$, Eqs. (21)-(22) factorize them for all links. Otherwise, the system is accommodated by the B-layer from Eq. (B.2); it complements Eq. (16) in the d2Q9 scheme. Due to symmetry: $\hat{B}_\parallel^{+(k)} = \hat{B}_\perp^{+(k)} = -\frac{1}{2}\hat{B}_y^{+(k)}$, the B-layer is fixed with the two coefficients of $\hat{B}_y^{+(k)}$ per phase. Together with $\{p_0^{(k)}, a_1^{(k)}\}$, they are derived from the set of the 4×2 interface conditions. The B-layer does not affect $\partial_y C$ in Eq. (31) [here, $\vec{1}_{z'} = \vec{1}_y$]. The obtained scalar-field solution in Eq. (45) and $\mathcal{D}_T$ are weight-independent and the same as in d2Q5, [34].

4.2.2. The diagonal system with the d2Q5 and d2Q5$^{(r)}$: no A-layer, no B-layer

The solvability condition from Eq. (A.13) reads:

$$\text{d2Q5} \ : \ (4 - 4r + \sqrt{2} Pe_\perp^{(k)}(1+r))(4\Lambda(-1+r^2)^2 - (1+r^2)^2) = 0 \ , \tag{47a}$$

$$\text{d2Q5}^{(r)} \ : (2 - 2r^2 + \sqrt{2} Pe_\perp^{(k)}(1+r^2))(4\Lambda(-1+r)^2 - (1+r)^2)(1+r) = 0 \ . \tag{47b}$$

The five roots to Eq. (47) are:

$$\text{d2Q5} : \cup_{j=1}^5 r_j = r_1^{(k)} \cup r|_{\text{d2Q5}}^{(u=0)} \ , \ \text{ with } \ r_1^{(k)} = \frac{4 + \sqrt{2} Pe_\perp^{(k)}}{4 - \sqrt{2} Pe_\perp^{(k)}} \ , \tag{48a}$$

$$\text{d2Q5}^{(r)} \ : \cup_{j=1}^5 r_j = r_{1,2}^{(k)} \cup r|_{\text{d2Q5}^{(r)}}^{(u=0)} \cup \{-1\} \ , \ r_{1,2}^{(k)} = \pm\sqrt{\frac{2 + \sqrt{2} Pe_\perp^{(k)}}{2 - \sqrt{2} Pe_\perp^{(k)}}} \ . \tag{48b}$$

The $r_j = r_1^{(k)}$ and $r_j = \{r_{1,2}^{(k)}\}$ are the physical roots and they vanish the term of $(\Lambda - \frac{1}{4})$ in Eq. (13); Eq. (12) is then solved with $\mathcal{E} = 0$ because the mass-source is piece-wise constant. The pure-diffusion roots $r|_{\text{d2Q5}}^{(u=0)}$ and $r|_{\text{d2Q5}^{(r)}}^{(u=0)}$ solve Eqs. (A.8a) and (A.9a); they are given in Eqs. (A.8b) and (A.9b), respectively. The two models do not need any accommodation. The d2Q5 maintains $\hat{n}_q^+(y')$ in the form of Eq. (16), and it extracts $\{p_0^{(k)}, a_1^{(k)}\}$ from the 2×2 Eqs. (23b) and (24b) to an additive constant. The d2Q5$^{(r)}$ produces their individual solutions on the two sub-diagonals and remains unsuitable.

4.2.3. The diagonal system with the d2Q9: the A-layer + the B-layer

When $\Lambda \neq \frac{1}{4}$, the solvability condition is given by the six order (sextic) polynomial equation; when $\Lambda = \frac{1}{4}$, the solvability equation is quartic. In the two cases, one root is equal to one, the reduced quintic (fifth-order) and cubic equations are given by Eqs. (A.13) and (A.14a), respectively. Eq. (40) reads:

$$\theta = \frac{\pi}{4} \quad : \quad C_k(n) = p_0^{(k)} + p_1^{(k)} n + \sum_{j=1}^{N} a_j^{(k)} r_j^n \ , \ r_j = r_j^{(k)}(t_q^{(a)}, t_q^{(m)}, \Lambda_k, Pe_\perp^{(k)}) \ , \tag{49}$$

with $N|_{\Lambda \neq \frac{1}{4}} = 5$ and $N|_{\Lambda = \frac{1}{4}} = 3$. The set $\{r_j\}$ is composed of the one physical root and the four or two A-layer roots, respectively. The A-layer has the same number of roots as in pure diffusion [cf. Eqs. (42)-(43)], but they depend upon the two weight families, Λ_k and $Pe_\perp^{(k)}$. The set of three roots to Eq. (A.14a) is illustrated in Fig. 7; the contour plot of Eq. (A.14b) bounds their real domain.

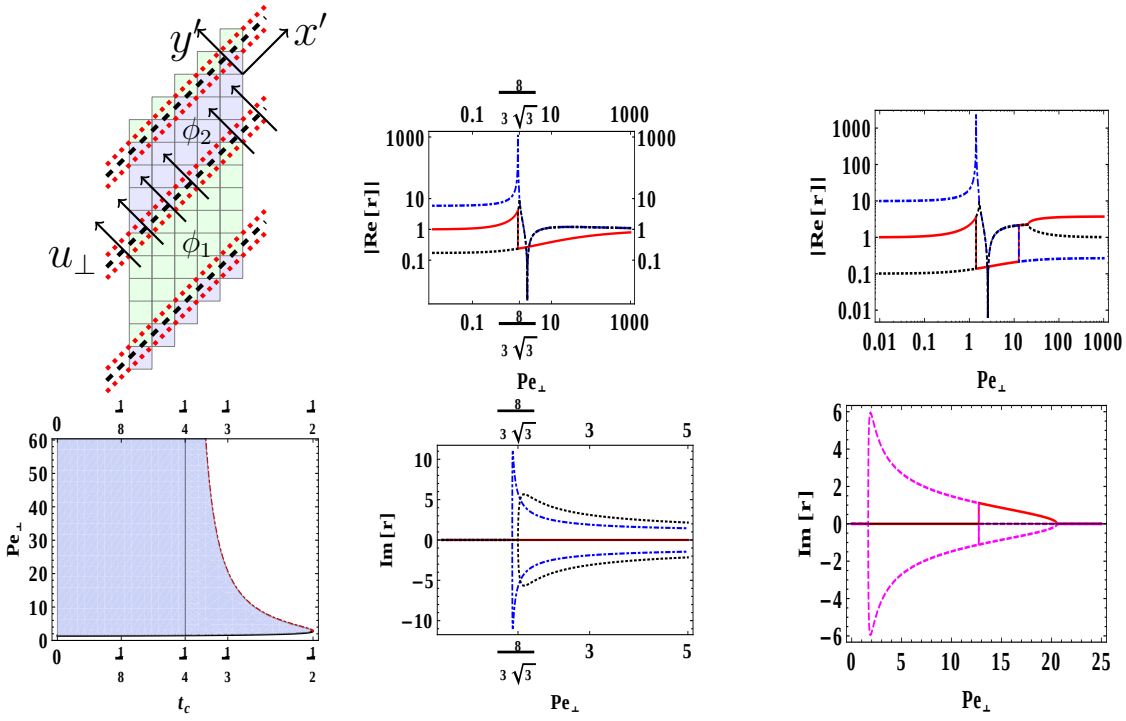

Figure 7: (a) The interface-perpendicular Darcy flow through the diagonal layers. The three A-layer roots from Eq. (A.14a) when $\Lambda = \frac{1}{4}$ and all weights are identical. Top row: (b) and (c): the three roots $\{r_j\}$ versus $\mathrm{Pe}_\perp$; the "physical" root is $r|_{\mathrm{Pe}_\perp=0} = 1$ [solid (red)]. (b) $|\mathscr{R}[r]|$ when $t_c = \frac{1}{4}$ [$Pe_\perp^{min}(\frac{1}{4}) = \frac{8\sqrt{3}}{3}$]. (c) $|\mathscr{R}[r]|$ when $t_c = \frac{1}{3}$ [$Pe_\perp^{min}(\frac{1}{3}) \approx 1.65$, $Pe_\perp^{max}(\frac{1}{3}) \approx 20.57$]. Bottom row: (d) region plot $\mathrm{Pe}_\perp \in \{Pe_\perp^{min}(t_c), Pe_\perp^{max}(t_c)\}$, Eq. (A.14b), all three roots are real outside of the shaded area, $t_c^{(a)} \in [0, \frac{1}{2}]$ && $(\mathrm{Pe}_\perp < Pe_\perp^{min}(t_c))$, and $t_c \in [\frac{1}{4}, \frac{1}{2}]$ && $(\mathrm{Pe}_\perp > Pe_\perp^{max}(t_c))$, with $Pe_\perp^{max}|_{t_c \to \frac{1}{4}} = \infty$. Inside the shaded area, only one root is real, e.g.: (e) $\pm\Im[r]$ when $t_c^{(a)} = \{\frac{1}{8}, \frac{1}{4}\}$ (dot-dashed (blue), dashed (black)); (f) $\pm\Im[r]$ when $t_c^{(a)} = \frac{1}{3}$.

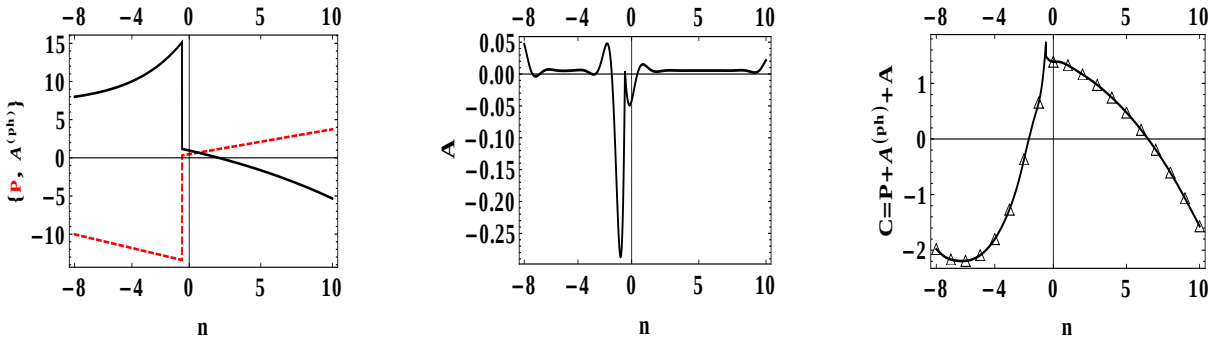

Figure 8: The normalized solution components in the interface-perpendicular Darcy flow through the diagonal layers. (a) the piecewise linear polynomial component $P(n)$ (dashed-red) and the physical exponent $A^{(ph)}(n)$ (solid-black). (b) the A-layer $A(n)$. (d) their sum $\mathcal{C}(n) = P + A^{(ph)} + A$ (solid) and the numerical solution (symbols); (a)-(d): phase 1: $n \in [-8, -\frac{1}{2}]$ and phase 2: $n \in [-\frac{1}{2}, 10]$. Data: $H = 19$, $r_h = 8/11$, $r_\phi = \frac{1}{4}$, $\phi_2 = 1$, $u_\perp/\mathcal{D}_0 = 10^{-1}$, $c_e = 10^{-1}$, $t_c = \frac{1}{4}$, $\Lambda = \frac{1}{4}$.

The coefficients are fixed by the closure conditions as in pure diffusion [see Sec. 4.1.5]. Fig. 8 displays the normalized components: (a) the linear $P_k(n)$ and the physical exponential branch $A^{(ph)}(n)$; (b) the A-layer $A(n)$; and (c), their sum $\mathcal{C}(n)$ which coincides with the numerical solution. Similar solutions are constructed and validated when $\Lambda \neq \frac{1}{4}$.

4.2.4. The dispersion coefficient in the interface-perpendicular flow

The dispersion coefficient $\mathcal{D} = \mathcal{D}_{eff}(1+k_T)$ sums $\mathcal{D}_{eff}(r_\phi, r_h)$ from Eq. (36b) and $\mathcal{D}_T = \mathcal{D}_{eff}k_T(r_\phi, r_h, \mathrm{Pe})$ [k_T is derived in [33], Eq.(58) there]. The k_T converges to the finite value $k_T(r_\phi, r_h) = \frac{r_h(r_\phi^2-1)^2}{r_\phi(1+r_h r_\phi)^2}$ when $\mathrm{Pe} \to \infty$, and k_T vanishes when $\mathrm{Pe} \to 0$, then $\mathcal{D} \to \mathcal{D}_{eff}$. The three normalized coefficients, $\mathcal{D}_0^{-1}\mathcal{D}_{eff}$, k_T and $\mathcal{D}_0^{-1}\mathcal{D}$ are illustrated in Fig. 9. The symbolic and numerical procedures compute $\mathcal{D}_{eff}^{(num)}$ with

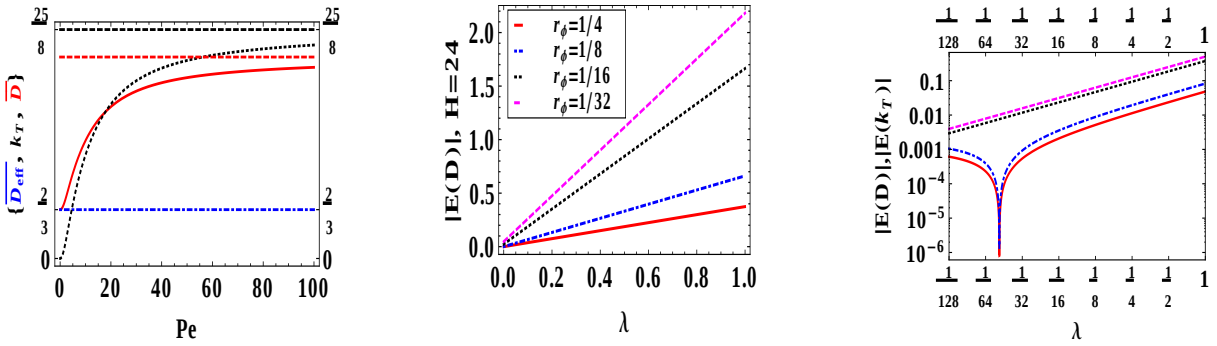

Figure 9: The interface-perpendicular Darcy flow when $r_h = 2$, $r_\phi = \frac{1}{4}$ [(a) and (c)]. a) The predicted transport coefficients versus Pe: $\overline{\mathcal{D}_{eff}} = \mathcal{D}_0^{-1}\mathcal{D}_{eff}(r_\phi, r_h) = \frac{2}{3}$ [Eq. (36b), dot-dashed(blue)], $k_T = \mathcal{D}_{eff}^{-1}\mathcal{D}_T(\mathrm{Pe})$ with its asymptotic $\lim_{\mathrm{Pe}\to\infty} k_T = \frac{25}{8}$ [dotted (black)], and $\bar{\mathcal{D}} = \mathcal{D}_0^{-1}\mathcal{D}$ with its asymptotic [solid (red)]. (b) and (c): identical error-estimate is produced by the d2Q9 [$\theta = 0$] and the d2Q5 [$\theta = \frac{\pi}{4}$] with Eq. (50); (b) |E(D)| versus λ [$H = 24$, $\mathrm{Pe} = 100$] when $r_\phi = \{\frac{1}{4}, \frac{1}{8}, \frac{1}{16}, \frac{1}{32}\}$ [solid(red), dot-dashed(blue), dotted (black), dashed (magenta)]. (c) |E(D)| and |E(k_T)| versus λ at $\mathrm{Pe} = 10$ [solid(red), dot-dashed(blue)] and $\mathrm{Pe} = 100$ [dotted (black), dashed (magenta)].

Eq. (30b) using Eq. (31) for $\partial_{y'}C_k(n)$, and $\mathcal{D}_T^{(num)} = k_T^{(num)}\mathcal{D}_{eff}$ with Eq. (30c); the two relative errors, $\mathrm{E(D)} = \mathcal{D}^{(num)}/\mathcal{D} - 1$ and $\mathrm{E}(k_T) = k_T^{(num)}/k_T - 1$, are examined. In the straight system, the k_T and $\mathcal{D}_{eff}$ are weight-independent together with the C_k and $\partial_y C_k$, respectively; they are weight-dependent in the diagonal system. The two following dependencies $\Lambda(c_e)$ parametrize any one-dimensional system through a free-tunable parameter λ, and they produce identical error-estimates in the straight [d2Q9] and the diagonal [d2Q5] layers:

$$\text{d2Q9}\ ,\ \theta = 0\ :\ \Lambda_k = \Lambda^{(0,Q9)} = \frac{\lambda}{1-c_e}\ , \tag{50a}$$

$$\text{d2Q5}\ ,\ \theta = \frac{\pi}{4}\ :\ \Lambda_k = \Lambda^{(\frac{\pi}{4},Q5)} = \frac{\lambda}{1-2c_e}\ ,\ c_e \in]0, \frac{1}{2}]\ , \tag{50b}$$

$$\text{then}\ \ \mathrm{E(D)}|_{\theta=0} = \mathrm{E(D)}|_{\theta=\frac{\pi}{4}}\ ,\ \mathrm{E}(k_T)|_{\theta=0} = \mathrm{E}(k_T)|_{\theta=\frac{\pi}{4}}\ ,\ \forall\ \{r_\phi\ ,\ r_h\ ,\ \mathrm{Pe}\}\ \text{ and }\ \forall\lambda > 0\ . \tag{50c}$$

Recall, the TRT steady-state bulk solutions are fixed by Pe, the aspect ratios and Λ on the given grid; they are hence the same for any $u_\perp$ and $\Lambda^- = \mathcal{D}_0/c_e$ when Pe and c_e is fixed. Using Eq. (50), the macroscopic solution $\mathcal{C}(y')$ becomes independent of the diffusion-scale parameter c_e, but it depends on λ. Plugging Eqs. (50a) [$\theta = 0, c_{qy'}^2 = 1$] and (50b) [$\theta = \frac{\pi}{4}$, $c_{qy'}^2 = \frac{1}{2}$] with $\lambda = \frac{1}{4}$ into Eq. (13), the two first terms are summed and $\mathcal{E}(y')$ vanishes for any mass term $M(y')$ when $t_q^{(m)} = t_q^{(M)}$; otherwise, when $M(y')$ is piece-wise linear (constant) [our example alike]. Fig. 9 demonstrates that E(D) and E(k_T) scale linearly with λ; their amplitudes grow with the porosity contrast and Pe. Fig. 10 [first diagram] shows that when Λ and c_e are fixed to the same values when $\theta = 0$ and $\theta = \frac{\pi}{4}$, their solutions are distinct because Eq. (50) is not satisfied; the straight solution is slightly more accurate within the examined parameter range; the accuracy degrades

with λ but the error-estimates all converge with second-order rate. Fig. 10 [second diagram] displays the predicted d2Q9 solutions for E(D) and E(k_T) versus $t_c \in]0, \frac{1}{2}]$ with $\Lambda = \frac{1}{4}$ and Pe $= \{10, 100\}$. This symbolic estimate shows that E(D) and E(k_T) increase with Pe for all weight values; the d2Q5 remains the most accurate. The two last diagrams in Fig. 10 extend these results to $\Lambda = \frac{1}{6}$ and examine the error convergence at fixed Pe when $t_c = \{\frac{1}{3}, \frac{1}{4}\}$, decreasing $u_\perp$ with H; the second-order d2Q5 error-estimate is plotted together. The numerical and symbolic results coincide in the coarse resolution; the asymptotic behaviour is then established with the help of the numerical simulations. The coarse-grid second-order d2Q9 rate is followed by the asymptotic, first-order convergence. Asymptotically, the d2Q5 with $\Lambda = \frac{1}{6}$ is much more accurate than d2Q9; otherwise, the d2Q9 with $t_c = \frac{1}{3}$ and $\Lambda = \frac{1}{6}$ is slightly more accurate among the four examined full-stencil parameter combinations.

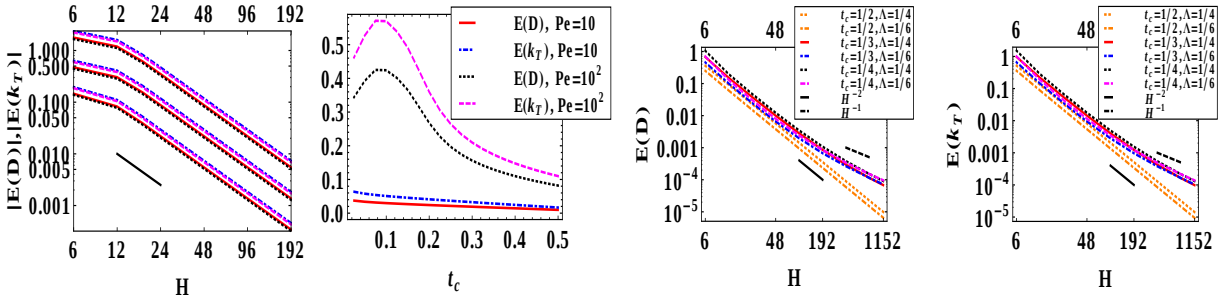

Figure 10: The interface-perpendicular Darcy flow. (a) |E(D)| [solid(red), dotted (black)] and E(k_T) [dot-dashed(blue),dashed (magenta)] versus H are displayed together for $\theta = 0$ [d2Q9] and $\theta = \frac{\pi}{4}$ [d2Q5] at Pe $= 10^2$, the three groups apply $\Lambda = \{\frac{1}{16}, \frac{1}{4}, 1\}$ from the bottom to the top: the convergence rate is H^{-2}. (b)-(d): the diagonal layers. (b): E(D) and E(k_T) versus $t_c \in]0, \frac{1}{2}]$ when $\Lambda = \frac{1}{4}$ and $H = 24$, Pe $= 10$ (the two bottom lines) and Pe $= 10^2$ (the two upper lines); (c) and (d): E(D) and E(k_T) when $t_c = \{\frac{1}{2}, \frac{1}{3}, \frac{1}{4}\}$ with $\Lambda = \frac{1}{4}$ [dotted(orange), solid(red), dashed (magenta)] and $\Lambda = \frac{1}{6}$ [dot-dashed (orange), dot-dashed (blue), dotted (black)]. The H^{-2} asymptotic rate is only produced by the d2Q5 [$t_c = \frac{1}{2}$]. (a)-(d): $r_h = 2$, $r_\phi = \frac{1}{4}$, $c_e = r_\phi/4$, $\phi_2 = 1$. (c) and (d): Pe $= 24$, $|u_\perp| = \frac{1}{8} \times 2^{-m}$ when $H = \{6 \times 2^m, m \in [0, 7]\}$, with $H^{max} = 18 \times 2^7$, $\Lambda^- = 1$.

4.2.5. Resume

When the series of the heterogeneous blocks is aligned with the *coordinate* axis and the weight families are distinct, $t_q^{(m)} \neq t_q^{(a)}$, the B-layer accommodates the d2Q9 solution in the interface-perpendicular Darcy flow. However, the B-layer does not impact the scalar field $\mathcal{C}(n)$, the effective-diffusivity or the Taylor dispersion coefficient; they remain weight-independent and the same as with the d2Q5. In the diagonal channels, the A-layer complements the physical exponential mode; the whole system is built with the five roots to Eq. (A.13) [when $\Lambda \neq \frac{1}{4}$]; otherwise, with the three roots to Eq. (A.14a), assisted by the B-layer. The base roots $\{r_j\}$ depend upon the advection and diffusion weights $\{t_q^{(m)}, t_q^{(a)}\}$, Λ_k and the local Péclet number $Pe_\perp^{(k)}$. Hence, the physical root is also weight- and rotation-dependent, meaning that it is different with the d2Q5 and d2Q5$^{(r)}$, Eq. (47). In these two models, the remaining [accommodation] roots are the same as in the pure diffusion, and they are not excited, unless when the mass-source weight $t_q^{(M)}$ differs from the two other weights. This methodological configuration is exemplified in Appendix A.2.

The parametrization by the governing numbers, physical Péclet and collision Λ, is more complicated in the ADE than in flow models [42, 45]; that is because the kinematic viscosity $\nu = \frac{1}{3}\Lambda^+$ is fixed by Λ^+ but $\mathcal{D}_0 = c_e\Lambda^-$ depends upon two free-tunable parameters. In any one-dimensional evolution process without A-layer, the d2Q9 [$\theta = 0$] and d2Q5 [$\theta = \frac{\pi}{4}$] produce c_e-independent scalar-field provided that Λ and c_e are inter-related, as $\Lambda = \lambda/(1 - c_e)$ and $\Lambda = \lambda/(1 - 2c_e)$, respectively. The relative error-estimates, E(D) and E(k_T), then converge with second-order rate; they reduce linearly to zero with λ thanks to reduction of the leading-order corrections in the interface-continuity relations when $\Lambda \to 0$. However, the asymptotic d2Q9 rate reduces to the first-order in the diagonal system thanks to A-layer, even when the three weight families are all the same. The solution remains parametrized by Pe and Λ, but it depends upon c_e at fixed value of $\mathcal{D}_0$. Hence, the A-layer delays the solution convergence and discards its parametrization $\Lambda(c_e)$.

5. Parallel heterogeneous system

Consider two stratified porous layers $\phi = \{\phi_1, \phi_2\}$, periodic along the $x'-$axis with $\vec{u} = u_{x'}\vec{1}_{x'}$ given by

$$\begin{aligned} u_{x'}(y') &= u_{\parallel}\ ,\ y' \in [-h_1', 0]\ ,\ \phi = \phi_1\ , \\ u_{x'}(y') &= u_{\parallel} - \frac{1}{2}\Psi y'(y' - h_2')\ ,\ y' \in [0, h_2']\ ,\ \phi = \phi_2\ . \end{aligned} \tag{51}$$

Solution to Eq. (4) is translation-invariant along the velocity direction $\vec{1}_{x'}$. Since the flow is complanar with the interface $[\vec{1}_{z'} = \vec{1}_{x'}]$, the advective-diffusive flux is continuous in Eq. (6b) $[||\vec{n}\cdot\vec{J}_k|| = 0]$ and the effective diffusivity in Eq. (30c) should reduce to $\mathcal{D}_0$ on the numerical solution. Eq. (51) is applied in three configurations: (i) the system is periodic along the $y'-$axis and $u_{x'}(y') = u_{\parallel}$ ($\Psi = 0$) presents a constant Darcy flow; the open/porous system is either (ii) bounded [B-OPL] or (iii) periodic [OPL] along the $y'-$axis, where pure-diffusive layer ($\phi = \phi_1$, $u_{\parallel} = 0$, $\Psi = 0$) is adjacent with the Poiseuille flow ($\phi_2 = 1$, $u_{\parallel} = 0$). The B-OPL reduces to the Poiseuille channel when the porous layer vanishes ($h_1' = 0$). The coefficients of the Taylor dispersion, skewness and kurtosis are predicted for (i) OPL [68], (ii) stratified Darcy flow, (iii) Poiseuille channel and (iv) B-OPL (Secs. 5.2, 5.3 and C.4 [33], respectively). These exact solutions are employed [34] to examine the d2Q5 symbolic solutions. We extend them to d2Q9 in the straight and diagonal channels, and evaluate the transport coefficients $\mathcal{D}_{eff}$ and $\mathcal{D}_T$ in Eq. (30).

5.1. The truncation effect in polynomial solution component

The mass-source $M_k(y') = U_{x'}\phi_k - u_{x'}(y')$ in Eq. (4) is piece-wise constant with constant Darcy velocity and parabolic in the Poiseuille flow. Accordingly, $P_k(n)$ is either quadratic or quartic [Eq. (25a)], and $e_q^{-(p)}(y') = t_q^{(a)}P_k(y')u_{x'}(y')c_{qx'}$ is either quadratic or sextic [Eq. (2)]. Hence, according to Eq. (26), $\hat{P}_q^{+(k)}(y')$ is looked for as the first- and fifth-order polynomial, respectively:

$$\{P_1, P_2\} = \{\sum_{m=0}^{2} p_m^{(1)} y'^m, \sum_{m=0}^{4} p_m^{(2)} y'^m\}\ , \tag{52a}$$

$$\{\hat{P}_q^{+(1)}, \hat{P}_q^{+(2)}\} = \{\sum_{m=0}^{1} \hat{p}_{q,m}^{(1)} y'^m, \sum_{m=0}^{5} \hat{p}_{q,m}^{(2)} y'^m\}\ . \tag{52b}$$

The coefficients $\hat{p}_{q,m}(y')$ are expressed for four links $\vec{c}_q = \{\vec{c}_x, \vec{c}_y, \vec{c}_{\parallel}, \vec{c}_{\perp}\}$ from Eq. (26). Eq. (52b) is then substituted into Eq. (28) to derive $\{p_m^{(k)}\}$ for $m \geq 2$ (phase-index k is dropped):

$$p_2 = \frac{1}{12}(-6\psi' + \Psi'(-1 - 6\Lambda(-1 + c_e)))\ ,\ \psi' = \frac{M}{c_e\Lambda^-}\ ,\ \theta = \frac{\pi m}{2}\ ,\ m = 0, 1, \ldots \tag{53a}$$

$$p_2 = \frac{1}{12}(-6\psi' + \Psi'(-2 + 3t_c^{(m)} + 6\Lambda(2 - 3t_c^{(m)} - c_e)))\ ,\ \theta = \frac{\pi m}{4}\ ,\ m = 1, 3, \cdots \tag{53b}$$

$$p_3 = \frac{\Psi' h'}{12}\ ,\ \theta = \frac{\pi m}{4}\ ,\ m = 0, 1, \ldots\ ,\ p_4 = -\frac{\Psi'}{24}\ ,\ \forall\ \theta\ , \Psi' = \frac{\Psi}{c_e\Lambda^-}\ . \tag{53c}$$

Eq. (53) reduces to the parabolic profile $P(y')$ with $p_2 = \frac{-M}{2c_e\Lambda^-}$ in constant Darcy flow. Otherwise, when the mass-source is parabolic, p_2 depends upon the inclination, the diffusion-weight $\{t_c^{(m)}, t_d^{(m)}\}$ and Λ, thanks to the fourth-order truncation; p_2 is the same with $\theta = 0$ and $\theta = \frac{\pi}{4}$ only when the hydrodynamic weight $\{t_c^{(m)}, t_d^{(m)}\} = \{\frac{1}{3}, \frac{1}{12}\}$ is applied in the diagonal system. Additionally, p_2 depends on c_e because the mass-source is parabolic, unless when Λ and c_e are inter-related via Eq. (50a) [$\theta = 0$] or by Eq. (54) [$\theta = \frac{\pi}{4}$]:

$$\text{d2Q9}\ ,\ \theta = \frac{\pi}{4}\quad :\ \Lambda_k = \Lambda^{(\frac{\pi}{4}, Q9)} = \frac{\lambda}{2 - 3t_c^{(m)} - c_e}\ ,\ t_c^{(m)} \in [0, \tfrac{1}{2}]\ ,\ c_e \in]0, c_e^{max}(t_c^{(m)})]\ . \tag{54}$$

Eqs. (52b)-(53) determine $\mathcal{E}$ in Eq. (13), with $\mathcal{E}^{(p)}$ due to the polynomial component alone when $\theta = \frac{\pi}{4}$:

$$\text{d2Q9 , } \theta = 0 : \ \mathcal{E} = \alpha^{(0,Q9)} \bar{\Delta}_y^2 M(y) \ , \ \alpha^{(0,Q9)} = \frac{1}{4} - (1 - c_e)\Lambda \ ,$$
$$\mathcal{E} = 0 \quad \text{with} \ \ \Lambda = \Lambda^{(0,Q9)} \ \ \text{if} \ \ \lambda = \frac{1}{4} \ , \tag{55a}$$

$$\text{d2Q9 , } \theta = \frac{\pi}{4} : \ \mathcal{E}^{(p)} = \alpha^{(\frac{\pi}{4},Q9)} \bar{\Delta}_{y'}^2 M(y') \ , \ \alpha^{(\frac{\pi}{4},Q9)} = \frac{1}{4}(2 - 3t_c^{(m)}) - \Lambda(2 - 3t_c^{(m)} - c_e) \ ,$$
$$\mathcal{E}^{(p)} = 0 \quad \text{with} \ \ \Lambda = \Lambda^{(\frac{\pi}{4},Q9)} \ \ \text{if} \ \ \lambda = \frac{2 - 3t_c^{(m)}}{4} \ . \tag{55b}$$

The "optimal" $\Lambda(\lambda)$ values differ between the continuous case $-M(y') = c_e \Lambda^- \partial_{y'}^2 B(y')$ and the discrete case $-M(y') = c_e \Lambda^- \bar{\Delta}_y^2 M(y')$, both in the straight [cf. Eqs. (53a) and (55a)] and the diagonal cases [cf. Eqs. (53b) and (55b)], where $\lambda(t_c^{(m)} = \frac{1}{3}) = \frac{1}{6}$ and $\lambda(t_c^{(m)} = \frac{1}{3}) = \frac{1}{4}$, respectively, with Eq. (54).

5.2. The truncation effect in local gradient

We examine now how the parallel velocity $u_{x'}(y')$ affects the local gradient in the translation-invariant direction $\vec{1}_{x'}$, where one expects to get $\partial_{x'} P = 0$. Let us put aside the truncation term $(\Lambda - \frac{1}{4})\bar{\Delta}_q^2 \hat{n}_q^-$ in Eq. (10) and substitute into Eq. (31): $\hat{P}_q^-(y') = \nabla_q e_q^{+(p)}(y') - \Lambda^+ \bar{\Delta}_q^2 e_q^{-(p)}(y')$ with $t_q^{(m)} = t_q^{(M)}$, $e_q^{-(p)}(y') = t_q^{(a)} u_{x'}(y') P(y') c_{qx'}$, $\bar{\Delta}_q^2 \approx \partial_{y'}^2 c_{q,y'}^2$. Eq. (31) then gives:

$$\partial_{x'} P(y') := 2c_e^{-1} \sum_{q=1}^{Q_m/2} \hat{P}_q^-(y') c_{qx'} \approx \partial_{x'} P(y') + \Lambda^+ \partial_{x'} M^{(p)}(y') + \mathrm{E}^{(p,\nabla)}(y') \ , \tag{56a}$$

$$\mathrm{E}^{(p,\nabla)}(y') = -2c_e^{-1} \Lambda^+ \boxed{\partial_{y'}^2 (u_{x'} P(y'))} \sum_{q=1}^{Q_m/2} t_q^{(a)} c_{q,x'}^2 c_{q,y'}^2 \ . \tag{56b}$$

Eq. (56a) reads with $\partial_{x'} P(y') = 0$ and $\partial_{x'} M^{(p)}(y') = 0$ thanks to translation invariance. However, $\mathrm{E}^{(p,\nabla)}$ gives non-zero truncation correction; it is isotropic only with the hydrodynamic advection-weight, and it vanishes only in d2Q5 [$\theta = 0$] and d2Q5$^{(r)}$ [$\theta = \frac{\pi}{4}$]. Hence, when $u_{x'}(y')P(y')$ is the parabolic- or the higher-order polynomial, the local gradient-estimate $\partial_{x'} C(y')$ *is not equal to zero for solution-invariant direction.* Moreover, when $\partial_{y'}^2 u_{x'}(y') \neq 0$, e.g. in the parabolic profile (51), $\partial_{x'} P(y')$ depends on an additive constant [$p_0^{(k)}$ in Eq. (25a)]. These two artefacts modify the $\mathcal{D}_{eff}$, which is expected to be equal to zero according to Eq. (30b).

5.3. The straight system with the d2Q9

Recall that there is no A-layer in the straight layers, either in the pure diffusion or the interface-perpendicular flow [in this last case, the B-layer accommodates the solution when the weight families are distinct, Sec. 4.2.1]. There is no A-layer also in the interface-parallel flow, but the B-layer from Eq. (B.2) is exhibited with any weights except the d2Q5. Substituting $\hat{B}_y^{+(k)} = -(\hat{B}_\parallel^{+(k)} + \hat{B}_\perp^{+(k)})$, the B-layer coefficients $\{b_\parallel^{(+,k)}, b_\perp^{+(k)}, d_\parallel^{(+,k)}, d_\perp^{+(k)}\}$ are derived together with the $\{p_0^{(k)}, p_1^{(k)}\}$ from the whole closure system (21)- (22). When the three weight families are the same, the B-layer vanishes on the vertical link and $C(y')$ becomes weight-independent. It follows that $\mathcal{D}_T^{(num)}$ from Eq. (30c) is weight-independent, and hence the same as in d2Q5. This explains the numerical observation [34].

5.4. The diagonal system with the d2Q5

To be contrasted with the pure diffusion and the interface-perpendicular flow, the d2Q5 requires the B-layer in the parallel flow. To explain this point, consider the constant Darcy flow $\vec{u} = u_\parallel \vec{1}_{x'}$ where

$M_k(y')$ is piece-wise constant; $P_k(y')$ is parabolic and the polynomial solution to Eq. (10) coincides with the Chapman-Enskog expansion expressed through $c_{qx'} = \frac{\sqrt{2}}{2}(c_{q,x} + c_{q,y})$ and $c_{q,y'} = \frac{\sqrt{2}}{2}(c_{q,y} - c_{q,x})$:

$$\hat{P}_q^{-(k)} = t_q^{(m)} c_e \partial_{y'} P_k \boxed{-t_q^{(a)} \Lambda_k^+ u_\parallel \partial_{y'}^2 P_k c_{qx'} c_{q,y'}^2} , \tag{57a}$$

$$\hat{P}_q^{+(k)} = t_q^{(a)} u_\parallel \partial_{y'} P_k c_{qx'} c_{q,y'} - t_q^{(m)} \Lambda_k^- c_e \partial_{y'}^2 P_k c_{q,y'}^2 . \tag{57b}$$

The set $\{P_k, \hat{P}_q^{+(k)}\}$ satisfies Eq. (12) with $\mathcal{E} = 0$, then $-M_k = c_e \Lambda_k^- \partial_{y'}^2 P_k$. Making use of this equation in $e_q^{+(p,k)}$, the interface-continuity condition (8a) reads [with the weights $\{t_c, t_d\}$]:

$$||[t_c c_e (P_k + \frac{1}{2}\partial_{y'} P_k c_{q,y'} + \Lambda_k (1 - 2c_e) \partial_{y'}^2 P_k c_{q,y'}^2) \boxed{-\frac{1}{2} t_c \Lambda_k^+ u_\parallel \partial_{y'} P_k c_{qx'} c_{q,y'}^2)}||_{r_0^{(k)}} = 0 . \tag{58}$$

The last term in Eq. (58) has different signs for interface-cut coordinate links $c_{qx'} = c_{\bar{x}} = -1$ and $c_{q,y'} = c_y = 1$ [$c_{q,y'}^2 = \frac{1}{2}$ in d2Q5]. The B-layer with $\hat{B}_x^{\pm(k)}(n) = \mp \hat{B}_y^{\pm(k)}(n)$ is called to compensate for this mismath: its coefficients $\{b_y^{+(k)}, d_y^{+(k)}\}$ are determined together with $\{p_0^{(k)}, p_1^{(k)}\}$ from the 4×2 coordinate closure relations. It is to note that Eq. (58) then becomes exact on the parabolic profile thanks to $\Lambda^{(\frac{\pi}{4},Q5)}(\lambda = \frac{1}{8}) = \frac{1}{8(1-2c_e)}$ [cf. Eq. (50b)]. Recall, $\Lambda = \{\frac{1}{8(1-c_e)}, \frac{1}{8(1-2c_e)}\}$ correspond to $\Lambda = \{\frac{3}{16}, \frac{3}{8}\}$ in the hydrodynamic solutions [26], where the kinematic viscosity $\nu = \frac{1}{3}\Lambda^+$ formally replaces $\mathcal{D}_0 = c_e \Lambda^-$ with $c_e = \frac{1}{3}$. Finally, if $t_c^{(m)} = t_c^{(a)} = \frac{1}{2}$ but $t_c^{(M)} \neq \frac{1}{2}$, the A-layer is additionally built on the four roots (A.8b): it modifies $C(y')$, and hence $\mathcal{D}_T$ in Eq. (30c). A similar situation has been encountered in the interface-perpendicular flow in Appendix A.2.

5.5. The diagonal system with the d2Q9

The A-layer solves Eq. (42) derived in the pure diffusion problem (see Appendix A.3). However, unlike in the pure diffusion, the $-x$ and y axes are not interchangeable [then $\hat{n}_x^{(+,k)} \neq \hat{n}_y^{(+,k)}$], and the interface system is closed with the help of the B-layer coefficients $\{b_y^{+(k)}, d_y^{+(k)}\}$ [Eq. (B.4) with $\hat{B}_x^{+(k)} = -\hat{B}_y^{+(k)}$, $\hat{B}_\perp^{+(k)} = 0$]. The 8×2 coefficients, $\{p_0^{(k)}, p_1^{(k)}\}$, $\{a_j^{(k)}\}$, $j = 1, \ldots, 4\}$ and $\{b_y^{+(k)}, d_y^{+(k)}\}$, are to be derived from the whole system of the 8×2 Eqs. (23)-(24); Eq. (24) becomes replaced by a couple of the 4×2 bounce-back closure relations (9b) in the bounded system. When $\Lambda = \frac{1}{4}$, the A-layer is built with the two roots (43) and the B-layer is fixed with the 4×2 interface-node corrections. Hence, the A-layer and B-layer coexist $\forall \Lambda$ thanks to parallel flow.

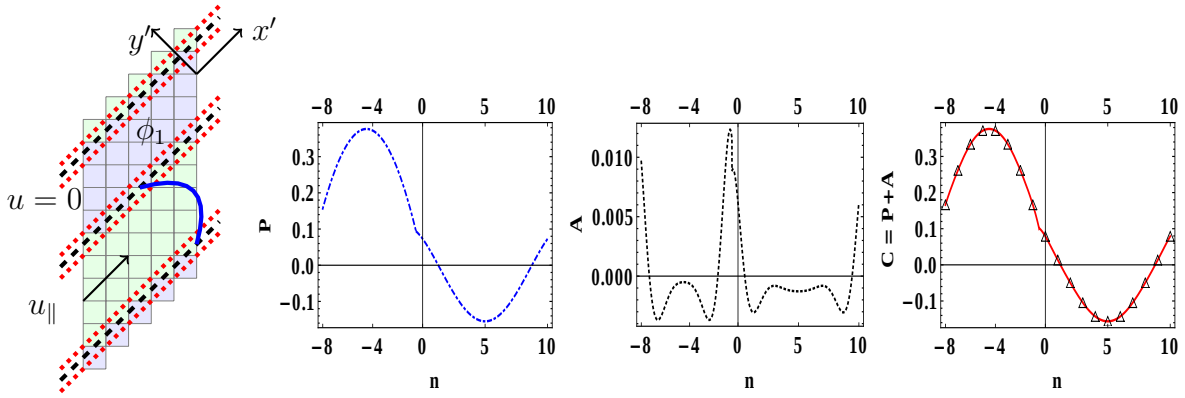

Figure 11: (a) The normalized solution in the diagonal periodic parallel system OPL from Eq. (53): theory (solid) and numerical results (symbols). (b) the polynomial component $P_k(n)$. (c) the A-layer $A_k(n)$. (d) $C_k(n) = P_k(n) + A_k(n)$, $k = \{1, 2\}$. Data: $H = 19$, $r_h = 8/11$, $r_\phi = \frac{1}{4}$, $\Psi = 1.67706 \times 10^{-2}$, $\Lambda^- = 1$, $c_e = 10^{-1}$, $t_c^{(a)} = \frac{1}{4}$, $t_c^{(m)} = \frac{1}{8}$, $t_c^{(M)} = \frac{3}{16}$, $\Lambda = \frac{1}{8}$.

Solution components are illustrated in Figs. 11-13 in OPL system when $t_c^{(m)} = \frac{1}{8}$ and $\Lambda = \frac{1}{8}$. Fig. 11 displays (i) P_k [it is parabolic in the diffusive layer and quartic in the parabolic flow]; (ii) the A-layer $A_k(n)$

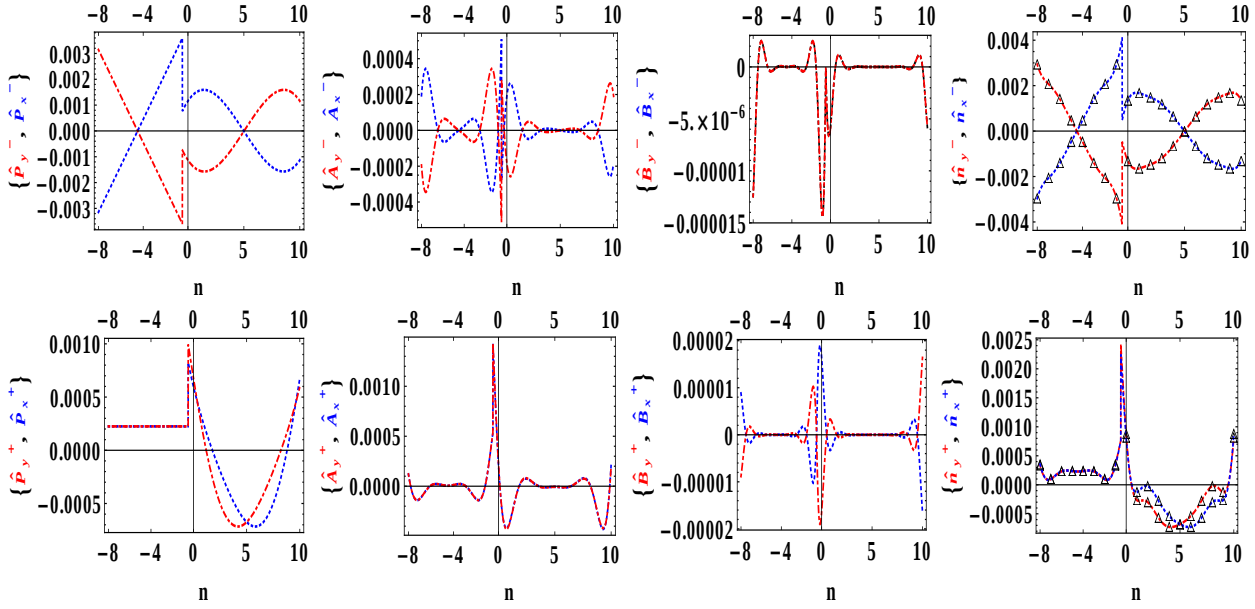

Figure 12: The OPL from Fig. 11. The post-collision is displayed together for $\vec{c}_y$ (dot-dashed (red)) and $\vec{c}_x$ (dashed (blue)): theory (solid) and numerical results (symbols); an additive constant fits the numerical data. Top row: the anti-symmetric component ("-"). Bottom row: the symmetric component ("+"). (a),(e): the polynomials, $\hat{P}_y^{\pm(k)}$ and $\hat{P}_x^{\pm(k)}$; (b),(f): the A-layer, $\hat{A}_y^{\pm(k)}$ and $\hat{A}_x^{\pm(k)}$; (c),(g) the B-layer, $\hat{B}_y^{\pm(k)}$ and $\hat{B}_x^{\pm(k)}$; (d),(h): the sum of three components, $\hat{n}_y^{\pm(k)}$ and $\hat{n}_x^{\pm(k)}$.

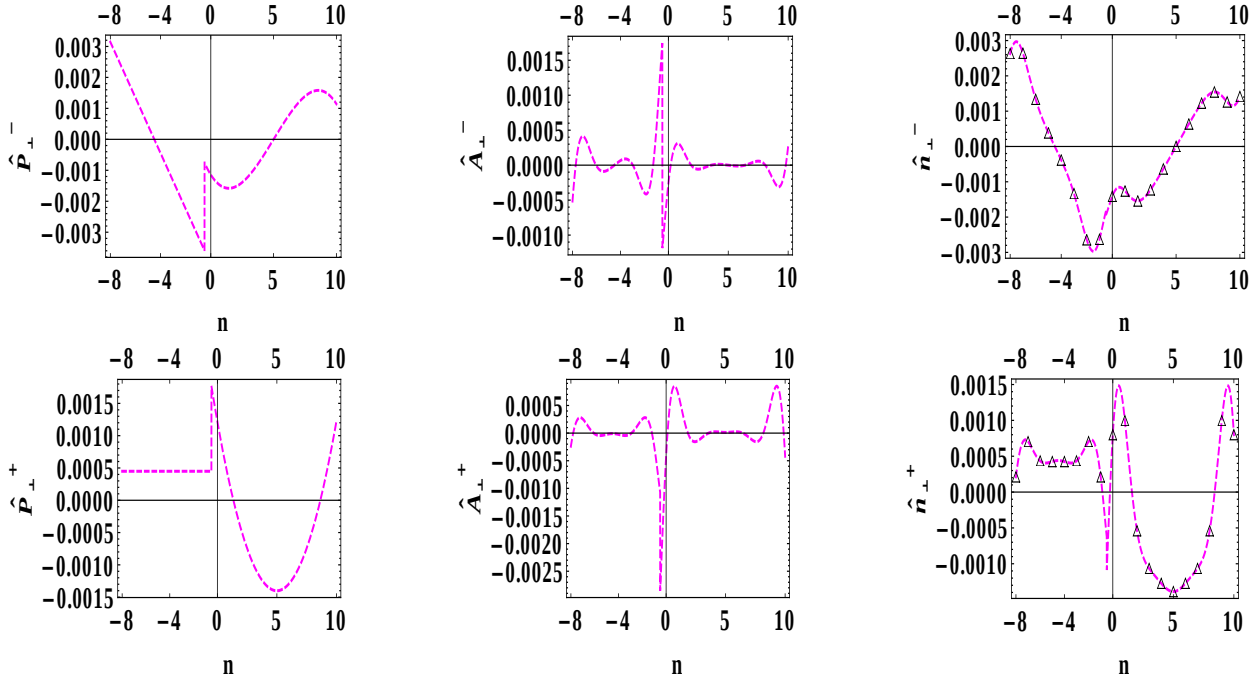

Figure 13: Similar as in Fig. 12 but for $\vec{c}_\perp$: theory (solid) and numerical results (symbol). Top row: the anti-symmetric component ("-"). Bottom row: the symmetric component ("+"). (a),(d): the polynomial component $\hat{P}_\perp^{\pm(k)}$. (b),(e): the A-layer $\hat{A}_\perp^{\pm(k)}$. (c),(f): $\hat{n}_\perp^{\pm(k)} = \hat{P}_\perp^{\pm(k)} + \hat{A}_\perp^{\pm(k)}$. The B-layer vanishes on the diagonal links, $\hat{B}_\perp^{\pm(k)} \equiv 0$.

[r solves Eq. (42): $7+24r+66r^2+24r^3+7r^4=0$]; and (iii), their normalized sum $\mathcal{C}_k(n)$ which coincides with the numerical solution in all grid points. Figs. 12 and 13 display the three post-collision solutions for $\{\vec{c}_x,\vec{c}_y\}$ and for $\vec{c}_\perp$, respectively. In two layers, the piece-wise polynomial $\{\hat{P}_q^{-(k)}\}$ is linear and cubic, $\{\hat{P}_q^{+(k)}\}$ is constant and parabolic. It is noted that the polynomial (physical) and the A-layer post-collision have quite comparable magnitude. The B-layer $\hat{B}_y^{\pm(k)}=\mp\hat{B}_x^{\pm(k)}$ is built with $K^{(k)}|_{\Lambda=\frac{1}{8}}=-3+2\sqrt{2}$ [Eq. (18b)]: it has much smaller amplitude. The sum of these three components coincides with the steady-state output $\hat{n}_q^{\pm}(n)$ in all grid points provided that solution is fixed to its numerical value in one point, because of the post-collision dependency upon an additive constant, Eq. (56b).

5.6. The dispersion coefficients in parallel flow

The truncation and accommodation contributions to dispersion values are examined in Poiseuille flow, stratified constant Darcy flow and the bounded B-OPL system. In theory, $\mathcal{D}_{eff}=\mathcal{D}_0$, however, we quantify the truncation effect in the local gradient, and then $\mathcal{D}_{eff}$. It is confirmed that all $k_T^{(num)}$ contributions scale as Pe^2; the relative error estimates in Eq. (33) are then Pe−independent.

5.6.1. The Poiseuille channel

Consider an open profile $\phi\equiv 1$, $u_{x'}(y')=-\frac{1}{2}\Psi y'(y'-h')$, $y'\in[0,h']$, $h'=H\cos[\theta]$, $k_T=\frac{\mathrm{Pe}^2}{210}$, where $\mathrm{Pe}=\frac{U_{x'}h'}{\mathcal{D}_0}$ is defined with $U_{x'}=h'^{-1}\int_0^{h'}u_{x'}(y')dy'=\frac{\Psi h'^2}{12}$; $U_{x'}$ becomes replaced by $U_{x'}(1+\frac{1}{2}H^{-2})$ in Eq. (4) because of the summation. Plugging then Eqs. (52a)- (53) into Eq. (30c), $k_T^{(p)}$ reads:

$$k_T^{(p)}=k_T^{(0)}-\alpha'\frac{(H^2-1)(H^2-4)\mathrm{Pe}^2}{5H^6}\ ,\ k_T^{(0)}=\frac{\mathrm{Pe}^2}{210}+\frac{(20-21H^2)\mathrm{Pe}^2}{210H^6}\ , \tag{59a}$$

$$\mathrm{d2Q9}\ ,\ \theta=0\ :\ \alpha'=\frac{1}{4}-(1-c_e)\Lambda\ ,\ k_T^{(p)}|_{\Lambda^{(0,Q9)}=\frac{1}{4(1-c_e)}}=k_T^{(0)}\ ; \tag{59b}$$

$$\mathrm{d2Q9}\ ,\ \theta=\frac{\pi}{4}:\alpha'=\frac{3-4t_c^{(m)}}{4}-2\Lambda(2-3t_c^{(m)}-c_e)\ ,\ t_c^{(m)}\neq 0\ ; \tag{59c}$$

$$\mathrm{d2Q5}\ ,\ \theta=\frac{\pi}{4}\ :\ k_T^{(p)}|_{\Lambda^{(\frac{\pi}{4},Q5)}=\frac{1}{4(1-2c_e)}}=k_T^{(0)}\ . \tag{59d}$$

Thanks to symmetry, $k_T^{(p)}$ is independent of the gradient value p_1 [Eq. (52a)] ; hence, Eq. (59) is not sensitive to the effective bounce-back closure [Eq. (9b)]. The $k_T^{(0)}$ replaces k_T when the Taylor Ansatz [65], expressed here by Eqs. (4)-(5), is solved with the discrete Laplacian and integration in Eq. (30c) is performed via summation; $k_T^{(0)}$ converges to k_T as H^{-4} (see [30, 34]). Since there is no A-layer in the straight [d2Q9] and the diagonal [d2Q5] channels, $k_T^{(num)}=k_T^{(p)}$ and it is parametrized by λ with Eq. (50); further, $k_T^{(num)}=k_T^{(0)}$ with Eqs. (55a) and (55b), respectively. Otherwise, the A-layer and B-layer adjust together the bounce-back diagonal closure relation with the polynomial (quartic) solution $C(y')$. The unknowns, $\{p_0,p_1\}$ and the six accommodation coefficients, are defined by the 4×2 bounce-back closure relations to an additive constant p_0. Fig. 14 [second diagram] displays $\mathrm{E}(k_T^{(p)})=k_T^{(p)}/k_T-1$ from Eq. (59c); this result is exact only for d2Q5. The numerical result $\mathrm{E}(k_T)$ is matched exactly when $\mathrm{E}(k_T^{(a)})$ is added in Eq. (33). The last diagram then displays the numerical convergence study of $\mathrm{E}(k_T)$ with the three weight families, $t_c=\{\frac{1}{2},\frac{1}{3},\frac{1}{4}\}$. It is observed that the A-layer produces the most disparate and weight-dependent behaviour on the coarse grid [the sign change explains the non-monotonicity of $|\mathrm{E}(k_T)|$]. However, despite the A-layer, $\mathrm{E}(k_T)$ converges with second-order rate in the diagonal Poiseuille flow due to homogeneity (symmetry). The d2Q5 with $\Lambda=\frac{1}{4}$ is the most accurate as might be expected from Eq. (59d), because $\Lambda^{(\frac{\pi}{4},Q5)}\approx\frac{1}{4}$ when c_e is small.

In resume, the d2Q9 [$\theta=0$] and d2Q5 [$\theta=\frac{\pi}{4}$] produce the expected Taylor result with a fourth-order accuracy employing $\Lambda^{(0,Q9)}$ and $\Lambda^{(\frac{\pi}{4},Q5)}$, respectively. The d2Q9 is impacted by the accommodation corrections in the diagonal channel but $\mathrm{E}(k_T)$ preserves the second-order rate in a homogeneous flow.

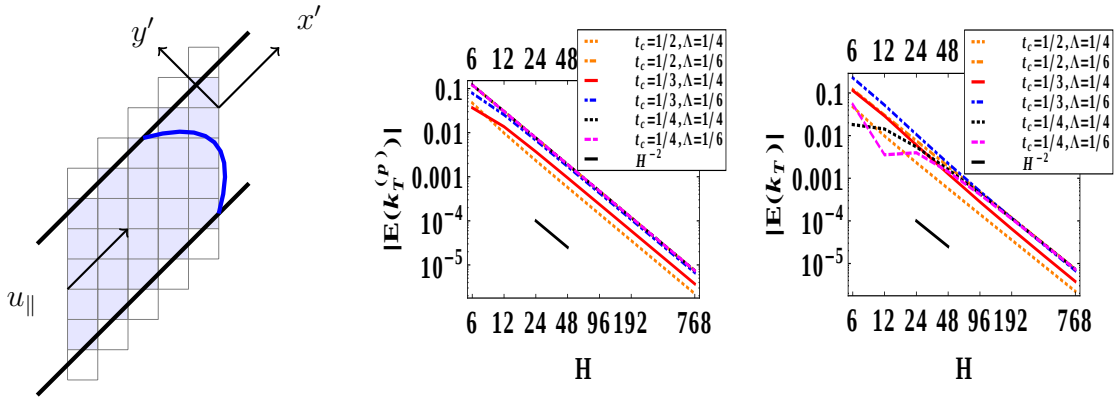

Figure 14: The Taylor dispersion in the diagonal Poiseuille flow is modeled in the single column versus $H = 6 \times 2^m$, $m \in [0, 7]$. (b) the predicted polynomial error component $\mathrm{E}(k_T^{(p)})$, Eq. (59c). (c) the total error $\mathrm{E}(k_T) = \mathrm{E}(k_T^{(p)}) + \mathrm{E}(k_T^{(a)})$ (the predicted and numerical results coincide). (b) and (c): $t_c = \{\frac{1}{2}, \frac{1}{3}, \frac{1}{4}\}$ with $\Lambda = \frac{1}{4}$ (dotted(orange), solid(red), dashed(black)) and $\Lambda = \frac{1}{6}$ (dot-dashed (orange), dot-dashed (blue), dashed (magenta)). The error-estimate is Pe−independent; $c_e = \frac{3}{16}$, $\Psi|_{H=6} = 2.37161 \times 10^{-3}$Eq. (51), Ψ linearly reduces with H. To be compared with Figs. 16 and 17 in heterogeneous channels.

5.6.2. The straight Darcy flow: truncation and B-layer effects in solution gradient

Consider now the Darcy flow $\vec{u} = u_\parallel \vec{1}_{x'}$ in Eq. (51) where $P(y')$ is parabolic and given by Eq. (53a) with $\Psi' = 0$; this solution is invariant by rotation and $\mathcal{E} = 0$ in Eq. (13). The $\mathcal{D}_{eff}$ reduces to $\mathcal{D}_0$ in parallel system; the k_T has exact solution [68, 33]:

$$\Psi = 0 \quad : \; k_T = \frac{\mathrm{Pe}^2 r_h^2 (-1+r_\phi)^2 (r_h+r_\phi)}{12(1+r_h)^4 r_\phi (1+r_h r_\phi)} \; , \; r_h = \frac{h_1'}{h_2'} \; , \; r_\phi = \frac{\phi_1}{\phi_2} \; . \tag{60}$$

In the straight parabolic profile, the relative discrepancy $\mathrm{E}(k_T^{(p)})$ in Eq. (33) is only expected from the interface continuity condition and the summation effect, [34]. However, when $\mathcal{D}_{eff}$ is computed with Eq. (31) at *non-zero velocity*, the measured dispersion value $\mathcal{D}^{(num)}$ sums $\mathrm{E}(k_T^{(p)})$ with $t_d \mathrm{E}^{(p,\nabla)}$ [thanks to truncation in Eq. (56)] and with $t_d \mathrm{E}^{(b)}$ [thanks to B-layer] [we factorize here $t_d k_T$ in the two last estimates], cf. Eq. (32)]:

$$\mathrm{d2Q9} \; , \; \theta = 0 \; : \; k_T^{(num)} = \frac{\mathcal{D}^{(num)}}{\mathcal{D}_0} - 1 = k_T(1 + \mathrm{E}(k_T^{(p)})) + t_d k_T (\mathrm{E}^{(p,\nabla)} + \mathrm{E}^{(b)}) \; , \tag{61a}$$

$$\mathrm{E}(k_T^{(p)}) = -\frac{1 - 12(1-c_e)\Lambda}{H^2} f(r_h, r_\phi) \; , \; f(r_h, r_\phi) = \frac{(1+r_h)^2(1+r_h r_\phi)}{r_h(r_h + r_\phi)} \; , \tag{61b}$$

$$\frac{t_d \mathrm{E}^{(p,\nabla)}}{\mathrm{E}(k_T^{(p)})} = \frac{-8 t_d u_\perp \sum_k \phi_k H_k \Lambda_k^+ p_2^{(k)}}{k_T \mathrm{E}(k_T^{(p)}) c_e < \phi >} = \frac{48 \Lambda t_d}{1 - 12(1-c_e)\Lambda} \; . \tag{61c}$$

Since $\hat{P}_q^-$ is piece-wise linear, $t_d \mathrm{E}^{(p,\nabla)}$ is quantified exactly, it converges with second-order rate and linearly grows with Λ; $\frac{t_d \mathrm{E}^{(p,\nabla)}}{\mathrm{E}(k_T^{(p)})}$ is then $H-$independent and it grows linearly with t_d; the two corrections vanish with d2Q5 [$t_d = 0$]. The B-layer correction $t_d \mathrm{E}^{(b)}$ also scales linearly with t_d and vanishes when $\Lambda = 0$. The two relative contributions, $\mathrm{E}(k_T^{(p)})$ and $t_d(\mathrm{E}^{(p,\nabla)} + \mathrm{E}^{(b)})$ are found exact with the numerical measurements of $k_T^{(num)}$ and $\mathcal{D}_{eff}^{(num)}$, respectively. Fig. 15 illustrates $\mathrm{E}(k_T^{(p)})$, $\mathrm{E}^{(p,\nabla)}$ and $\mathrm{E}^{(b)}$ versus λ when $\Lambda = \Lambda^{(0,Q9)}$ [Eq. (50a)]: $\mathrm{E}(k_T^{(p)})$ and $\mathrm{E}^{(p,\nabla)}$ are linear with λ [or Λ], $\mathrm{E}^{(b)}$ is almost linear with it; the three components have the same order of magnitude. Fig. 15 shows that $\mathrm{E}^{(b)}/\mathrm{E}^{(p,\nabla)}$ is almost $H-$independent, and hence, $\mathrm{E}^{(b)}$ converges with second-order rate. In resume, the truncation and B-layer effects may produce quite comparable, non-zero local gradient values along the translation-invariant direction in the parabolic profile $C(y)$. These two deficiencies of the local gradient converge with second-order rate and they may concern any LBM problem.

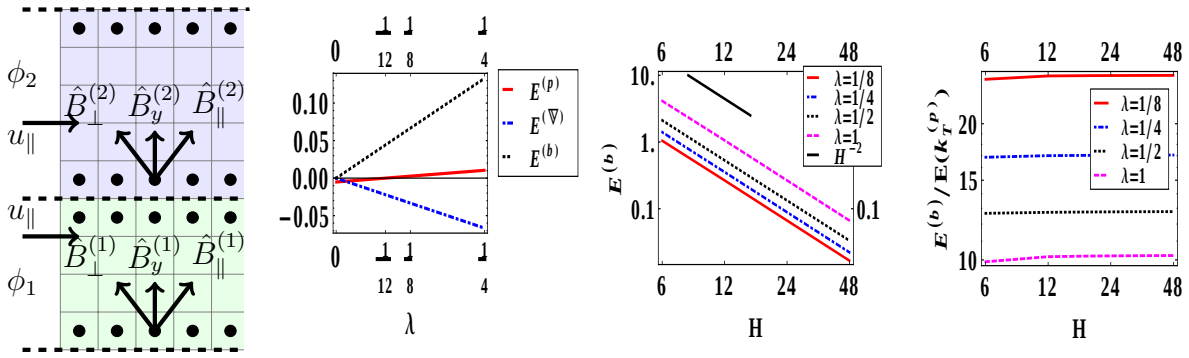

Figure 15: (a) The straight stratified Darcy flow [$c_e = r_\phi/4$, $r_\phi = \frac{1}{4}$, $r_h = 2$, $\Lambda = \lambda/(1-c_e)$]. The three contribution to $\mathrm{E}(k_T)$, Eq. (61): (b) (polynomial) $\mathrm{E}^{(p)}$, (truncation) $\mathrm{E}^{(p,\nabla)}$ and (the B-layer) $\mathrm{E}^{(b)}$ versus λ when $H = 24$; (c) $\mathrm{E}^{(b)}(r_h, r_\phi, c_e, \lambda, H)$; and (d); $\mathrm{E}^{(b)}/\mathrm{E}(k_T^{(p)})$ versus H when $\lambda = \{\frac{1}{8}, \frac{1}{4}, \frac{1}{2}, 1\}$ [solid(red), dot-dashed(blue), dotted (black), dashed (magenta)].

5.6.3. The diagonal Darcy flow: the A-layer solution effect

The d2Q5 is A-layer−free in the diagonal system, the $\mathrm{E}(k_T)$ is then only due to the polynomial component [$f(r_h, r_\phi)$ is defined in Eq. (61b)]:

$$\text{d2Q5}\ ,\ \theta = \frac{\pi}{4}\quad :\ \mathrm{E}(k_T) = \mathrm{E}^{(p)} = -\frac{1-12(1-2c_e)\Lambda}{H^2} f(r_h, r_\phi)\ ,\ \mathrm{E}(k_T) = 0\ \text{ if }\ \Lambda_k = \Lambda^{(\frac{\pi}{4}, Q5)}\ ,\ \lambda = \frac{1}{12}\ . \quad (62)$$

The $\mathrm{E}(k_T)$ converges with second-order rate and produces the same accuracy as the d2Q9 in the straight system with Eq. (50a) and $\lambda = \frac{1}{12}$ [when $\mathrm{E}(k_T^{(p)}) = 0$ in Eq. (61b)]. It is to note that although the mid-grid interface is located exactly with $\lambda = \frac{1}{8}$ in Eq. (58), the summation effect shifts this exact result to $\lambda = \frac{1}{12}$. We examine now the A-layer contribution when $t_c \in]0, \frac{1}{2}[$ and $\Lambda = \frac{1}{4}$.

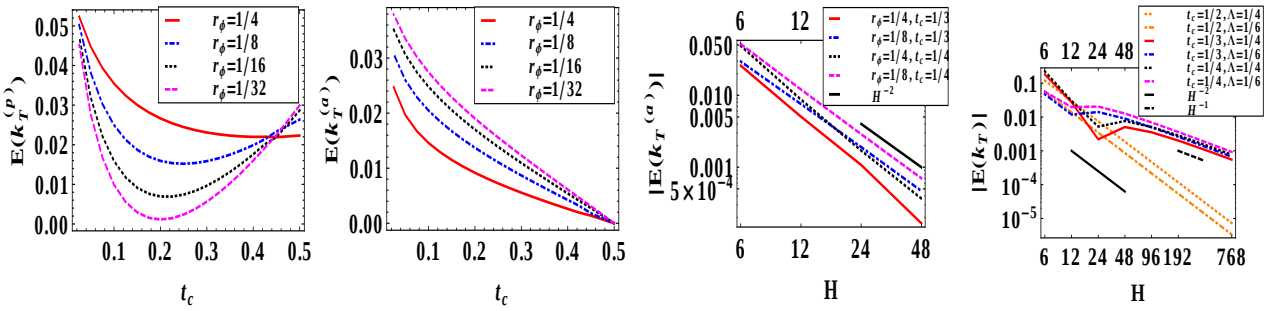

Figure 16: The diagonal stratified Darcy flow. (a) the polynomial [$\mathrm{E}(k_T^{(p)}) = \frac{k_T^{(p)}}{k_T} - 1$] and (b) the A-layer [$\mathrm{E}(k_T^{(a)}) = \frac{k_T^{(a)}}{k_T}$] contributions versus t_c; (c): $\mathrm{E}(k_T^{(a)})$ versus H, $\Lambda = \frac{1}{4}$, $t_c = \{\frac{1}{3}, \frac{1}{4}\}$; (d): the total error-estimate $|\mathrm{E}(k_T)| = |\mathrm{E}(k_T^{(p)}) + \mathrm{E}(k_T^{(a)})|$ when $t_c = \{\frac{1}{2}, \frac{1}{3}, \frac{1}{4}\}$ with $\Lambda = \frac{1}{4}$ [dotted(orange), solid(red), dashed(magenta)] and $\Lambda = \frac{1}{6}$ [dot-dashed (orange), dot-dashed(blue), dotted (black)]. The $\mathrm{E}(k_T)$ converges with H^{-2} rate only with d2Q5 [$t_c = \frac{1}{2}$] where the A-layer vanishes and $\mathrm{E}(k_T) = \mathrm{E}(k_T^{(p)})$. Data (a)-(b): $\Lambda = \frac{1}{4}$, $c_e = r_\phi/4$, $r_h = \frac{8}{11}$, $H = 19$. Data (c)-(d): $r_h = 2$, $c_e = \frac{1}{16}$, $H = 6 \times 2^n$, $n \in [0, 7]$.

Fig. 16 displays $\mathrm{E}(k_T^{(p)})$ and $\mathrm{E}(k_T^{(a)})$ in Eq. (33). It is observed that $\mathrm{E}(k_T^{(p)})$ is not monotonous with t_c, but $\mathrm{E}(k_T^{(a)})$ increases monotonously when $t_c \to 0$ from $\mathrm{E}(k_T^{(a)})|_{t_c=\frac{1}{2}} = 0$; $\mathrm{E}(k_T^{(p)})$ and $\mathrm{E}(k_T^{(a)})$ have the same sign and order of magnitude. Fig. 16 [third diagram] indicates that $\mathrm{E}(k_T^{(a)})$ reduces with second-order rate, on the coarse grid at least. However, the last diagram in Fig. 16 shows that the total deviation $\mathrm{E}(k_T) = \mathrm{E}(k_T^{(p)}) + \mathrm{E}(k_T^{(a)})$ asymptotically converges only with first-order rate, as H^{-1}. It is highlighted that this first-order effect is due to $\mathrm{E}(k_T^{(p)})$, because the A-layer modifies the parabolic profile. Asymptotically, the d2Q5 is then much more accurate than the d2Q9. As might be expected, and similar to the interface-

perpendicular Darcy flow, the d2Q9 with the larger weight $t_c = \frac{1}{3}$ and the smaller value $\Lambda = \frac{1}{6}$ is most accurate among the four examined configurations.

5.6.4. The bounded stratified parabolic flow: the A-layer solution effect

The B-OPL system is described by Eq. (51) and it is closed by the solid walls. The transport coefficients are weight-independent in the straight layers, their TRT solution for k_T, Sk and Ku is displayed in Sec.6.2 [34] using $\Lambda^{(0,Q9)} = \frac{1}{4(1-c_e)}$. We provide the exact solution $k_T(r_\phi, r_h)$ and the second-order error-estimate $\mathrm{E}(k_T^{(p)})$ using parametrization dependency $\Lambda^{(0,Q9)}$ from Eq. (50a):

$$k_T(r_\phi, r_h) = \frac{\mathrm{Pe}^2(1+cX)}{210a(1+cR_\phi)}\ ,\ X = 9 + 78c + r_h^2\ ,\ a = 1+c\ ,\ c = r_h r_\phi\ ,\ R_\phi = r_\phi^{-1}\ ; \tag{63a}$$

$$\theta = 0\ ,\ \text{d2Q9}\ :\ \mathrm{E}(k_T^{(p)}) = H^{-2}\mathrm{E}^{(p,2)} + O(H^{-4}) + O(H^{-6})\ ,$$

$$\mathrm{E}^{(p,2)}(r_\phi, r_h, \lambda) = \frac{7(1+r_h)^2(-3+12a\lambda(1+6c)+c(-20+c(3+20cR_\phi^2)))}{2(1+cX)}\ , \tag{63b}$$

$$\mathrm{E}(k_T^{(p)})|_{\theta=0} = \mathrm{E}(k_T^{(p)})|_{\theta=\frac{\pi}{4}}\ \text{ if }\ \Lambda|_{\theta=0} = \Lambda^{(0,Q9)}\ \text{ and }\ \Lambda|_{\theta=\frac{\pi}{4}} = \Lambda^{(\frac{\pi}{4},Q5)}\ ,\ \text{with}\ \ \lambda = \frac{1}{6}\ . \tag{63c}$$

When $r_h \to 0$, the B-OPL reduces to the Poiseuille channel, then $\mathrm{E}^{(p,2)}(\lambda) = \frac{21(-1+4\lambda)}{2}$ corresponds to the second-order term in Eq. (59a) with Eq. (59b). The two systems, d2Q9 [$\theta = 0$] and d2Q5 [$\theta = \frac{\pi}{4}$], converge with second-order rate; they have the same accuracy only when $\lambda = \frac{1}{6}$ [Eq. (63c)]. Otherwise, the A-layer impacts solution in the diagonal system. Fig. 17 displays the relative polynomial [$\mathrm{E}(k_T^{(p)})$] and the A-layer

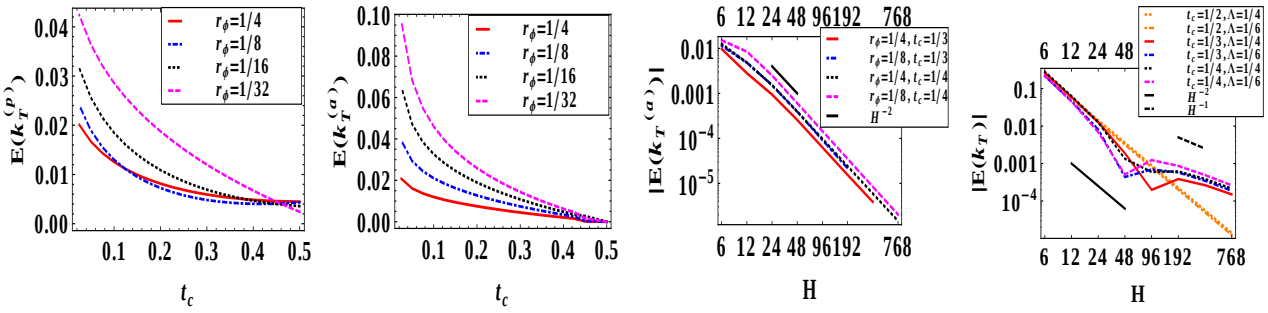

Figure 17: The diagonal bounded open-porous system B-OPL, following Fig. 16.

[$\mathrm{E}(k_T^{(a)})$] contributions to Eq. (33) in the diagonal system when $\Lambda = \frac{1}{4}$; both of them grow monotonously when $t_c \to 0$; $\mathrm{E}(k_T^{(a)})$ behaves very similar to the Darcy flow in Fig 16, and $|\mathrm{E}(k_T^{(a)})|$ even exceeds $|\mathrm{E}(k_T^{(p)})|$. It is then shown that $|\mathrm{E}(k_T^{(a)})|$ monotonously reduces with second-order rate when $t_c = \{\frac{1}{3}, \frac{1}{4}\}$. Nevertheless, the last diagram confirms that the total result $\mathrm{E}(k_T)$ asymptotically converges only with first-order rate due to the the polynomial component $\mathrm{E}(k_T^{(p)})$, as with the Darcy flow in Fig. 16. In summary, the interface accommodation modifies the polynomial solution and slows the k_T convergence to first order on a diagonal mid-grid interface, with the d2Q5 exception.

5.7. Resume

When the stratified layers and interface-parallel flow are aligned with the *coordinate axis*, the B-layer accommodates the d2Q9 solution on the interface (boundary), and it vanishes in d2Q5. The B-layer does not impact the modeled Taylor dispersion coefficient k_T in Eq. (30c) and k_T remains weight-independent. The scalar field and the k_T are properly controlled by Pe when $\Lambda = \frac{\lambda}{1-c_e}$. However, when one computes $\mathcal{D}_{eff}$ in Eq. (30b) from the local gradient *in interface-parallel velocity field*, then the truncation and the

B-layer affect $\mathcal{D}_{eff}$ in proportion to the diagonal weight value, Eq. (61). Moreover, although the scalar solution of the given boundary-value problem is determined to an additive constant, the locally derived gradient becomes constant-dependent in the parabolic velocity profile. Finally, $\mathcal{D}_{eff}$ then depends on c_e at fixed $\mathcal{D}_0$. In the diagonal channels, the d2Q5$^{(r)}$ remains unsuitable because of the "checkerboard" effect.

Otherwise, the polynomial solution becomes assisted by the B-layer even in d2Q5, because the interface-parallel flow breaks the symmetry between the two coordinate axes. The d2Q9 with any weights, except for d2Q5 and d2Q5$^{(r)}$, needs both the A-layer and the B-layer; the A-layer is built on the four diffusion roots to Eq. (40b); the accommodation coefficients solve the whole system of the interface and boundary conditions, Eqs. (23)-(24). The accommodation maintains the k_T scaling with Pe^2 and the relative error-estimate is then $\mathrm{Pe}-$independent [at fixed c_e]; however, the gradient of the polynomial solution component gets modified. In the homogeneous (open) diagonal channel, the parabolic mass-source and velocity field activate the two accommodations but, thanks to symmetry, k_T converges with second-order rate to its famous Taylor value. The d2Q9 [$\theta = 0$] and d2Q5 [$\theta = \frac{\pi}{4}$] converge k_T with the fourth-order rate using, respectively, $\Lambda = \frac{1}{4(1-c_e)}$ and $\Lambda = \frac{1}{4(1-2c_e)}$, Eq. (59). In the heterogeneous channels, only d2Q5 maintains the second-order rate relatively the mid-grid interface. The d2Q9 converges k_T with first-order asymptotic rate, either on the parabolic or quartic solutions.

6. Concluding remarks

This work presents a novel piece of the linear algebra behind the exact construction of the steady-state scalar-field and non-equilibrium solutions of Lattice Boltzmann schemes. The advection-diffusion d2Q9 TRT model is operated on its full parameter space; it is composed of the two relaxation parameters $\Lambda^{\pm}$ per phase, the diffusion-coefficient scale c_e and the three equilibrium weight-families for (i) diffusion, (ii) advection and (iii) mass-source. All solution components are decomposed into their polynomial and discrete-exponential counterparts; the equilibrium and non-equilibrium are exactly inter-related with the TRT recurrence equations, subject to local mass-conservation solvability constraint. The whole solution is fixed with the exact intrinsic closure relations of the implicit-interface and bounce-back boundary, assumed to be located mid-grid in the straight and diagonal two-layered configurations. When the advection-diffusion process is perpendicular to the interface, the constant flux jump produces a non-zero solution in the fully periodic heterogeneous system.

	Straight						Diagonal					
	$\vec{u}=0$		$\vec{u}=u_{\perp}\vec{1}_{y'}$		$\vec{u}=u_{\parallel}\vec{1}_{x'}$		$\vec{u}=0$		$\vec{u}=u_{\perp}\vec{1}_{y'}$		$\vec{u}=u_{\parallel}\vec{1}_{x'}$	
	$Q5$	$Q9$	$Q5$	$Q9$	$Q5$	$Q9$	$Q5$	$Q9$	$Q5$	$Q9$	$Q5$	$Q9$
A-layer	$-$	$-$	$-$	$-$	$-$	$-$	$-$	$+$	$-$	$+$	$-$	$+$
B-layer	$-$	$-$	$-$	$t_q^{(a)} \neq t_q^{(m)}$	$-$	$+$	$-$	$\Lambda=\frac{1}{4}$	$-$	$+$	$+$	$+$

Table 1: This table summarises the presence (+) or absence (-) of the A-layer in equilibrium [$A(y')$ from Eq. (15)], and the B-layer in post-collision [$\hat{B}_q^{\pm}(n)$ from Eq. (18b)], with the d2Q5 ["$Q5$"] and an arbitrary advection-diffusion d2Q9 stencil ["$Q9$", $\forall\ \{t_q^{(m)}, t_q^{(a)}\}$, $t_q^{(M)} = t_q^{(m)}$]. The three corresponding piece-wise scalar-field solutions $C(y')$ are (a) linear [$\vec{u}=0$, $M=0$]; (b) discrete-exponential [$\vec{u}=u_{\perp}\vec{1}_{y'}$, $M(y')$ is piece-wise constant]; and (c), polynomial [$\vec{u}=u_{\parallel}(y')\vec{1}_{x'}$, $M(y')$ is piece-wise polynomial]. The d2Q5$^{(r)}$ does not need either A-layer or B-layer in the diagonal orientation; however, its scalar field solution is unsuitably shifted on the two sub-diagonals.

Is is demonstrated that these simplest mass-conserving closure conditions may excite an exponential accommodation of the scalar field, referred to as the A-layer. The A-layer covers for the weight-depending mismatch between the bulk solution across the interface; its base depends upon the weights, free-tunable collision parameter $\Lambda = \Lambda^{-}\Lambda^{+}$, and the physical governing numbers. The complementary, additive, B-layer directional post-collision correction solves the recurrence equations for zero equilibrium, and its base is fixed by Λ alone. The B-layer is singular when $\Lambda = \frac{1}{4}$, and it is then constrained to the interface and boundary nodes. The considered physical problems constitute three groups of increasing complexity, ranging from the

one dimensional pure diffusion and interface-perpendicular flow to the two-dimensional, constant and piece-wise parabolic, interface-parallel flow problems. Table 1 summarizes their accommodation counterparts. In resume, the B-layer does not modify the scalar field and its scalar solution is weight-independent for a straight d2Q9 system; however, the B-layer may bring the linear weight-dependency into the *locally* derived solution gradient. The A-layer renders the macroscopic scalar field depending on the weights and the diffusion-scale c_e in the diagonal d2Q9 system. Furthermore, the A-layer degrades the local gradient of the piece-wise linear profile, which is the most classical first-order Chapman-Enskog prediction [20, 11].

On top of the accommodation effects, the local gradient-estimate may become inconsistent in the translation-invariant direction due to the truncation of the type $\partial_x C(y) \approx c_e^{-1}\partial_y^2[u_\parallel(y)C(y)]\sum_{q=1}^{Q_m} t_q^{(a)} c_{qx}^2 c_{qy}^2$ when $\vec{u} = u_\parallel(y)\vec{1}_x$: $\partial_x C(y)$ differs from zero even on the parabolic $C(y)$ profile in constant flow, and it depends on an additive constant in the parabolic profile $\partial_y^2 u_\parallel(y) \neq 0$. The truncation and accommodation contributions may reach quite comparable amplitudes. In contrast with the truncation, the accommodation is beyond the reach of the perturbative analysis, but it explains the first-order solution and its gradient convergence delay in the grid-rotated geometry. In this regard, we note that the A-layer and B-layer are not the Knudsen layers in the kinetic sense [64], where they should appear only in extension of the hydromechanical models to account for the "higher-order effects in the Knudsen number".

The explicit interface (boundary) treatment, accurate with respect to the physical continuity relations, is expected to damp the spurious accommodations in any grid-rotated geometry [23]. The d2Q4 *interface-conjugate*, decomposition-flux scheme [48, 49] is found accurate [15] on the diagonal interface. However, the local gradient rate degrades on the circular (spherical) surface with the full-weight interface-conjugate, from -1.5 [d2Q5] towards -0.5 [d2Q9], [51]. It might be suggested that the full-weight scheme does not attenuate sufficiently the accommodation layers due to the nonphysical tangential diffusive-flux constraint. A poor accuracy because of an implicit, straight interface tangential-coupling has been also encountered with the discontinuous anisotropic weights, and improved for their leading-order mismatch [25]. Our recent work [35] confirms that the second-order interface-conjugate extension of this last approach vanishes the exponential accommodations of the arbitrary-placed rotated interface in the parabolic profiles. It would be interesting to examine and extend from this perspective the known interface, boundary and grid-refining approaches. All in all, we hope our approach to become helpful for the understanding of the LBM steady-state and transient accommodations, and for their distinction from the LBM kinetic behaviour.

Appendix A. The A-layer accommodation

The solution procedure from Sec. 3.2 is applied in the pure diffusion, interface-perpendicular and interface-parallel flow. We make use the solution invariance along $\vec{c}_x$ [$\theta = 0$] and $\vec{c}_\parallel$ [$\theta = \frac{\pi}{4}$]; Eqs. (26) and (27) are then expressed with the exact central-differences:

$$\bar{\Delta}_q\psi(n) = \frac{1}{2}(\psi(n+\delta_q) - \psi(n-\delta_q)) \ , \tag{A.1a}$$

$$\bar{\Delta}_q^2\psi(n) = \psi(n+\delta_q) - 2\psi(n) + \psi(n-\delta_q) \ , \ \forall\ \psi = \{\psi_k\} \ , \tag{A.1b}$$

$$\bar{\Delta}_q r^n = \frac{1}{2} r^{(n-\delta_q)}(-1 + r^{2\delta_q}) \ , \ \bar{\Delta}_q^2 r^n = r^{(n-\delta_q)}(-1 + r^{\delta_q})^2 \ , \tag{A.1c}$$

with

$$\theta = 0: \ \delta_q = \{1,1,1\} \quad \text{for} \quad \vec{c}_q = \{\vec{c}_y, \vec{c}_\parallel, \vec{c}_\perp\} \ , \tag{A.2a}$$

$$\theta = \frac{\pi}{4}: \ \delta_q = \{-1,1,2\} \ \text{ for } \ \vec{c}_q = \{\vec{c}_x, \vec{c}_y, \vec{c}_\perp\} \ . \tag{A.2b}$$

Appendix A.1. Pure diffusion through the diagonal layers

Solution is looked for in the form of Eqs. (40)-(41). The A-layer solves Eq. (26) with $\vec{u} = 0$ and hence, $e_q^{-(a)} \equiv 0$ [phase-index k is dropped]:

$$\hat{a}_{q,j} r_j^n \ = \ -\Lambda^- c_e t_q^{(m)} a_j \bar{\Delta}_q^2 r_j^n + (\Lambda - \frac{1}{4})\hat{a}_{q,j}\bar{\Delta}_q^2 r_j^n \ , \ q = 1, \ldots, \frac{Q_m}{2} \ , \ j = 1, 2, \ldots \ . \tag{A.3}$$

When $t_c^{(m)} \neq 0$, Eq. (A.3) is expressed with Eq. (A.1) and solved for $\hat{a}_{x,j}(a_j)$ [$\vec{c}_q = \vec{c}_x$, $\delta_q = -1$] and $\hat{a}_{y,j}(a_j)$ [$\vec{c}_q = \vec{c}_y$, $\delta_q = 1$]; the diagonal component $\hat{a}_{\perp,j}$ is expressed from Eq. (28a):

$$t_c^{(m)} \neq 0 \ : \ \hat{a}_{x,j} = \hat{a}_{y,j} = \hat{a}_j^{(u=0)}(a_j, t_c^{(m)}) \ , \ \text{ with } \ \hat{a}_j^{(u=0)}(a_j, t_q) = -\frac{a_j \Lambda^- c_e t_q (-1+r_j)^2}{r_j - (\Lambda - \frac{1}{4})(-1+r_j)^2} \ , \tag{A.4a}$$

$$\hat{a}_{\perp,j} = -(\hat{a}_{x,j} + \hat{a}_{y,j}) \quad \text{for } \ \vec{c}_q = \vec{c}_\perp \ . \tag{A.4b}$$

When $t_d^{(m)} \neq 0$, solution of Eq. (A.3) for $\vec{c}_q = \vec{c}_\perp$ reads:

$$t_d^{(m)} \neq 0 \ : \ \hat{a}_{\perp,j} = \hat{a}_{\perp,j}^{(u=0)}(a_j, t_d^{(m)}) \ \text{ with } \ \hat{a}_{\perp,j}^{(u=0)}(a_j, t_q) = \frac{4 a_j t_q c_e \Lambda^- (-1+r_j^2)^2}{4\Lambda(-1+r_j^2)^2 - (1+r_j^2)^2} \ , \tag{A.5a}$$

$$\hat{a}_{x,j} = \hat{a}_{y,j} = -\frac{1}{2}\hat{a}_{\perp,j}^{(u=0)} \ . \tag{A.5b}$$

Equating Eqs. (A.4a) and (A.5b), or Eqs. (A.5a) and (A.4b), one gets the solvability condition in the form of the quartic equation given by Eq. (42) with the roots $r = \cup_{j=1}^4 \{r_j^{(k)}(t_q^{(m)}, \Lambda)\}$. These roots are illustrated in Fig. 3. The auxiliary functions to Eq. (42) are:

$$\Delta_0 = c^2 - 3bd + 12ae \ , \ \Delta_1 = 2c^3 - 9bcd + 27b^2 e + 27ad^2 - 72ace \ , \tag{A.6a}$$

$$\Delta = -\frac{1}{27}(\Delta_1^2 - 4\Delta_0^3) = 8388608 t_c^{(m)} (t_c^{(m)} - 2(\Lambda - t_c^{(m)} + 6\Lambda t_c^{(m)})^2)^2 \ , \tag{A.6b}$$

$$P = 8ac - 3b^2 = 128(4t_c^{(m)} - \Lambda(1+6t_c^{(m)})(1 - 2t_c^{(m)} + 2\Lambda(1+6t_c^{(m)}))) \ , \tag{A.6c}$$

$$\begin{aligned} D &= 64a^3 e - 16a^2 c^2 + 16ab^2 c - 16a^2 bd - 3b^4 \\ &= -2048(1 - 4t_c^{(m)}(7 + 3t_c^{(m)}) + 8\Lambda(1+2t_c^{(m)})(1+6t_c^{(m)})) \times (-t_c^{(m)} + 2(\Lambda - t_c^{(m)} + 6\Lambda t_c^{(m)})^2) \ . \end{aligned} \tag{A.6d}$$

One interesting case is $\Lambda = \frac{1}{6}$, $t_c^{(m)} = \frac{1}{18}$, then $\Delta = 0$ in Eq. (A.6b), and Eq. (42) reduces to $-\frac{4}{9}(1 + r(4 + r))^2 = 0$, with the two double roots $r_{1,2} = r_{3,4} = -2 \pm \sqrt{3}$. Otherwise, Eq. (A.6) allows to examine the roots. When $\Delta > 0, P < 0, D < 0$, the four roots are all real [69]. These conditions are all satisfied when

$$\begin{aligned} &(\Lambda > \frac{1}{4} \ , \ \forall \, t_c^{(m)}) \ \ || \ \ (\Lambda = \frac{1}{6} \ , \ t_c^{(m)} \in]0, \frac{1}{18}[) \ \ || \ \ (t_c^{(m)} \in]0, t_c^{max}(\Lambda)] \ , \ \forall \, \Lambda \neq \frac{1}{6} \ ) \ , \\ &t_c^{max}(\Lambda)] = \frac{1 + 4\Lambda(1-6\Lambda) - \sqrt{1 + 8\Lambda(1-6\Lambda)}}{4(1-6\Lambda)^2} \ , \ \Delta(t_c^{max}) = 0 \ . \end{aligned} \tag{A.7}$$

We note that all four roots are real with any weights when $\Lambda > \frac{1}{4}$. The d2Q5 holds four non-trivial roots:

$$t_c^{(m)} = \frac{1}{2} \ , \ \Lambda \neq \frac{1}{4} : \ 4\Lambda(-1+r^2)^2 - (1+r^2)^2 = 0 \ , \tag{A.8a}$$

$$\cup_{j=1}^4 r_j = r|_{\text{d2Q5}}^{(u=0)} = \pm\sqrt{\frac{2\sqrt{\Lambda} - \sigma}{2\sqrt{\Lambda} + \sigma}} \ , \ \sigma = \pm 1 \ . \tag{A.8b}$$

The d2Q5$^{(r)}$ has only two non-trivial roots:

$$t_c^{(m)} = 0 \ , \ \Lambda \neq \frac{1}{4} : \ 4\Lambda(-1+r)^2 - (1+r)^2 = 0 \ , \ r_{3,4} = -1 \ , \tag{A.9a}$$

$$\{r_1, r_2\} = r|_{\text{d2Q5}^{(r)}}^{(u=0)} = \frac{1 \pm 4\sqrt{\Lambda} + 4\Lambda}{4\Lambda - 1} = \{K_{(\sigma)} \ , \ \sigma = \pm 1\} \ . \tag{A.9b}$$

The two roots $r|_{\text{d2Q5}^{(r)}}^{(u=0)}$ are equivalent to B-layer roots (18b).

Appendix A.2. The interface-perpendicular Darcy flow $\vec{u} = u_\perp \vec{1}_{y'}$

The exponential components reads with: $e_q^{+(a)} = t_q^{(m)} c_e \sum_{j=1} a_j {r_j}^{n_k}$, $e_q^{-(a)} = t_q^{(a)} u_\perp c_{q,y'} \sum_{j=1} a_j {r_j}^{n_k}$. Eq. (26) then reads as [$r_j = r_j^{(k)}$, k is dropped]:

$$\hat{a}_{q,j} r_j^n = u_\perp c_{q,y'} t_q^{(a)} a_j \bar{\Delta}_q r_j^n - \Lambda^- c_e t_q^{(m)} a_j \bar{\Delta}_q^2 r_j^n + (\Lambda - \frac{1}{4}) \hat{a}_{q,j} \bar{\Delta}_q^2 r_j^n \ , \ \forall\, q = 1, .., \frac{Q_m}{2} \ , \ j = 1, 2, . \quad \text{(A.10)}$$

Eq. (A.10) reduces to Eq. (A.3) when $u_\perp = 0$. We first solve Eq. (A.10) for the coordinate links:

$$\theta = 0 : \ \hat{a}_{y,j} = \hat{a}_j^{(u=0)}(a_j, t_c^{(m)}) + \frac{1}{2} \hat{a}_j^{(u)}(a_j, t_c^{(a)}) \ , \quad \text{(A.11a)}$$

$$\hat{a}_{\perp,j} = \hat{a}_{\parallel,j} = -\frac{1}{2} \hat{a}_{y,j} \ , \ \hat{a}_{x,j} = 0 \ ; \quad \text{(A.11b)}$$

$$\theta = \frac{\pi}{4} : \ \hat{a}_{x,j} = \hat{a}_{y,j} = \hat{a}_j^{(u=0)}(a_j, t_c^{(m)}) + \frac{\sqrt{2}}{4} \hat{a}_j^{(u)}(a_j, t_c^{(a)}) \ , \quad \text{(A.11c)}$$

$$\hat{a}_{\perp,j} = -(\hat{a}_{x,j} + \hat{a}_{y,j}) \ , \ \hat{a}_{\parallel,j} = 0 \ ; \quad \text{(A.11d)}$$

$$\theta = \{0, \frac{\pi}{4}\} \ : \ \hat{a}_j^{(u)}(a_j, t_q) = \frac{a_j t_q u_\perp (-1 + {r_j}^2)}{r_j - (\Lambda - \frac{1}{4})(-1 + r_j)^2} \ . \quad \text{(A.11e)}$$

Eq. (A.4) gives $\hat{a}_j^{(u=0)}(a_j, t_q)$. Eq. (A.10) is now solved for the diagonal links:

$$\theta = 0 : \hat{a}_{\parallel,j} = \hat{a}_{\perp,j} = \hat{a}_j^{(u=0)}(a_j, t_d^{(m)}) + \frac{1}{2} \hat{a}_j^{(u)}(a_j, t_d^{(a)}) \ , \quad \text{(A.12a)}$$

$$\hat{a}_{y,j} = -(\hat{a}_{\parallel,j} + \hat{a}_{\perp,j}) \ ; \quad \text{(A.12b)}$$

$$\theta = \frac{\pi}{4} : \hat{a}_{\perp,j} = \hat{a}_{\perp,j}^{(u=0)}(a_j, t_d^{(m)}) + \frac{\sqrt{2}}{4} \hat{a}_{\perp,j}^{(u)}(a_j, t_d^{(a)}) \ , \quad \text{(A.12c)}$$

$$\hat{a}_{x,j} = \hat{a}_{y,j} = -\frac{1}{2} \hat{a}_{\perp,j} \ ; \quad \text{(A.12d)}$$

$$\theta = \{0, \frac{\pi}{4}\} \ : \ \hat{a}_{\perp,j}^{(u)}(a_j, t_q) = -\frac{t_q a_j u_\perp (-1 + {r_j}^4)}{4\Lambda(-1 + r_j^2)^2 - (1 + r_j^2)^2} \ . \quad \text{(A.12e)}$$

Eq. (A.5a) gives $\hat{a}_{\perp,j}^{(u=0)}(a_j, t_q)$. The obtained solution for the coordinate links from Eq. (A.11), and the diagonal links from Eq. (A.12), is summed and equated to zero in Eq. (28a). In the straight layers, $\hat{a}_j^{(u=0)}$ and $\hat{a}_j^{(u)}$ from Eqs. (A.11a) and (A.12a) scale with $t_q^{(m)}$ and $t_q^{(a)}$, respectively. The solvability condition $\hat{a}_{y,j} + \hat{a}_{\parallel,j} + \hat{a}_{\perp,j} = 0$ is then weight-independent due to Eq. (2d), it is quadratic and given in Eq. (44). In the diagonal system, the solvability condition $\hat{a}_{x,j} + \hat{a}_{y,j} + \hat{a}_{\perp,j} = 0$ is expressed by the sextic ($\Lambda \neq \frac{1}{4}$) and the quartic ($\Lambda = \frac{1}{4}$) equations with one root equal to 1. The reduced quintic and cubic equations, respectively, are given in Eqs. (A.13) and (A.14):

$$\Lambda \neq \frac{1}{4} \quad , \quad \forall\, t_q^{(a)}, t_q^{(m)} \ : \sum_{j=0}^{5} b_j r^j = 0 \ , \ \text{with}$$

$$\begin{aligned}
b_0 &= -\eta_1 (P_3 + 2\zeta_1) \ , \ b_1 = 4\Lambda_k (P_4 + 2\zeta_1) + P_5 + 6 - 28 t_c^{(m)} \ , \ b_2 = 4(P_2 + \eta_2 \zeta_1) \ , \\
b_5 &= -\eta_1 (P_3 - 2\zeta_1) \ , \ b_4 = 4\Lambda_k (P_4 - 2\zeta_1) + P_5 - 6 + 28 t_c^{(m)} \ , \ b_3 = 4(P_2 - \eta_2 \zeta_1) \ , \\
\eta_1 &= 4\Lambda_k - 1 \ , \ \eta_2 = 4\Lambda_k + 1 \ , \ P_i = \sqrt{2} P e_\perp^{(k)} \zeta_i \ , \ i = 2, \ldots, 6 \ , \ P e_\perp^{(k)} = \frac{u_\perp}{\mathcal{D}_k} \ , \\
\zeta_1 &= 1 + 6 t_c^{(m)} \ , \ \zeta_2 = 1 + 8\Lambda_k t_c^{(a)} \ , \ \zeta_3 = 1 + 2 t_c^{(a)} \ , \\
\zeta_4 &= 1 - 6 t_c^{(a)} \ , \ \zeta_5 = 3 - 2 t_c^{(a)} \ , \quad \zeta_6 = -1 + 2 t_c^{(a)} .
\end{aligned} \quad \text{(A.13)}$$

When $\Lambda=\frac{1}{4}$, Eq. (12) reduces to cubic equation [in notations of Eq. (A.13)]:

$$\Lambda_k=\frac{1}{4}\ ,\ \forall\ t_q^{(a)}\ ,\forall\ t_q^{(m)}\ :\ ar^3+br^2+cr+d=0\ ,\ \text{ with}$$
$$d=-2+4t_c^{(m)}+P_6\ ,\ c=-2\zeta_1-P_3\ ,\ b=2\zeta_1-P_3\ ,\ a=2-4t_c^{(m)}+P_6\ . \tag{A.14a}$$
$$Q(\mathrm{Pe},t_c)|_{t_c^{(a)}=t_c^{(m)}=t_c}=128t_c^{(a)}+{Pe_\perp^{(k)}}^2(2+{Pe_\perp^{(k)}}^2(-1+4t_c)^3+8t_c(-11+13t_c))\ . \tag{A.14b}$$

Eq. (A.14b) is proportional to determinant [44] of Eq. (A.14a) when the two weight families are the same. In d2Q5 [$t_c^{(a)}=t_c^{(m)}=\frac{1}{2}$], Eq. (A.14a) is satisfied with two real roots, $r=0$ and $r_1^{(k)}$ from Eq. (48a). In d2Q5$^{(r)}$ [$t_c^{(a)}=t_c^{(m)}=0$], Eq. (A.14a) is satisfied with $r=-1$ and two roots $r_{1,2}^{(k)}$ from Eq. (48b); $r_{1,2}^{(k)}$ are real when $Pe_\perp^{(k)}<\sqrt{2}$. In turn, Eq. (A.14a) has three real roots when $t_c^{(a)}\in[0,\frac{1}{2}]$ && $(Pe_\perp^{(k)}<Pe_\perp^{min}(t_c))$, or when $t_c\in[\frac{1}{4},\frac{1}{2}]$ && $(Pe_\perp^{(k)}>Pe_\perp^{max}(t_c))$, with $Pe_\perp^{max}|_{t_c\to\frac{1}{4}}=\infty$. In that, $\{Pe_\perp^{min}(t_c),Pe_\perp^{max}(t_c)\}$ are the two positive roots to Eq. (A.14b). Otherwise, one root is real and the two others are complex-conjugate. A singular weight-value is $t_c^{(a)}=t_c^{(m)}=\frac{1}{4}$, where $Pe_\perp^{min}|_{(t_c=\frac{1}{4})}=8\sqrt{3}/9$ and $Pe_\perp^{max}|_{t_c\to\frac{1}{4}}=\infty$. The roots to Eq. (A.14a) are illustrated in Fig. 7.

Example: Consider the d2Q5[$t_c^{(a)}=t_c^{(m)}=\frac{1}{2}$] and d2Q5$^{(r)}$[$t_c^{(a)}=t_c^{(m)}=0$] when $t_q^{(M)}\neq t_q^{(m)}$ in the diagonal system. These two cases are instructive because the last term in Eq. (2a) becomes piece-wise constant and non-zero for all links; it excites the A-layer in these two models. The d2Q5 constructs the A-layer with $\hat{A}_x^{+(k)}=\hat{A}_y^{+(k)}$ on the four roots $r|_{\mathrm{d2Q5}}^{(u=0)}$ from Eq. (A.8b), following the general procedure from Sec. 4.2.3. The d2Q5$^{(r)}$ builds the accommodation with the two B-layer roots $r|_{\mathrm{d2Q5}^{(r)}}^{(u=0)}$ from Eq. (A.9) using Eqs. (A.12c)-(A.12e) for $\hat{a}_{q,j}^{(k)}(a_j^{(k)})$. The A-layer is then inter-connected through the coordinate links, but the set $\{p_0^{(k)},a_1^{(k)}\}$ remains decoupled on the two sub-diagonals with d2Q5$^{(r)}$. When $\Lambda=\frac{1}{4}$, the diffusion roots vanish and the B-layer accommodates the case $t_q^{(M)}\neq t_q^{(m)}$.

Appendix A.3. The A-layer in interface-parallel velocity

We address Eq. (51) with $u_{x'}=u_\parallel(y')\vec{1}_{x'}$; Eq. (26) then reads :

$$\hat{a}_{q,j}r_j^n\ =\ a_jt_q^{(a)}\bar{\Delta}_qu_{x'}(n)c_{qx'}r_j^n-a_j\Lambda^-c_et_q^{(m)}\bar{\Delta}_q^2r_j^n+(\Lambda-\frac{1}{4})\hat{a}_{q,j}(n)\bar{\Delta}_q^2r_j^n\ . \tag{A.15}$$

The solution can be presented in the form:

$$\begin{aligned}\hat{a}_{x,j}(n)&=\hat{a}_j^{(u=0)}(a_j,t_c^{(m)})-\hat{a}_j^{(u)}(n)\ ,\ \vec{c}_q=\vec{c}_x\ ,\\ \hat{a}_{y,j}(n)&=\hat{a}_j^{(u=0)}(a_j,t_c^{(m)})+\hat{a}_j^{(u)}(n)\ ,\ \vec{c}_q=\vec{c}_y\ ,\\ \hat{a}_{\perp,j}&=-(\hat{a}_{x,j}+\hat{a}_{y,j})=-2\hat{a}_j^{(u=0)}(a_j,t_c^{(m)})\ .\end{aligned} \tag{A.16}$$

When $\vec{u}=0$, Eq. (A.16) reduces to $\hat{a}_j^{(u=0)}(a_j,t_c^{(m)})$ in Eq. (A.4). The two coordinate links, $\vec{c}_q=\vec{c}_y$ and $\vec{c}_q=\vec{c}_x$, get the coefficients $\pm\hat{a}_j^{(u)}(n)$ in Eq. (A.16), and they become polynomial together with $u_{x'}(n)$. The $\hat{a}_{\perp,j}$ remains velocity-independent in Eq. (A.16); the roots $\{r_j\}$ then solve Eqs. (42) and (43) derived in pure diffusion.

Appendix B. The B-layer accommodation

The B-layer from Eq. (18) applies along the directional segment $\{\vec{r}_n=\vec{r}_0+n\vec{c}_q,\ n=0,\dots,N\}$ connecting the interface nodes $\vec{r}_0$ and $\vec{r}_N$ inside phase k. Eq. (18) is prescribed in this work with $K_{(+1)}=\{K_k\}$:

$$\Lambda_k\ \neq\frac{1}{4}\ :\ K_k=\tfrac{2\sqrt{\Lambda_k}-1}{2\sqrt{\Lambda_k}+1}\ ,\ K_k|_{\Lambda_k\to0}=-1\ ,\ K_k|_{\Lambda_k\to\infty}=1\ ,\ k=1,2\ . \tag{B.1}$$

The B-layer obeys the local mass-conservation with Eq. (28b), and it vanishes on the translation-invariant direction $\vec{1}_{x'}$.

Appendix B.1. The straight layers

Consider $\theta = 0$ and construct the B-layer along $\vec{c}_q = \{\vec{c}_y, \vec{c}_\parallel, \vec{c}_\perp\}$:

$$\theta = 0 \ : \ \hat{B}_q^{+(k)}(n) = b_q^{+(k)} K_k^{n_k} + d_q^{+(k)} K_k^{-n_k} \ , \ \hat{B}_q^{-(k)}(n) = \frac{\Lambda_k}{\Lambda_k^-}(b_q^{+(k)} K_k^{n_k} - d_q^{+(k)} K_k^{-n_k}) \ , \tag{B.2a}$$

$$\hat{B}_x^{\pm(k)} = 0 \ , \ \hat{B}_y^{\pm(k)} + \hat{B}_\parallel^{\pm(k)} + \hat{B}_\perp^{\pm(k)} = 0 \ , \ n_k \in [0, H_k - 1] \ . \tag{B.2b}$$

Making use of Eq. (B.2b), the B-layer is fixed with the four coefficients per phase k, say $\{b_\parallel^{(+,k)}, d_\parallel^{(+,k)}, b_\perp^{+(k)}, d_\perp^{+(k)}\}$. The B-layer vanishes in d2Q5 due to Eq. (B.2b), and it is fixed with two coefficients in d2Q5$^{(r)}$:

$$\theta = 0 \ , \ \text{d2Q5} \ : \ \hat{B}_q^{\pm(k)} = 0 \ , \ \forall \ q \ ; \tag{B.3a}$$

$$\theta = 0 \ , \ \text{d2Q5}^{(r)} \ : \ \hat{B}_\parallel^{\pm(k)} = -\hat{B}_\perp^{\pm(k)} \ , \ b_\parallel^{(+,k)} = -b_\perp^{+(k)} \ , \ d_\parallel^{(+,k)} = -d_\perp^{+(k)} \ . \tag{B.3b}$$

When $\Lambda = \frac{1}{4}$, the B-layer is defined with the four (interface-node) values, e.g., $\{\hat{B}_\parallel^{+(k)}, \hat{B}_\perp^{+(k)}\}|_{n_k=\{0,H_k-1\}}$; the set $\{\hat{B}_q^{-(k)}\}$ is expressed through these coefficients with Eq. (B.2a).

Appendix B.2. The diagonal layers

Consider $\theta = \frac{\pi}{4}$ and prescribe the B-layer along $\vec{c}_y$ and $-\vec{c}_x$ in sign convention of Eq. (18):

$$\theta = \frac{\pi}{4} \ : \ \hat{B}_y^{+(k)}(n) = b_y^{+(k)} K_k^{n_k} + d_y^{+(k)} K_k^{-n_k} \ , \ \hat{B}_y^{-(k)}(n) = \frac{\Lambda_k}{\Lambda_k^-}(b_y^{+(k)} K_k^{n_k} - d_y^{+(k)} K_k^{-n_k}) \ ; \tag{B.4a}$$

$$\hat{B}_x^{+(k)}(n) = b_x^{+(k)} K_k^{n_k} + d_x^{+(k)} K_k^{-n_k} \ , \ \hat{B}_x^{-(k)}(n) = -\frac{\Lambda_k}{\Lambda_k^-}(b_x^{+(k)} K_k^{n_k} - d_x^{+(k)} K_k^{-n_k}) \ , \tag{B.4b}$$

$$\hat{B}_\parallel^{\pm(k)}(n) = 0 \ , \ \hat{B}_\perp^{+(k)}(n) = -(\hat{B}_x^{+(k)} + \hat{B}_y^{+(k)}) \ , \ \text{ then } \ \hat{B}_\perp^{-(k)}(n) = \hat{B}_x^{-(k)} - \hat{B}_y^{-(k)} \ . \tag{B.4c}$$

The B-layer is fixed through $\{b_x^{+(k)}, b_y^{+(k)}, d_x^{+(k)}, d_y^{+(k)}\}$; this set reduces to two coefficients in d2Q5 and it vanishes in d2Q5$^{(r)}$:

$$\theta = \frac{\pi}{4} \ , \ \text{d2Q5} \quad : \hat{B}_x^{\pm(k)} = \mp \hat{B}_y^{\pm(k)} \ , \ b_x^{+(k)} = -b_y^{+(k)} \ , \ d_x^{+(k)} = -d_y^{+(k)} \ ; \tag{B.5a}$$

$$\theta = \frac{\pi}{4} \ , \ \text{d2Q5}^{(r)} : \hat{B}_q^{\pm(k)} = 0 \ , \ \forall \ q \ . \tag{B.5b}$$

When $\Lambda = \frac{1}{4}$, the B-layer is set with the four (interface-node) values $\{\hat{B}_x^{+(k)}, \hat{B}_y^{+(k)}\}|_{n^{(k)}=\{0,H_k-1\}}$; the set $\{\hat{B}_x^{-(k)}, \hat{B}_y^{-(k)}\}|_{n^{(k)}=\{0,H_k-1\}}$ is related to them through Eq. (18c):

$$\theta = \frac{\pi}{4} \ , \ \Lambda_k = \frac{1}{4} \ : \ \{\hat{B}_y^{-(k)}\} = \{-\frac{\hat{B}_y^{+(k)}}{2\Lambda^-}|_{n=-1}^{k=1}, \frac{\hat{B}_y^{+(k)}}{2\Lambda^-}|_{n=0}^{k=2}, \frac{\hat{B}_y^{+(k)}}{2\Lambda^-}|_{n=-H_1}^{k=1}, -\frac{\hat{B}_y^{+(k)}}{2\Lambda^-}|_{n=H_2-1}^{k=2}\} \ ; \tag{B.6a}$$

$$\{\hat{B}_x^{-(k)}\} = \{\frac{\hat{B}_x^{+(k)}}{2\Lambda^-}|_{n=-1}^{k=1}, -\frac{\hat{B}_x^{+(k)}}{2\Lambda^-}|_{n=0}^{k=2}, -\frac{\hat{B}_x^{+(k)}}{2\Lambda^-}|_{n=-H_1}^{k=1}, \frac{\hat{B}_x^{+(k)}}{2\Lambda^-}|_{n=H_2-1}^{k=2}\} \ ; \tag{B.6b}$$

$$\{\hat{B}_\perp^{+(k)}\} = \{-(\hat{B}_x^{+(k)} + \hat{B}_y^{+(k)})\} \ , \ \text{ then } \ \{\hat{B}_\perp^{-(k)}\} = \{\hat{B}_x^{-(k)} - \hat{B}_y^{-(k)}\} \ . \tag{B.6c}$$

The B-layer coefficients are fixed by interface (boundary) conditions together with the polynomial and A-layer remaining unknowns; the B-layer vanishes when there is only one interface-cut link.

References

[1] R. Aris, On the dispersion of a solute in a fluid flowing through a tube, Proc. R. Soc. Lond. 235 (1956) 67-77.

[2] S. Bogner, R. Ammer, U. Rüde. Boundary conditions for free interfaces with the lattice Boltzmann method. J. Comput. Phys. 297 (2015) 1-12.

[3] M. Bouzidi, D. d'Humières, P. Lallemand, L-S. Luo, Lattice Boltzmann equation on a two-dimensional rectangular grid, J. Comput. Phys. 172 (2001) 704-717.
[4] H. Brenner, Dispersion resulting from flow through spatially periodic porous media, Philos. Trans. R. Soc. Lond, Ser. A 297(1430) (1980) 81–133.
[5] C. Cercignani, Theory and Application of the Boltzmann Equation, Scottish Academic, New-York, 1975.
[6] Z. Chai, T. S. Zhao. Lattice Boltzmann model for convection-diffusion equation. Phys. Rev. E 87, 063309-15, 2013.
[7] S. Chapman, On the law of distribution of velocities, and on the theory of viscosity and thermal conduction, in a non-uniform simple monoatomic gas, Phil. Trans. Roy. Soc. A 216 (1916) 279-349.
[8] Y. I. Chen, K. Q. Zhu, A study of the upper limit of solid scatters density for gray Lattice Boltzmann method, Acta Mech Sin 24 (2008) 515-537.
[9] S. Cui, N. Hong, B. Shi, Z. Chai, Discrete effect on the halfway bounce-back boundary condition of multiple-relaxation-time lattice Boltzmann model for convection-diffusion equations, Phys. Rev. E 93 (2016) 043311-13.
[10] D. Contarino, P. Lallemand, P. Asinary, L.-S. Luo, Lattice Boltzmann simulations of the thermally driven 2D square cavity at high Rayleigh numbers, J. Comput. Phys. 275 (2014) 257-272.
[11] R. Cornubert, D. d'Humières, D. Levermore, A Knudsen layer theory, Physica D 47 (1991) 241-259.
[12] R. Cornubert, Boundary conditions in discrete kinetic models: Knudsen layers and obstacles. PhD Thesis, Paris 6, 1991.
[13] S. Dellacherie, Construction and Analysis of Lattice Boltzmann Methods Applied to a 1D Convection-Diffusion equation, Acta Applicandae Mathematicae 131(1) (2014) 69-140.
[14] P. Dellar, Incompressible limits of Lattice Boltzmann equations using multiple relaxation times J. Comp. Phys. 191 (2003) 351-370.
[15] C. Demuth, S. Mishra, M. A. Mendes, S. Ray, D. Trimis, Application and accuracy issues of TRT lattice Boltzmann method for solving elliptic PDEs commonly encountered in heat transfer and fluid flow problems, Int. J. of Thermal Sciences. 100 (2016) 185-201.
[16] G. Drazer, J. Koplik, Tracer dispersion in two dimensional rough fractures, Phys. Rev. E 63 (2001) 056104-1-11.
[17] F. Dubois, P. Lallemand, Towards higher order lattice Boltzmann schemes, J. of Stat. Mech.: Theory and Experiment. P06 (2009) P06006-47.
[18] F. Dubois, P. Lallemand, M. M. Tekitek, Taylor expansion method for analyzing bounce-back boundary conditions for lattice Boltzmann method, ESAIM: Proceedings and surveys 52 (2015) 25-46.
[19] D. Enskog, The kinetic theory of Phenomena in fairly rare gases, Dissertation, Upsala, 1917.
[20] U. Frisch, D. d'Humières, B. Hasslacher, P. Lallemand, Y. Pomeau, J.-P. Rivet, Lattice Gas Hydrodynamics in Two and Three Dimensions, Complex Systems 1 (1987) 649-707.
[21] T. Gebäck and A. Heintz. A Lattice Boltzmann Method for the Advection-Diffusion Equation With Neumann Boundary Conditions. Com. Comp. Phys. 15(2) (2013) 487–505.
[22] I. Ginzbourg, P. M. Adler, Boundary flow condition analysis for the three-dimensional lattice Bolzmann model, J. Phys. II France 4 (1994) 191–214.
[23] I. Ginzbourg, D. d'Humières, Local Second-Order Boundary method for Lattice Boltzmann models, J. Stat. Phys. 84(5/6) (1996) 927–971.
[24] I. Ginzburg, Generic boundary conditions for Lattice Boltzmann models and their application to advection and anisotropic-dispersion equations, Adv. Wat. Res. 28 (2005) 1196–1216.
[25] I. Ginzburg, D. d'Humières, Lattice Boltzmann and analytical modeling of flow processes in anisotropic and heterogeneous stratified aquifers, Adv. Water Resour. 30 (2007) 2202-2234.
[26] I. Ginzburg, Lattice Boltzmann modeling with discontinuous collision components, Hydrodynamic and advection-diffusion equations, J. Stat. Phys. 126 (2007) 157–203.
[27] I. Ginzburg, F. Verhaeghe, d'Humières, Study of simple hydrodynamic solutions with the two-relaxation-times Lattice Boltzmann scheme, Commun. Comput. Physics 3(3) (2008) 519–581.
[28] I. Ginzburg, Consistent Lattice Boltzmann schemes for the Brikman model of porous flow and infinite Chapman-Enskog expansion, Phys. Review E 77 (2008) 066704-1-12.
[29] I. Ginzburg, Truncation errors, exact and heuristic stability analysis of two-relaxation-times lattice Boltzmann schemes for anisotropic advection-diffusion equation, Commun. Comput. Phys. 11(5) (2012) 1439–1502.
[30] I. Ginzburg, L. Roux, Truncation effect on Taylor-Aris dispersion in Lattice Boltzmann schemes: accuracy towards stability, J. Comput. Phys. 299 (2015) 974–1003.
[31] I. Ginzburg, G. Silva, L. Talon, Analysis and improvement of Brinkman Lattice Boltzmann schemes: bulk, boundary, interface. Similarity and distinctness with finite-elements in heterogeneous porous media, Phys. Rev. E. 91 (2015) 023307-32.
[32] I. Ginzburg, Prediction of the moments in advection-diffusion lattice Boltzman method. II. Attenuation of the boundary layers via double-Λ bounce-back flux scheme, Phys. Rev. E 95 (2017) 013305-42.
[33] I. Ginzburg, A. Vikhansky, Determination of the diffusivity, dispersion, skewness and kurtosis in heterogeneous porous flow. Part I: Analytical solutions with the Extended Method of Moments, Adw. Wat. Res. 115 (2018) 60-87.
[34] I. Ginzburg, Determination of the diffusivity, dispersion, skewness and kurtosis in heterogeneous porous flow. Part II: Lattice Boltzmann schemes with implicit interface, Adw. Wat. Res. 118 (2018) 49-82.
[35] I. Ginzburg. Steady-state Two-relaxation-time Lattice Boltzmann formulation for transport and flow, closed with the compact multi-reflection boundary and interface-conjugate schemes. J. of Comp. Science. (2020) https://doi.org/10.1016/j.jocs.2020.101215
[36] Y. Guan, I. Novosselov. Two relaxation time lattice Boltzmann method coupled to fast Fourier transform Poisson solver: Application to electroconvective flow. J. of Comp. Phys., 397 (2019), https://doi.org/10.1016/j.jcp.2019.07.029
[37] K. Guo, L. Li, G. Xiao, N. AuYeung, R. Mei, Lattice Boltzmann method for conjugate heat and mass transfer with

interfacial jump conditions, Int. J. of Heat and Mass Transfer 88 (2015) 306-322.
[38] X. He, Y. Zou, L.-S. Luo, M. Dembo, Analytic Solutions of Simple Flows and Analysis of Nonslip Boundary Conditions for the Lattice Boltzmann BGK Model, J. Stat. Phys. 87 (1997) 115–135.
[39] F. J. Higuera, J. Jiménez, Boltzmann approach to lattice gas simulations, Europhys. Lett. 9 (1989) 663-668.
[40] F. J. Higuera, S. Succi, R. Benzi, Lattice Gas Dynamics with Enhanced Collisions, Europhys. Lett. 9 (1989) 345-349.
[41] D. d'Humières, Generalized Lattice-Boltzmann Equations, Prog. Astronaut. Aeronaut. 59 (1992) 450-548.
[42] D. d'Humières, I. Ginzburg, Viscosity independent numerical errors for Lattice Boltzmann models: from recurrence equations to "magic" collision numbers, Comp. Math. Appl. 58(5) (2009) 823–840.
[43] M. Junk, Z. Yang, Convergence of lattice Boltzmann methods for Stokes flows in periodic and bounded domains, Comp. Math. Appl. 55 (2008) 1481–1491.
[44] G. A. Korn, T. M. Korn, Mathematical handbook for scientists and engineers: Definitions, Theorems, and Formulas for Reference and Review. Nauka, Moscow (in Russian), 1968.
[45] S. Khirevich, I. Ginzburg, U. Tallarek, Coarse- and fine-grid numerical behavior of MRT/TRT Lattice-Boltzmann schemes in regular and random sphere packings, J. Comp. Phys. 281 (2014) 708–742.
[46] T. Krüger, H. Kusumaatmaja, A. Kuzmin, 0. Shardt, G. Silva, E.M. Viggen, The Lattice Boltzmann Method Principles and Practice. 1st ed. Springer, 2016.
[47] P. Lallemand, L.-S. Luo, Theory of the lattice Boltzmann method: Dispersion, dissipation, isotropy, Galilean invariance, and stability, Phys. Rev. E 61 (2000) 6546–6562.
[48] L. Li, R. Mei, J. F. Klausner, Boundary conditions for thermal lattice Boltzmann equation method, J. Comp. Phys. 237 (2013) 366-395.
[49] L. Li, R. Mei, J. F. Klausner, Conjugate heat and mass transfer in the lattice Boltzmann equation method, Phys. Rev. E 89 (2014) 043308-21.
[50] L. Li, N. AuYeung, R. Mei, J. F.Klausner, Effects of tangential-type boundary condition discontinuities on the accuracy of the lattice Boltzmann method for heat and mass transfer, Phys. Rev. E. 94 (2016) 023307-30.
[51] L. Li, J. Klausner, Lattice Boltzmann models for the convection-diffusion equation: D2Q5 vs D2Q9, Int. J. of Heat and Mass Transfer 108 (2017) 41-62.
[52] G. R. McNamara, G. Zanetti, Use of the Boltzmann equation to simulate lattice-gas automata Phys. Review Letters 61(20) (1988) 2332-2335.
[53] S. Mohammed, D. Graham, T. Reis, Assessing moment-based boundary conditions for the lattice Boltzmann equation: A study of dipole-wall collisions. Computers and Fluids 176 (2018) 79-96.
[54] X. Nie, N. S. Martys, Breakdown of Chapman-Enskog expansion and the anisotropic effect for lattice-Boltzmann models of porous media, Phys. Fluids 19 (2007) 011702-1–4.
[55] Y. Qian, D. d'Humières, P. Lallemand, Lattice BGK models for Navier-Stokes equation, Europhys. Lett. 17 (1992) 479–484.
[56] J. Salles, J.-F. Thovert, R. Delannay, L. Prevors, J.-L. Auriault, P. M. Adler, Taylor dispersion in porous media. Determination of the dispersion tensor, Phys. Fluids A 5(10) (1993) 2348-2377.
[57] A. Sengupta, P. S. Hammond, D. Frenkel, E. S. Boek, Error analysis and correction for Lattice Boltzmann simulated flow conductance in capillaries of different shapes and alignments, J. Comp. Phys. 231 (2012) 2634–2640.
[58] B. Servan-Camas, Frank T.-C. Tsai. Lattice Boltzmann method with two relaxation times for advectiondiffusion equation: Third order analysis and stability analysis. Adv. in Water Res. 31 (8), (2008) 1113-1126.
[59] B. Servan-Camas, Frank T.-C. Tsai. Non-negativity and stability analyses of lattice Boltzmann method for advectiondiffusion equation. J. of Comp. Phys. 228 (1), (2009), 236-256.
[60] G. Silva, V. Semiao, Truncation errors and the rotational invariance of three-dimensional lattice models in the lattice Boltzmann method, J. Comp. Phys. 269 (2014) 259-279.
[61] G. Silva, L. Talon, I. Ginzburg, Low- and high-order accurate boundary conditions: From Stokes to Darcy porous flow modeled with standard and improved Brinkman lattice Boltzmann schemes, J. Comp. Phys. 335 (2017) 50-83.
[62] G. Silva, Consistent lattice Boltzmann modeling of low-speed isothermal flows at finite Knudsen numbers in slip-flow regime: II. Application to curved boundaries. Phys. Rev. E 98 (2018) 023302.
[63] G. Silva, I. Ginzburg, Reviving the Local Second-Order Boundary Approach within the Two-Relaxation-Time Lattice Boltzmann Modelling, Phil. Trans. R. Soc. A. (2020) 378:20190404.
[64] H. Struchtrup, Linear kinetic heat transfer: Moment equations, boundary conditions, and Knudsen layers, Physica A 387 (2008) 1750-1766.
[65] G. I. Taylor, Dispersion of soluble matter in solvent flowing slowly through a tube, Proc. R. Soc. Lond, Ser. A. 219 (1953) 186–2003.
[66] D. Valougeorgis, S. Naris, Analytical Lattice Boltzmann Solutions for Thermal Flow Problems, Thransport Theory and Statistical Physics 32 5-7 (2003) 639-650.
[67] F. J. Valds-Parada, D. Lasseux, F. Bellet, A new formulation of the dispersion in homogeneous porous media, Adv. Water Res. 90 (2016) 70-82.
[68] A. Vikhansky, I. Ginzburg, Taylor dispersion in heterogeneous porous media: Extended method of moments, theory, and modelling with two-relaxation-times Lattice Boltzmann scheme, Physics of Fluids 26 (2014) 022104-52.
[69] wikipedia.org/wiki/Quartic_function
[70] S. D. C. Walsh, H. Burwinkle, and M. O. Saar, A new partial bounce-back lattice Boltzmann mathod for fluid flow through heterogeneous media, Comput. Geosci. 36 (2009) 1186-1193.
[71] Z. Yan, X. Yang, S. Li, M. Hilpert. Two-relaxation-time lattice Boltzmann method and its application to advective-diffusive-reactive transport. Adv. Wat. Res., 109, p. 333-342, 2017.

[72] J. Zhu, J. Ma, An improved gray lattice Boltzmann model for simulating fluid flow in multi-scale porous media, Adv. Water Res. 56 (2013) 61–76.
[73] Q. Zou, S. Hou, G. D. Doolen, Analytical solutions of the lattice Boltzmann BGK model, J. Stat. Phys. 81 (1995) 319–339.